High-resolution O$_2$ Imaging of Living Tissues Based on Phosphorescence Lifetime Imaging Microscopy Using Ir(III) Complexes

KIICHI MIZUKAMI

Gunma University

2020

Contents

Chapter 1

General Introduction

1-1 Importance of Molecular Oxygen in Aerobic Organisms

Molecular oxygen (O_2) is one of the most essential requirements of aerobic organisms on earth. Oxygen has various functions in the living body. One is a source of reactive O_2 species (ROS), and both O_2 and ROS may affect transcription of many genes. The other most important function of O_2 is as the terminal electron acceptor for electrons in the electron transport chain in mitochondria. The mitochondria consume over 90 % of O_2 in cells to produce adenosine triphosphate (ATP) during oxidative phosphorylation. As the oxygen deprivation leads to impaired cell function and even death, it is constantly delivered to each cell through the blood circulation including microcirculation in the body (Fig. 1-1). First, oxygen that entered the alveoli by breathing passes through the walls of the blood vessels and dissolves in arterial blood. Then, it circulates throughout the body and supplies oxygen to each cell by diffusion. Due to its low solubility in water, oxygen is carried with the bloodstream by binding to hemoglobin in erythrocytes. In humans, the partial pressure of oxygen (pO_2) in alveoli is about 100 mmHg, and those in arteries and veins are reduced to about 80-100 mmHg and 40 mmHg, respectively (Fig. 1-1) due to O_2 consumption in cells. Therefore, an O_2 concentration gradient is generated from the alveoli to mitochondrion in the living body.

Maintaining O_2 homeostasis is critical for cellular function, proliferation, and survival. Disruption of oxygen homeostasis is, therefore, associated with various diseases such as cerebral infarction, fatty liver disease, chronic kidney disease, diabetic retinopathy, and cancer [1-3]. Recent studies have shown that cells have a defense mechanism against the hypoxia (lack of O_2) through a transcription factor called hypoxia inducible factor (HIF) [4,5]. The details of the hypoxia-responsive mechanism have been revealed by extensive studies by many researchers, including 2019 Nobel

Laureates in Physiology or Medicine, Gregg Semenza, Peter Ratcliffe, and Willian Kaelin Jr.

As described above, with the recent development of oxygen biology and the pathophysiology of various hypoxia-related diseases, imaging of O_2 distribution in biological cells and tissues is becoming increasingly important. In particular, excellent techniques capable of measuring O_2 distribution of tissues *in vivo* with high-resolution are desired in medicine as well as biochemistry.
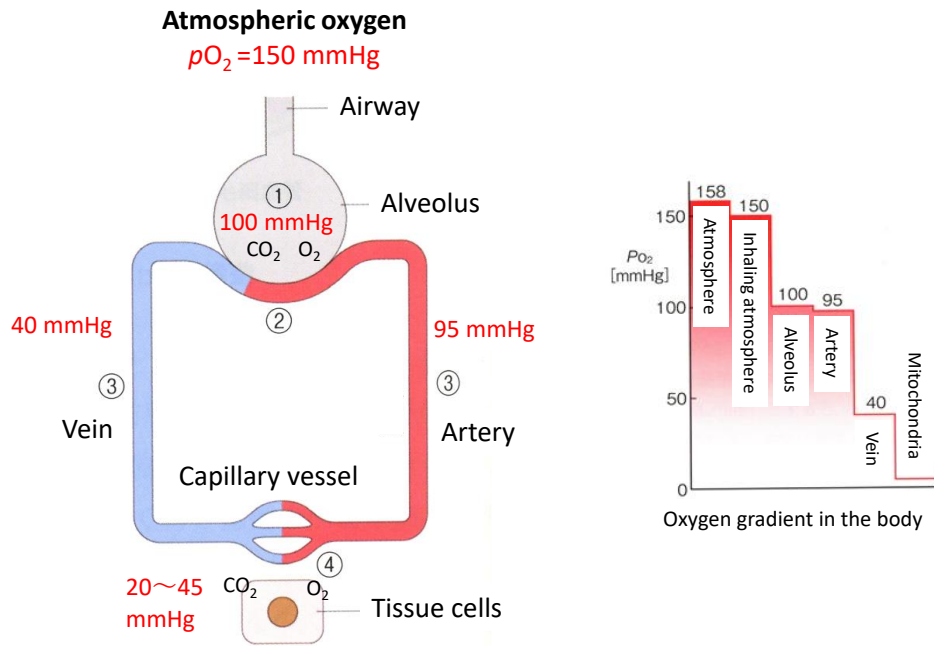
Fig. 1-1 Respiratory circulatory system of the human body and oxygen gradient from inhaling atmosphere to mitochondria. Revised the figure in "Human Anatomy Physiology" by Muneyuki Horikawa (Shinko Trading Company, 2014).

1-2   Optical Detection of Oxygen Levels in Cells and Tissues

Over the last few decades, various techniques have been developed for measuring oxygen levels *in vivo*, and their usefulness has been evaluated by various basic studies using small animals as well as cell cultures. The most typical techniques include oxygen microelectrodes [6,7], hypoxia markers such as nitroimidazole derivatives [8-10], blood oxygen level-dependent magnetic resonance imaging (Bold MRI) [11,12], positron emission tomography (PET) using a hypoxia tracer [13], electron paramagnetic resonance (EPR) oximetry [14,15], and optical imaging [16-18]. These methods have advantages and limitations in terms of applicable targets, spatial resolution, observation depth, reversibility, invasiveness, convenience, etc. Among these techniques, the optical O_2 imaging method uses a luminescent microscope to image the O_2 distribution by administrating phosphorescent molecules into tissues as an O_2 probe. This method has the advantages of being less invasive and capable of high-resolution, real-time imaging of oxygen in the living tissue, but it also has the disadvantage of being less permeable to tissue: ~ 1 cm depth even under near-infrared excitation [19].

Optical oxygen measurement methods usually use transition-metal complexes such as Pt(II) and Pd(II) porphyrins, Ru(II) complexes, Ir(III) complexes, and Pt(II) complexes as O_2 probes [16-18,20,21]. Due to the heavy atom effect of the central metal ion, these complexes provide intense phosphorescence in the visible to near-infrared wavelength range with reasonably long lifetimes (> 1.0 μs) under deaerated conditions. By using these metal complexes as oxygen-sensitive cores and making appropriate modifications, oxygen probes suitable for various biological targets have been developed so far. These include cell-penetrating conjugates of Pt(II)-porphyrins [22,23], dendrimerized Pt(II)- and Pd(II)-porphyrins [24-26], Ru(II) complex

5

derivatives that target the cell nucleus [27], ratiometric O_2 probes linking an Ir(III) complex and fluorophore [28,29], etc. The molecular structures of some of these complexes and displayed in Fig. 1-2.

Wide-field emission lifetime measurements using a phosphorescent probe and a gated CCD camera have enabled wide-field O_2 imaging of tumor tissues, fundus tissues, and specific organs, etc [30-33]. On the other hand, phosphorescence lifetime imaging microscopy (PLIM) measurements [34,35] using a phosphorescent O_2 probe have allowed O_2 imaging at cellular level resolution, and provided detailed information on its microenvironment including real-time changes of O_2 distribution. The PLIM method using cell-penetrating small-molecule or nanoparticle probes has been successfully applied to image the oxygen status of giant cells [36], cell spheroids [22,26,37-38], neurospheres [39,40] and the epithelium of rat and human colon tissues [41]. Vinogradov and coworkers have succeeded in microvascular and interstitial O_2 imaging of the brain [24,41,42], bone marrow [43,44], and retinal tissue [45] in vivo by applying the PLIM method using dendrimerized Pt-porphyrin probes to small animals.
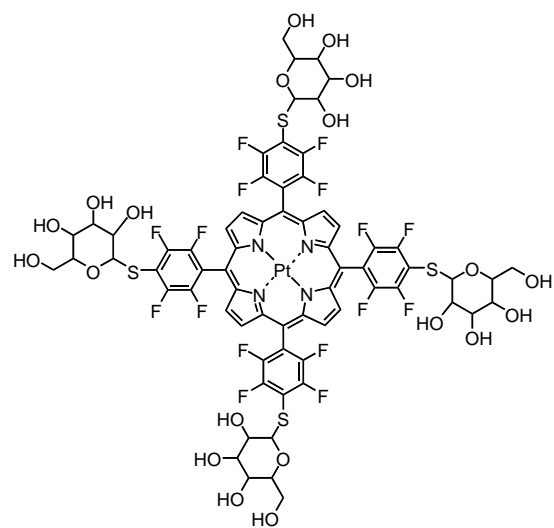
Pt-Glc
(cell-penetrating conjugate of Pt(II)-porphyrin)
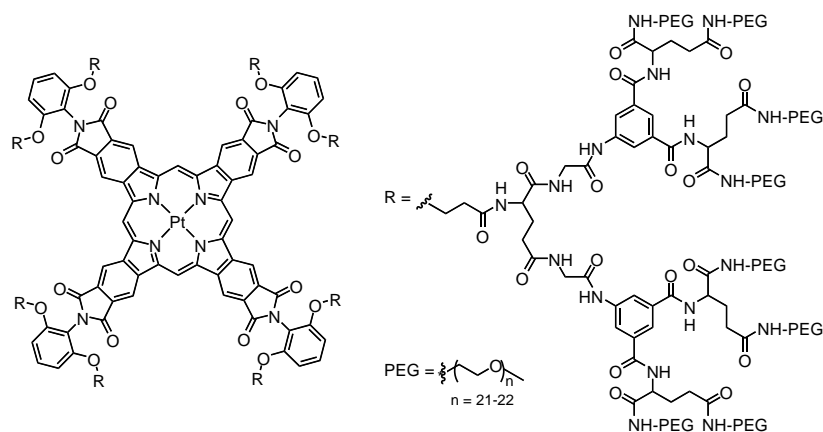
Oxyphor 2P
(dendritic Pt(II)-porphyrin)
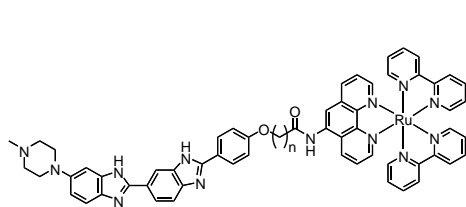
Ru-Hoechst
(Hoechst-tagged Ru(II) complex)
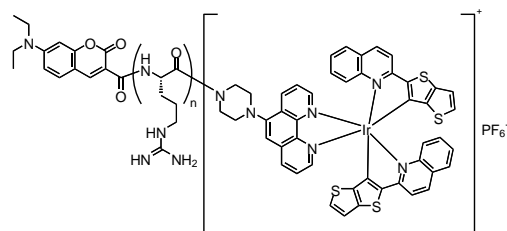
7DEAC-R_n-BTQPhen
(ratiometric O_2 probe)

Fig. 1-2 Molecular structures of representative phosphorescent O_2 probes.

1-3 O₂ Imaging Based on Phosphorescence Lifetime Imaging Microscopy

The PLIM method is a sophisticated optical imaging method recently developed as an extension of fluorescence lifetime imaging microscopy (FLIM) [34,35]. An inverted microscope or upright microscope combined with a confocal scanning system with a high-frequency pulsed laser is used in these methods (Fig. 1-3A). The sample is excited by a high-repetition laser pulse (typically, pulse width: 40-90 ps, repetition: 50 MHz) under a microscope, and the emission from each pixel (usually 128×128 or 256×256 pixels) is detected by a photomultiplier tube via a confocal scanning system. Repeated fluorescence decay measurements using the confocal scanning system enable acquisition of fluorescence decay profile of each pixel based on the time-correlated single photon counting (TCSPC) method. A FLIM image can be obtained by displaying the lifetime in each pixel on a color scale (Fig. 1-3B).

Similar measurements are not applicable to the acquisition of phosphorescence image because the phosphorescence decay time is much longer than that of fluorescence. This is because almost no decay occurs in phosphorescence intensity between high-repetition laser pulses. To overcome this problem, the PLIM method was developed by Becker *et al* [35]. The principle of the PLIM measurement is shown in Fig. 1-3C. At each pixel the laser is turned on only for a short period of time T_{on}. Phosphorescence builds up during the period T_{on}, and the phosphorescence decay is obtained from photons accumulated within the rest of the pixel dwell time after the laser is turned off. This method makes it possible to efficiently obtain phosphorescence lifetime images without losing the advantage of using high-repetition pulses as excitation light.

As shown in Fig. 1-4, phosphorescence is a spin-forbidden transition from the

excited triplet state of a molecule (^{3}M*), having much longer lifetimes compared with that of spin-allowed fluorescence. As a result, phosphorescence is significantly quenched by energy transfer due to collision with ground-state oxygen ($^3\Sigma$), producing ground-state molecule (^{1}M) and singlet oxygen ($^1\Delta$) (energy transfer (ET) channel). In Ir(III) complexes with low redox potentials, charge transfer from ^{3}M* to O$_2$($^3\Sigma$) competes with the ET channel to form a charge transfer complex (M$^{\delta+}$ O$_2$ $^{\delta-}$) (charge transfer (CT) channel) [46]. Due to these competing quenching processes, Ir(III) complexes have higher sensitivity to oxygen compared with other phosphorescent metal complexes such as Ru(II) complexes and Pt(II) complexes. The phosphorescence quenching property of Ir(III) complexes by O$_2$ can be applied to O$_2$ sensing in cells and tissues. Quantitative O$_2$ measurements can be performed according to the Stern-Volmer equation:

$$\frac{\tau_p^{\,0}}{\tau_p} = 1 + k_q \tau_p^{\,0} p\,O_2 = 1 + k_q{}'\tau_p^{\,0}[O_2] \tag{1-1}$$

where τ_p and τ_p^0 are the phosphorescence lifetimes under the presence and absence of O$_2$. pO$_2$ and [O$_2$] are the oxygen partial pressure in mmHg and the oxygen concentration in mol dm^{-3}, and k_q and k_q' denote the bimolecular quenching rate constant expressed by mmHg^{-1} s^{-1} and dm^3 mol^{-1} s^{-1} units. From Eq. 1-1, the following equation that gives the pO$_2$ can be obtained.

$$p\,O_2 = \frac{1}{k_q}\left(\frac{1}{\tau_p} - \frac{1}{\tau_p^{\,0}}\right) \tag{1-2}$$

If τ_p^0 and k_q are determined in advance according to Eq. 1-1, $p\mathrm{O}_2$ can be calculated from Eq. 1-2 by measuring τ_p. O_2 images of cells and tissues can be obtained by performing a similar analysis on each pixel in the lifetime image.
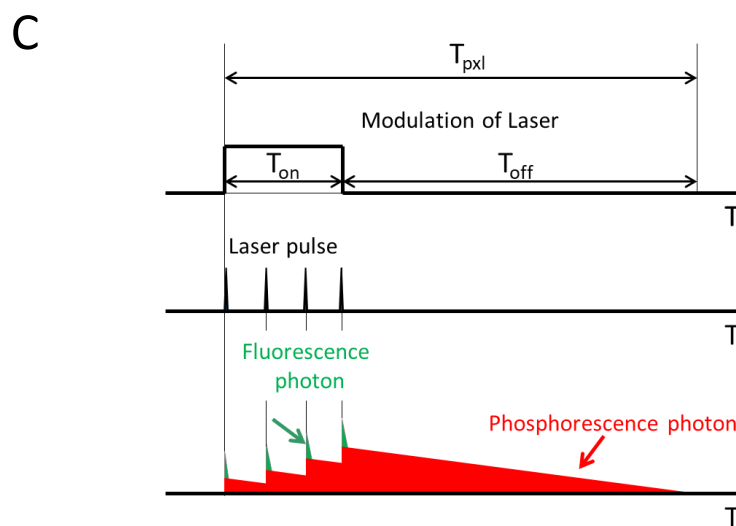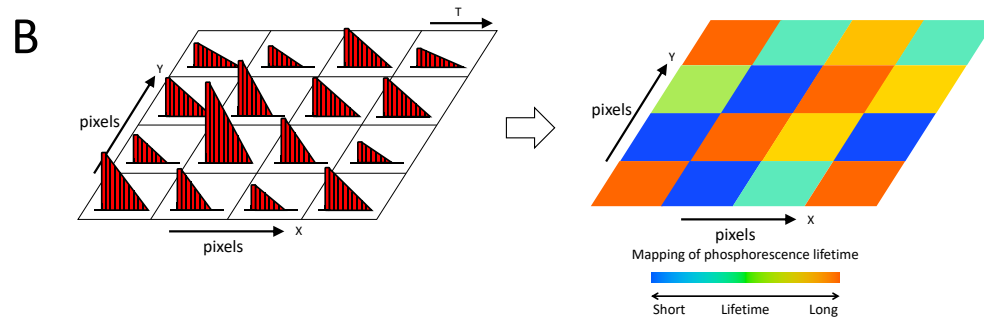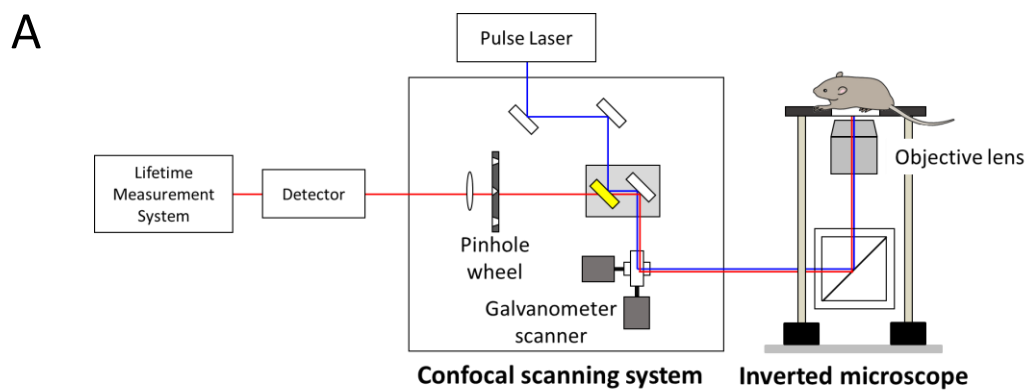
Fig. 1-3 Principle of the PLIM method. (**A**) Schematic diagram of PLIM system. (**B**) Mapping of lifetimes by color scale. (**C**) Acquisition of phosphorescence decay profile following repeated laser pulse excitation.
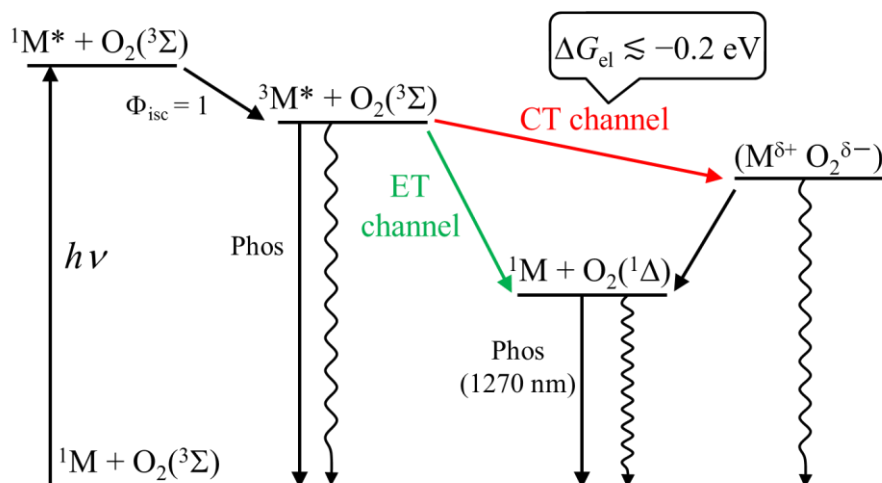
Fig. 1-4 Energy state diagram representing phosphorescence quenching by oxygen. $^1M^*$ and $^3M^*$ denote the excited singlet and triplet state of a molecule (^1M). Solid line and wavy arrows represent radiative and nonradiative processes. Phos: phosphorescence. The CT process usually occurs when the Gibbs energy change for the electron transfer reaction (ΔG_{el}) is about -0.2 eV or loss.

1-4   Purpose of This Study

In vivo O$_2$ measurements using the PLIM method reported so far are limited to intravascular measurements using hydrophilic O$_2$ probes such as dendrimerized Pt(II) or Pd(II) porphyrins (Fig. 1-2). In contrast, few studies have performed high-resolution imaging of oxygen in tissues by PLIM measurement using an intracellular O$_2$ probe, probably due to the lack of suitable probes. In our laboratory, various intracellular O$_2$ probes have been developed using Ir(III) complexes. Among them, (btp)$_2$Ir(acac-DM) (BTPDM1) (Fig. 1-5) has been shown to enable measurement of O$_2$ levels in hypoxic tumors [47,48]. To improve the reliability of optical O$_2$ imaging techniques using a small-molecule probe, it is necessary to quantify O$_2$ levels in different tissues *in vivo* and investigate various issues: localization and stability of probes in tissues, calibration of emission lifetime in tissues (cell-specific calibration), the influence of probe administration on the target tissues, etc.

In light of these challenges, this study was aimed to establish an *in vivo* O$_2$ imaging method using small-molecule intracellular O$_2$ probes by investigating the O$_2$ distribution in organ tissues of living mice by PLIM measurements. Chapter 2 describes the detailed methods of the experiments in Chapter 3-5. Chapter 3 describes the introduction of the PLIM device, evaluation of its basic performance, and O$_2$ imaging of cells and cell spheroids using the PLIM system. In Chapter 4, high-resolution O$_2$ images of hepatic tissues of mice are acquired by *in vivo* PLIM measurements using two structurally related Ir(III) complexes, BTPDM1 and BTP-3OH ((btp-OH)$_3$Ir) (Fig. 1-5), with particular interest in the O$_2$ gradient in hepatic lobules and its dynamic changes due to xenobiotics. Following these chapters, in Chapter 5, *in vivo* O$_2$ distributions of renal cortex are clarified by PLIM measurements using BTPDM1 as an intracellular probe. Based on these results, the usefulness of the

O$_2$ imaging method combining Ir(III) complexes and the PLIM measurements is summarized in Chapter 6.
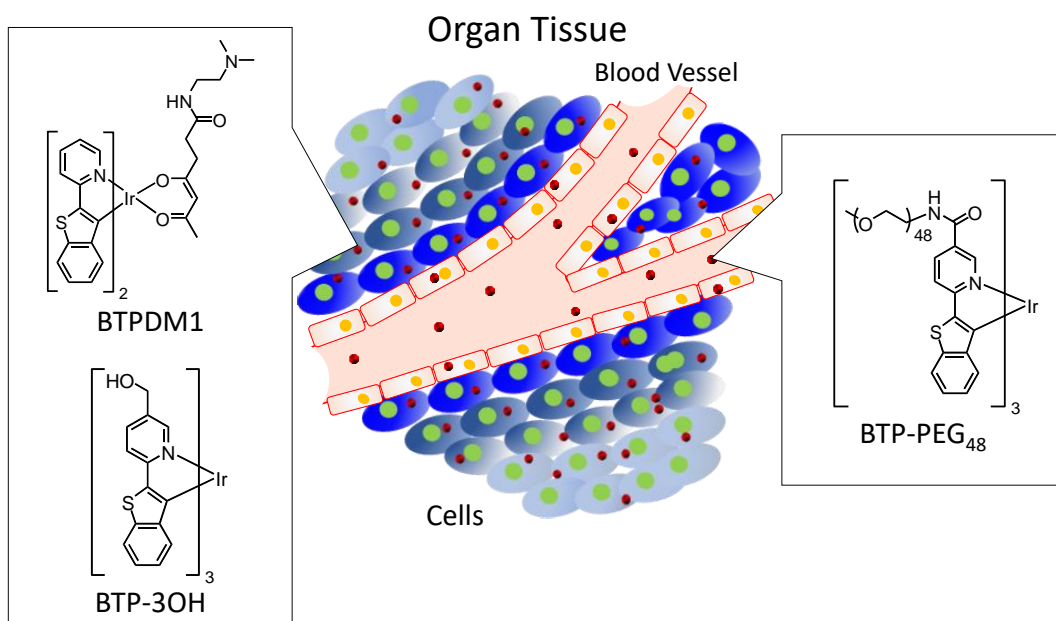
Fig. 1-5 Intracellular and intravascular probes for *in vivo* tissue O₂ measurements.

References

[1]   Mimura, I. & Nangaku, M. The suffocating kidney: tubulointerstitial hypoxia in end-stage renal disease. *Nat. Rev. Nephrol.* **6**, 667–678 (2010).

[2]   Arden, G. B. & Sivaprasad, S. Hypoxia and oxidative stress in the causation of diabetic retiopathy. *Curr. Diabetes Rev.* **7**, 291–304 (2011).

[3]   Vaupel, P. & Mayer, A. Hypoxia in cancer: Significance and impact on clinical outcome. *Cancer Metastasis Rev.* **26**, 225–239 (2007).

[4]   Semenza, G. L. Hypoxia-inducible factors in physiology and medicine. *Cell*, 148, 399-408 (2012).

[5]   Minamishima, Y. *SEIKAGAKU*, **88**, 302-307 (2016).

[6]   Rivas, L., Dulay, S., Miserere, S., Pla, L., Marin, S. B., Parra, J., Eixarch, E., Gratacós, E., Illa, M., Mir, M. & Samitier, J. Micro-needle implantable electrochemical oxygen sensor: ex-vivo and in-vivo studies. *Biosens. Bioelectron*. **153**, 112028 (2020).

[7]   Bolger, F. B., McHugh, S. B., Bennett, R., Li, J., Ishiwari, K., Francois, J., Conway, M. W., Gilmuor, G., Bannerman, D. M., Fillenz, M., Tricklebank, M . & Lowry, J. P. Characterisation of carbon past electrodes for real-time amperometric monitoring of brain tissue oxygen. *J. Neurosci. Methods* **195**, 135–142 (2011).

[8]   Okuda, K., Okabe, Y., Kadonosono, T., Ueno, T., Youssif, B. G. M., Kizaka-Kondoh, S., & Nagasawa, H. 2-Nitroimidazole-tricarbocyanine conjugate as a near-infrared fluorescent probe for in vivo imaging of tumor hypoxia, *Bioconjugate Chem*. **23**, 324–329 (2012).

[9]   Piao, W., Tsuda, S., Tanaka, Y., Maeda, S., Liu, F., Takahashi, S., Kushida, Y., Komatsu, T., Ueno, T., Terai, T., Nakazawa, T., Uchiyama, M., Morokuma, K.,

Nagano, T., & Hanaoka, K. Development of azo-based fluorescent probes to detect different levels of hypoxia, *Angew. Chem. Int. Ed.* **52**, 13028–13032 (2013).

[10] Uddin, M. I., Evans, S. M., Craft, J. R., Capozzi, M. E., McCollum, G. W., Yang, R., Marnett, L. J., Uddin, M. J., Jayagopal, A., & Penn, J. S. In vivo imaging of retinal hypoxia in a model of oxygen-induced retinopathy. *Sci. Rep.* **6**, 31011 (2016).

[11] O'Connor, J. P. B., Robinson, S. P. & Waterton, J. C. Imaging tumour hypoxia with oxygen-enhanced MRI and BOLD MRI. *Br. J. Radiol.* **92**, 20180642 (2019).

[12] Feldman, S. C., Chu, D., Schulder, M., Barry, M., Cho, E. S., & Liu, W. C. The blood oxygen level-dependent functional MR imaging signal can be used to identify brain tumors and distinguish them from normal tissue. *AJNR Am. J. Neuroradiol.* **30**, 389–395 (2009).

[13] Löck, S., Perrin, R., Seidlitz, A., Bandurska-Luque, A., Zschaeck, S., Zöphel, K., Krause, M., Steinbach, J., Kotzerke, J., Zips, D., Troost, E. G. C., & Baumann, M. Residual tumour hypoxia in head-and-neck cancer patients undergoing primary radiochemotherapy, final results of a prospective trial on repeat FMISO-PET imaging. *Radiother. Oncol.* **124**, 533–540 (2017).

[14] Khan, M., Williams, B. B., Hou, H., Li, H. & Swartz, H. M. Repetitive tissue pO_2 measurements by electron paramagnetic resonance oximetry: current status and future potential for experimental and clinical studies. *Antioxid. Redox Signal* **9**, 1169–1182 (2007).

[15] Weaver, J., Burks, S. C., Lie, K. J., Kao, J. P. Y. & Rosen, G. M. In vivo EPR oximetry using an isotropically-substitutes nitroxide: Potential for quantitative

measurement of tissue oxygen. *J. Magn. Reson.* **271**, 68–74 (2016).

[16] Papkovsky, D. B. & Dmitriev, R. I. Imaging of oxygen and hypoxia in cell and tissue samples. *Cell. Mol. Life Sci.* **75**, 2963–2980 (2018).

[17] Roussakis, E., Li, Z., Nichols, A. J. & Evans, C. L. Oxygen-sensing methods in biomedicine from the macroscale to the microscale. *Angew. Chem. Int. Ed.* **54**, 8340–8362 (2015).

[18] Papkovsky, D. B. & Dmitriev, R. I. Biological detection by optical sensing, *Chem. Soc. Rev.* **42**, 8700–8732 (2013).

[19] Li, J.-B., Liu, H.-W., Fu, T., Wang, R., Zhang, X.-B., & Tan, W. Recent progress in small-molecule near-IR probes for bioimaging. *Trends Chem.* **1**, 224–234 (2019).

[20] Yoshihara, T., Hirakawa, Y., Hosaka, M., Nangaku, M. & Tobita, S. Oxygen imaging of living cells and tissues using luminescent molecular probes. *J. Photochem. Photobiol. C Photochem. Rev.* **30**, 71–95 (2017).

[21] Tobita, S. & Yoshihara, T. Intracellular and in vivo oxygen sensing using phosphorescent iridium(III) complexes. *Curr. Opin. Chem. Biol.* **33**, 39–45 (2016).

[22] Dmitriev, R. I., Kondrashina, A. V., Koren, K., Klimant, I., Zhdanov, A. V., Pakan, J. M. P., McDermott, K. W., & Papkovsky, D. B. Small molecule phosphorescent probes for O_2 imaging in 3D tissue models. *Biomater. Sci.* **2**, 853–866 (2014).

[23] Dmitriev, R. I., Ropiak, H. M., Ponomarev, G. V., Yashunsky, D. V. & Papkovsky, D. B. Cell-penetrating conjugates of coproporphyrins with oligoarginine peptides: rational design and application for sensing intracellular O_2. *Bioconjugate Chem.* **22**, 2507–2518 (2011).

[24] Esipova, T. V., Barrett, M. J. P., Erlebach, E., Masunov, A. E., Weber, B., & Vinogradov, S. A. Oxyphor 2P: A high-performance probe for deep-tissue longitudinal oxygen imaging. *Cell Metabolism* **29**, 736-744 (2019).

[25] Roussakis, E., Spencer, J. A., Lin, C. P. & Vinogradov, S. A. Two-photon antenna-core oxygen probe with enhanced performance. *Anal. Chem.* **86**, 5937–5945 (2014).

[26] Nichols, A. J., Roussakis, E., Klein, O. J. & Evans, C. L. Click-assembled, oxygen-sensing nanoconjugates for depth-resolved, near-infrared imaging in a 3D cancer model, *Angew. Chem. Int. Ed.* **53**, 3671–3674 (2014).

[27] Hara, D., Umehara, Y., Son, A., Asahi, W., Misu, S., Kurihara, R., Kondo, T., & Tanabe, K. Tracking the oxygen status in the cell nucleus with a hoechst-tagged phosphorescent ruthenium complex. *ChemBioChem*, **19**, 956-962 (2018).

[28] Yoshihara, T., Yamaguchi, Y., Hosaka, M., Takeuchi, T. & Tobita, S. Ratiometric molecular sensor for monitoring oxygen levels in living cells. *Angew. Chem. Int. Ed.* **51**, 4148–4151 (2012).

[29] Yasukagawa, M., Yamada, K., Tobita, S. & Yoshihara, T. Ratiometric oxygen probes with a cell-penetrating peptide for imaging oxygen levels in living cells. *J. Photochem. Photobiol. A Chem.*, **383**, 111983 (2019).

[30] Liu, Y., Gu, Y., Yuan, W., Zhou, X., Qiu, X., Kong, M., Wang, Q., Feng, W., & Li, F. Quantitative mapping of liver hypoxia in living mice using time-resolved wide-field phosphorescence lifetime imaging. *Adv. Sci.* **7**, 1902929 (2020).

[31] Felder, A. E., Wanek, J., Teng, P. Y., Blair, N. P. & Shahidi, M. A method for volumetric retinal tissue oxygen tension imaging. *Curr. Eye Res.* **43**, 122–127 (2018).

[32] Akiyama, H., Takahashi, I., Shimoda, Y., Mukai, R., Yoshihara, T., & Tobita, S.

Ir(III) complex-based oxygen imaging of living cells and ocular fundus with a gated ICCD camera. *Photochem. Photobiol. Sci*. **17**, 846–853 (2018).

[33] Esipova, T. V., Karagodov, A., Miller, J., Wilson, D. F., Busch, T. M., & Vinogradov, S. A. Two new "protected" oxyphors for biological oximetry: properties and application in tumor imaging. *Anal. Chem*. **83**, 8756–8765 (2011).

[34] Jahn, K., Buschmann, V. & Hille, C. Simultaneous fluorescence and phosphorescence lifetime imaging microscopy in living cells. *Sci. Rep*. **5**, 14334 (2015).

[35] Becker, W., Su, B., Bergmann, A., Weisshart, K. & Holub, O. Simultaneous fluorescence and phosphorescence lifetime imaging. *Proc. SPIE* **7903** (2011).

[36] Zhdanov, A. V., Golubeva, A. V., Okkelman, I. A., Cryan, J. F. & Papkovsky, D. B. Imaging of oxygen gradients in giant umbrella cells: an ex vivo PLIM study. *Am. J. Physiol. Cell Physiol*. **309**, C501–C509 (2015).

[37] Raza, A., Colley, H. E., Baggaley, E., Sazanovich, I. V., Green, N. H., Weinstein, J. A., Botchway, S. W., MacNeil, S., & Haycock, J. W. Oxygen mapping of melanoma spheroids using small molecule platinum probe and phosphorescence lifetime imaging microscopy. *Sci. Rep*. **7**, 10743 (2017).

[38] Kurokawa, H., Ito, H., Inoue, M., Tabata, K., Sato, Y., Yamagata, K., Kizaka-Kondoh, S., Kadonosono, T., Yano, S., Inoue, M., & Kamachi, T. High resolution imaging of intracellular oxygen concentration by phosphorescence lifetime. *Sci. Rep.* **5**, 10657 (2015).

[39] Dmitriev, R. I., Zhdanov, A. V., Nolan, Y. M. & Papkovsky, D. B. Imaging of neurosphere oxygenation with phosphorescent probes. *Biomaterials* **34**, 9307–9317 (2013).

[40] Zhdanov, A. V., Okkelman, I. A., Golubeva, A. V., Doerr, B., Hyland, N. P.,

Melgar, S., Shanahan, F., Cryan, J. F., & Papkovsky, D. B. Quantitative analysis of mucosal oxygenation using ex vivo imaging of healthy and inflamed mammalian colon tissue. *Cell. Mol. Life Sci*. **74**, 141–151 (2017).

[41] Lecoq, J., Parpaleix, A., Roussakis, E., Ducros, M., Houssen, Y. G., Vinogradov, S. A., & Charpak, S. Simultaneous two-photon imaging of oxygen and blood flow in deep cerebral vessels. *Nat. Med*. **17**, 893–898 (2011).

[42] Parpaleix, A., Houssen, Y. G. & Charpak, S. Imaging local neuronal activity by monitoring PO_2 transients in capillaries. *Nat. Med*. **19**, 241–246 (2013).

[43] Spencer, J. A., Ferraro, F., Roussakis, E., Klein, A., Wu, J., Runnels, J. M., Zaher, W., Mortensen, L. J., Alt, C., Turcotte, R., Yusuf, R., Côté, D., Vinogradov, S. A., Scadden, D. T., & Lin, C. P. Direct measurement of local oxygen concentration in the bone marrow of live animals. *Nature* **508**, 269–273 (2014).

[44] Christodoulou, C., Spencer, J. A., Yeh, S. C. A., Turcotte, R., Kokkaliaris, K. D., Panero, R., Ramos, A., Guo, G., Seyedhassantehrani, N., Esipova, T. V., Vinogradov, S. A., Rudzinskas, S., Zhang, Y., Perkins, A. S., Orkin, S. H., Calogero, R. A., Schroeder, T., Lin, C. P., & Camargo, F. D. Live-animal imaging of native haematopoietic stem and progenitor cells. *Nature* **578**, 278–283 (2020).

[45] Spencer, J. A., Ferraro, F., Roussakis, E., Klein, A., Wu, J., Runnels, J. M., Zaher, W., Mortensen, L. J., Alt, C., Turcotte, R., Yusuf, R., Côté, D., Vinogradov, S. A., Scadden, D. T., & Lin, C. P. Two-photon phosphorescence lifetime microscopy of retinal capillary plexus oxygenation in mice, *J. Biomed. Opt*. **23**, 126501 (2018).

[46] Hasebe, N., Deguchi, Y., Murayama, S., Yoshihara, T., Horiuchi, H., Okutsu, T., & Tobita, S. Phosphorescence quenching of neutral and cationic iridium(III)

complexes by molecular oxygen and aromatic electron acceptors. *J. Photochem. Photobiol. A Chem.* **324**, 134–144 (2016).

[47] Zhang, S., Hosaka, M., Yoshihara, T., Negishi, K., Iida, Y., Tobita, S., & Takeuchi, T. Phosphorescent light-emitting iridium complexes serve as a hypoxia-sensing probe for tumor imaging in living animals. *Cancer Res.* **70**, 4490–4498 (2010).

[48] Yoshihara, T., Hosaka, M., Terata, M., Ichikawa, K., Murayama, S., Tanaka, A., Mori, M., Itabashi, H., Takeuchi, T., & Tobita, S. Intracellular and in vivo oxygen sensing using phosphorescent IR(III) complexes with a modified acetylacetonato ligand. *Anal. Chem.* **87**, 2710–2717 (2015).

Chapter 2

Experimental Section

2-1   Materials

All reagents and solvents used in synthesis and optical measurements were purchased from Kanto Chemical, Wako Pure Chemical, Tokyo Chemical Industry or Sigma-Aldrich, and were used as received. The Ir(III) complexes, BTP, BTPDM1 and BTP-PEG$_{48}$ were synthesized and characterized according to the methods described in the literature [1-3]. The synthesis methods of other Ir(III) complexes, BTP-3OH and (btp)$_2$Ir(acac-2OH), are described in Chapter 3 and 4. ^{1}H NMR and mass spectrometry (MS) were used to characterize all products. Acetonitrile (MeCN, Kanto Chemical, spectroscopic grade) was used as received. Deionized water was purified using a water purification system (Simplicity UV, Merck-Millipore).

Antimycin A from *Streptomyces* sp. (AntA), carbonyl cyanide 4-(trifluoromethoxy) phenylhydrozone (FCCP, 98%), and L-glutatione reduced (GSH, 98%) were purchased from Sigma-Aldrich. Cell Counting Kit-8 (CCK-8) was purchased from Dojindo Laboratories. NH$_4$Cl (Kanto Chemical, special grade) were used as received. (FITC)-conjugated *Lycopersicon esculentum* lectin (FITC-lectin) was purchased from Vector Laboratories Inc. (USA) and used without further purification.

^{1}H-NMR spectra were recorded with a JEOL JNM-ECS400 (400 MHz) spectrometer in DMSO-d_6. ^{1}H-NMR chemical shifts were referenced to tetramethylsilane. The apparent resonance multiplicity was described as s (singlet), d (doublet), dd (double doublet), t (triplet) and m (multiplet). ESI-MS spectra were recorded on an API 2000 mass spectrometer (Applied Biosystems).

2-2   Photophysical Properties of Probes in Solutions

Absorption spectra of probes in solutions were recorded on a UV/Vis

spectrophotometer (Ubest-V550, JASCO). Emission spectra were recorded with a system that consisted of a monochromatized Xe arc lamp, a sample holder, and a photonic multichannel analyzer (C10027-01, Hamamatsu Photonics). This system was fully corrected for spectral sensitivity between 200-950 nm. Fluorescence and phosphorescence lifetimes in solutions were measured with a lifetime measurement system (Quantaurus-Tau C11367G, Hamamatsu Photonics) based on the time-correlated single photon counting (TCSPC) method. Fluorescence and phosphorescence quantum yield in solutions were measured with an absolute photoluminescence quantum yield measurement system (C9920-02, Hamamatsu Photonics) that consisted of a Xe arc lamp, a monochromator, an integrating sphere, a multichannel detector, and a personal computer [4].

2-3   Liposome Experiments

Lipid membranes of L-α-dimyristoyl-phosphatidylcholine (DMPC, Sigma-Aldrich) were formed as small unilamellar vesicles prepared by ethanol injection method [5]. An ethanolic solution of DMPC (30 mM), and a DMSO stock solution of each probe (600 μM) were injected rapidly into Tris/HCl buffer or HEPES buffer. The final concentration of DMPC and the probe were 10 mM and 10 μM, respectively. The pH in the solution were prepared using hydrochloric acid and sodium hydroxide solution.

2-4   Phosphorescence Lifetime Measurements Using TCSPC System

The phosphorescence lifetime of BTP-PEG$_{48}$ in solutions was measured using a lifetime measurement system consisting of an inverted microscope (IX71, Olympus) with a TCSPC system (Quantaurus-Tau C11367, Hamamatsu Photonics), a laser diode

(iBeam smart-S 488-S, Topica Photonics; wavelength: 488 nm, pulse width: 20 ns, repetition rate: 40 or 15 kHz) as the excitation light source and an O_2 concentration-changeable incubator with a temperature controller (Inub-Onics-F1-H2, GM-8000, Tokai Hit) (Fig. 2-1). BTP-PEG$_{48}$ in solutions was excited using custom filter setting (excitation: a bandpass filter (488±10 nm), emission: a long-pass filter (>590 nm)).
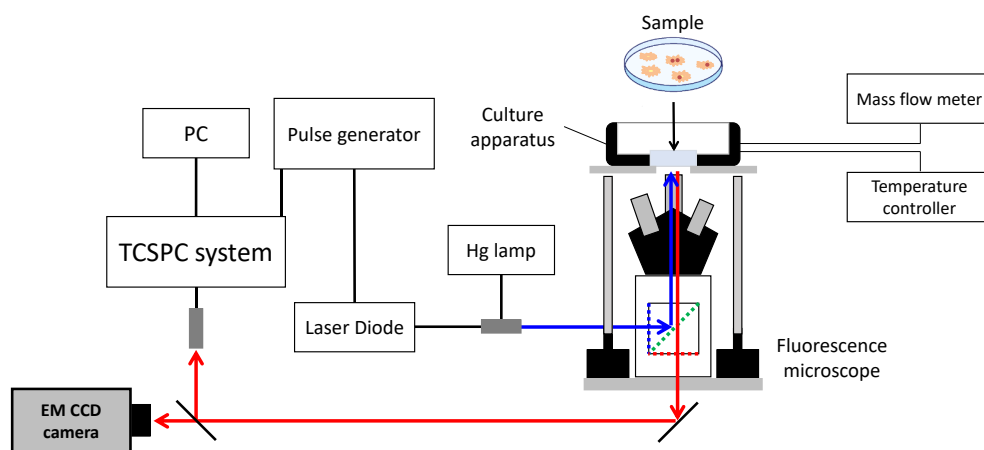
Fig. 2-1 Schematic diagram of a TCSPC system.

2-5　Cell and Cell Spheroid Cultures

Human colorectal adenocarcinoma (HT-29) cells and human uterine cancer-derived HeLa cells were purchased from the American Type Culture Collection (ATCC). Alpha mouse liver 12 (AML 12) cells were kindly provided by Prof. T. Inagaki of the Laboratory of Epigenetics and Metabolism, IMCR, Gunma University. Human kidney 2 (HK-2) cells were kindly provided by Prof. M. Nangaku of the Graduate School of Medicine, the University of Tokyo.

HT-29 cells were incubated in McCoy's 5A medium (Gibco) containing 10% fetal bovine serum (FBS), penicillin (50 units/mL), and streptomycin (50 μg/mL). AML 12 cells and HK-2 cells were incubated in a mixture of Dulbecco's Modified Eagle's Medium (DMEM, Gibco) and Ham's F-12 Nutrient Mixture containing 10% FBS, penicillin (50 units/mL), and streptomycin (50 μg/mL). All cells were grown in at 37°C a humidified 5% CO_2 enriched atmosphere. In PLIM measurements, all cells were cultured on glass-based dishes, and the medium were gently washed 3 times with McCoy's 5A or DMEM/F-12 without phenol red and FBS prior to the measurements.

HT-29 cell spheroids were grown using a low attachment 96-well NanoCulture Plate (NCP; NCP-LH96, ORGANOGENICS) with a micro-honeycomb pattern on the film that comprises the bottom of the plate. McCoy's 5A medium (100 μL) containing 10% FBS, penicillin (50 units/mL), and streptomycin (50 μg/mL) was added to each well in the NCP, and the NCP was centrifuged at 10×100 rpm for 5 min to remove the bubbles in the media in the wells. Then HT-29 cells (1.0×10^5 cells/mL) suspended in 100 μL McCoy's 5A medium were added to each well in the NCP. The cells were incubated in the NCP at 37°C, 5% CO_2 for 4 days to form the HT-29 cell spheroids. In PLIM measurements of cell spheroids, HT-29 sell spheroids were incubated in the McCoy's 5A medium containing a final concentration of 500 nM BTPDM1 or BTP-

3OH for 24 h at 37°C, 5% CO_2 prior to the measurements.

2-6 Emission Intensity Measurement Using a Microplate Reader

HT-29 cells (3.0×10^4 cells/well) were seeded into a 96-well flat bottom plates (Greiner) and incubated for 48 h. The cells were incubated with BTP, BTPDM1 or BTP-3OH (5 μM) for 2 h at 37°C under a 5% CO_2 atmosphere. The cells were gently washed 3 times with McCoy's 5A medium without phenol red, and then the emission intensities of the probes incorporated into cells were measured using a microplate reader (Infinite 200 PRO, Tecan) equipped with a gas control module (GCM, Tacan).

2-7 Subcellular Localization of O_2 Probes

HeLa cells were incubated in DMEM (Gibco) with 10% FBS, penicillin (50 units/mL), and streptomycin (50 μg/mL), and were grown under a 5% CO_2 atmosphere at 37°C. The cells were seeded into glass bottom imaging dishes (Greiner) and allowed to adhere for 24 h, incubated with BTPDM1 (500 nM) or BTP-3OH (1 μM) for 2 h. The cells were gently washed 3 times with DMEM, and then the medium was replaced with DMEM (FluoroBrite, Gibco) without FBS prior to measurements of microscopic images. Luminescence microscopic images were obtained with an inverted fluorescence microscope (IX71, Olympus) equipped with an electron multiplying CCD (charge coupled device) camera (Evolve 512, PHOTOMETRICS) driven by MetaMorph software.

2-8 Evaluation of Cytotoxicity of O_2 Probes Using WST Assays

HT-29 cells (2.5×10^4 cells/well) were seeded into a 96-well flat bottom plates (Greiner) and incubated for 48 h. The HT-29 cells were incubated with various

concentrations of BTPDM1 or BTP-3OH for 24 h at 37°C under a 5% CO_2 atmosphere. After removing the medium, the cells were washed gently 3 times with McCoy's 5A medium with and without phenol red, respectively. Cell Counting Kit-8 reagent (CCK-8, Dojindo) was added to each well, and incubation was continued for 1 h [6]. The absorbance at 450 nm of each well referenced at 650 nm was recorded using a microplate reader (Infinite 200 PRO, Tecan). Cell viability (% of control) was evaluated as $(A_{sample} - A_{blank})/(A_{control} - A_{blank}) \times 100$, where A_{sample} is the absorbance of cells exposed to the probe, $A_{control}$ is the absorbance of cells without probe, and A_{blank} is the absorbance of wells without cells.

2-9   Mitochondrial Membrane Potential

HT-29 cells (3.0×10^4 cells/well) were seeded into a 96-well flat bottom plates (Greiner) and incubated for 48 h, and then the cells were incubated with BTPDM1 or BTP-3OH (1 μM) for 2h at 37°C. The medium was removed, and the cells were washed gently 3 times with McCoy's 5A medium without phenol red. 5,5′,6,6′-tetrachloro-1,1′-3,3′-tetraethyl-benzimidazolylcarbocyanine iodide (JC-1, Thermo Fisher Scientific) (5 μM) was added to each well, and incubation was continued for 30 min. The medium was removed, and the cells were washed gently 3 times with McCoy's 5A medium without phenol red. The emission intensities of JC-1 were recorded on a microplate reader (Infinite 200 PRO, Tecan) equipped with a gas control module (GCM, Tecan). The excitation wavelength was 488 nm, and the monitor wavelength was 595 nm for Red emission (aggregate) and 540 nm for green emission (monomer).

2-10 FLIM/PLIM Measurements of Cultured Cells and Cell Spheroids

FLIM and PLIM images were measured using an inverted fluorescence microscope (IX73, Olympus) equipped with a picosecond diode laser (BDL-SMC, Becker & Hickl; wavelength: 488 nm, pulse width: 40-90 ps, repetition rate: 50 MHz) and a confocal scanning system (DCS-120, Becker & Hickl) (Fig. 2-2). A 4× objective (UPlanSApo; NA 0.16, Olympus), 10× objective (UPlanSApo; NA 0.40, Olympus), 20× objective (UCPlanFLN; NA 0.70, Olympus), 40× oil objective (UPlanFLN; NA 1.30, Olympus), or 100× oil objective (UPlanSApo; NA 1.40, Olympus) were used for FLIM/PLIM measurements. The emission, as guided through a 1 mm pinhole, was collected at >590 nm long-pass filter and 535±50 nm bandpass filter, and detected with a hybrid detector module (HPM-100-40, Becker & Hickl). Time-resolved emission measurements were performed with a time-correlated single photon counting (TCSPC) system (Simple-Tau-150-DX, Becker & Hickl). The emission signals were acquired at a resolution of 128 × 128 pixels for PLIM and 256 × 256 pixels for FLIM, and the decay curve in each pixel was fitted to single- or double-exponential decay function. with lifetimes of τ_1 and τ_2, and amplitudes A_1 and A_2, respectively (Eq. 2-1).

$$I_p(t) = A_1 \exp\left(-\frac{t}{\tau_1}\right) + A_2 \exp\left(-\frac{t}{\tau_2}\right) \qquad (2\text{-}1)$$

When the emission decay did not follow the exponential decay, the emission lifetime was assessed using the following amplitude-averaged lifetime

$$\langle \tau \rangle_{\mathrm{amp}} = \frac{A_1 \tau_1 + A_2 \tau_2}{A_1 + A_2} \qquad\qquad (2\text{-}2)$$

SPCImage data analysis software (Becker and Hickl) was used for analysis of FLIM
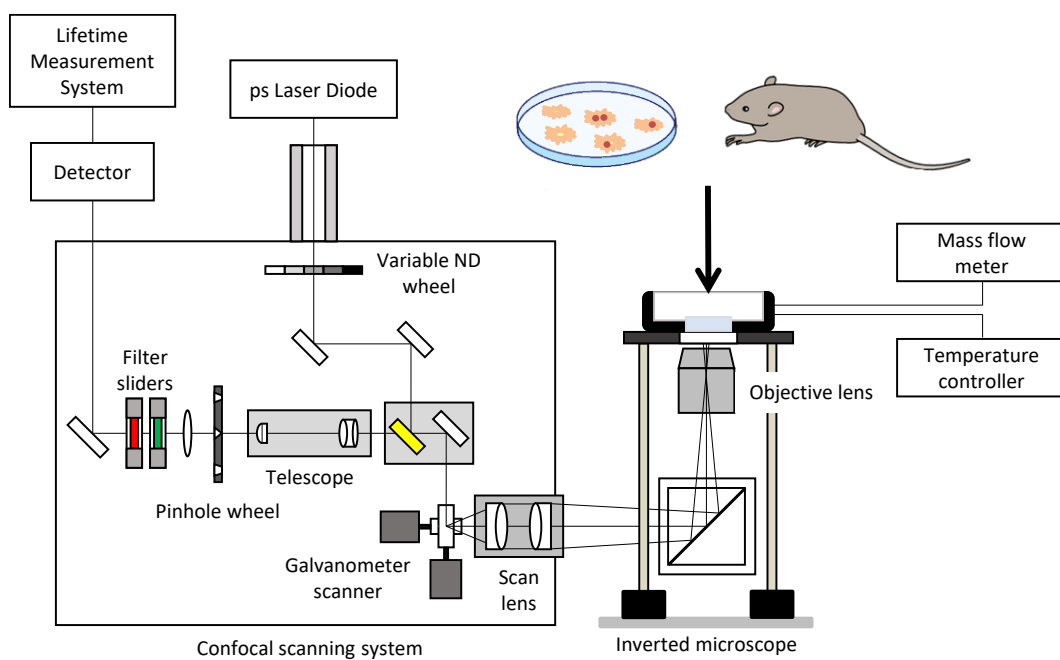
and PLIM images.

Fig. 2-2 Schematic diagram of a confocal PLIM system used in this study. A dish containing cells or cell spheroids was placed on the top stage of the inverted microscope. In animal experiments, exposed liver or kidney of mice was placed on a thin glass plate on a microscope stage, and the surface was irradiated with the excitation laser light from below.

2-11 Calibration of the Phosphorescence Lifetime in Cells

The oxygen partial pressure (pO_2) in cells was obtained from the phosphorescence lifetime, based on a calibration using cultured cells. HT-29 cells, AML 12 cells or HK-2 cells were seeded on glass-based dishes and stained with BTPDM1 (500 nM, 2 h) or BTP-3OH (500 nM, 2 h). PLIM images were acquired for the stained cells at 21%, 15%, 10%, 5% and 0% O_2 in an incubator at 37°C. Here, in the 5-21% O_2 experiments, cells were incubated with AntA (10 μM, >0.5 h) to block cellular respiration, and in the 0% O_2 experiments, fresh medium containing Na_2SO_3 (500 mM) was used to remove existing O_2 in the medium. The average phosphorescence lifetimes of each the PLIM image taken under different pO_2 was plotted according to the Stern-Volmer equation (Eq. 1-1) to determine the bimolecular quenching rate constant, k_q. The pO_2 of biological targets (cells, cell spheroids, and tissues) were obtained by measuring the phosphorescence lifetime (τ_p) and subsequent calculations based on Eq. 1-2 using the k_q and τ_p^0 determined as mentioned above.

2-12 FLIM/PLIM Measurements of Living Mice

All protocols for animal experiments were approved by the Ethical Committee on Animal Experiments of Gunma University (18-018), and all animal experiments were conducted in accordance with the institutional guidelines.

PLIM experiments of hepatic tissues in Chapter 4 were conducted using BTPDM1 and BTP-3OH as O_2 probes. Six- to eight-week-old *Balb/c* male mice (CLEA Japan) were fasted for one day before the experiments. After general anesthesia using pentobarbital, probe solution (200 μL) containing 250 nmol BTPDM1 or BTP-3OH in 10% DMSO/saline was injected into tail vein of mice, and the abdomen was opened by median incision to expose the liver approximately 10 minutes before PLIM

measurements. The exposed liver was gently placed on the cover slip above the inverted microscope stage to ensure that the mouse was stationary, and then the laser beam was confocal-scanned to obtain PLIM images. PLIM images were analyzed with SPCImage data analysis software (Becker and Hickl).

FLIM/PLIM experiments of kidney tissues in Chapter 5 were carried out using BTPDM1 as an O_2 probe and FITC-lectin as a vascular imaging reagent. Eight-week-old *Balb/c* male mice (Japan SLC Inc.) were fasted for one day before the experiment. After general anesthesia using pentobarbital, probe solution (200 µL) containing 250 nmol BTPDM1 in 10% DMSO/saline and FITC-lectin (125 µg/mouse) in saline were injected into the tail vein, a flank incision was made, and the left kidney was exposed for approximately 15 minutes before FLIM/PLIM measurements. The left kidney was placed on the cover slip above the inverted microscope stage, and then the PLIM images were acquired and analyzed in the same manner as for the liver. The effect of inspiratory O_2 concentration on renal oxygenation was examined using a digital gas mixing system (GM-8000, Tokai-Hit) which can supply a gas with an arbitrary pO_2 using an O_2/N_2 mixed gas.

2-13 Emission Spectra of O_2 Probes in Cells and Living Tissues

The emission spectra of cultured cells and living tissues were measured using a fluorescence microscope (IX71, Olympus) equipped with a spectrometer (USB-4000, Ocean Optics), a 100 W mercury lamp as the excitation light source and an O_2 concentration-changeable incubator (Inub-Onics-F1-H2, GM-8000, Tokai Hit). The emission images and spectra of cultured cells stained with and without Ir(III) complexes or living tissues of the mice administered with and without Ir(III) complexes were obtained using custom filter setting.

References

[1]   Zhang, S., Hosaka, M., Yoshihara, T., Negishi, K., Iida, Y., Tobita, S., & Takeuchi, T. Phosphorescent light-emitting iridium complexes serve as a hypoxia-sensing probe for tumor imaging in living animals. *Cancer Res.* **70**, 4490–4498 (2010).

[2]   Yoshihara, T., Hosaka, M., Terata, M., Ichikawa, K., Murayama, S., Tanaka, A., Mori, M., Itabashi, H., Takeuchi, T., & Tobita, S. Intracellular and in vivo oxygen sensing using phosphorescent Ir(III) complexes with a modified acetylacetonato ligand. *Anal. Chem.* **87**, 2710–2717 (2015).

[3]   Yoshihara, T., Hirakawa, Y., Nangaku, M. & Tobita, S. Hydrophilic Ir(III) Complexes for In vitro and In vivo Oxygen Imaging, RSC Detection Science: Quenched-phosphorescence Detection of Molecular Oxygen: Applications in Life Sciences, ed. Papkovsky, D. B. & Dmitriev, R. I. Royal Society of Chemistry, 2018, Chap. 4, pp.71-90.

[4]   Suzuki, K., Kobayashi, A., Kaneko, S., Takehira, K., Yoshihara, T., Ishida, H., Shiina, Y., Oishi, S., & Tobita, S. Reevaluation of absolute luminescence quantum yields of standard solutions using a spectrometer with an integrating sphere and a back-thinned CCD detector. *Phys. Chem. Chem. Phys.* **11**, 9850–9860 (2009).

[5]   Batzri, S. & Korn, E. D. Single bilayer liposomes prepared without sonication, *Biochim. Biophys. Acta - Biomembr.* **298**, 1015–1019 (1973).

[6]   Yoshihara, T., Murayama, S., Masuda, T., Kikuchi, T., Yoshida, K., Hosaka, M., & Tobita, S. Mitochondria-targeted oxygen probes based on cationic iridium complexes with a 5-amino-1,10-phenanthroline ligand. *J. Photochem. Photobiol. A: Chem.* **299**, 172–182 (2015).

Chapter 3

O$_2$ Imaging of Cell and Cell Spheroids

3-1　Introduction

In Chapter 3, an *in vivo* O_2 imaging technique using small-molecule probes is developed by investigating the O_2 distribution in cells and cell spheroids by PLIM measurements with two structurally related Ir(III) complexes, BTPDM1 and BTP-3OH ((btp-OH)$_3$Ir) (Fig. 3-1). Both complexes have a benzothienyl group, which predominately controls photophysical properties as the main ligand, and BTPDM1 also has acetylacetone as an ancillary ligand. BTPDM1 and BTP-3OH are imparted with hydrophilicity by the dimethylamino group on the acetylacetone ligand and the hydroxybenzyl group on the benzothienyl ligand, respectively, in order to facilitate cellular uptake.

First, a PLIM system optimized for O_2 imaging of cells and living tissues is constructed based on an inverted microscope equipped with a confocal laser scanning system and a lifetime measurement system, and its basic performance is evaluated by using a water-soluble Ir(III) complex, BTP-PEG$_{48}$. Next, the photophysical properties and oxygen sensitivity of BTPDM1 and BTP-3OH are compared in solutions and in cultured cells. Then, the cellular uptake efficiency, subcellular localization, and cytotoxicity of BTPDM1 and BTP-3OH are examined using HT-29 cells and HeLa cells. Furthermore, a calibration method for the relationship between phosphorescence lifetime and oxygen partial pressure is investigated using cultured cells. Based on these results, the capabilities of these probes for measuring the O_2 distribution in 3D cell spheroids are investigated by PLIM measurements.
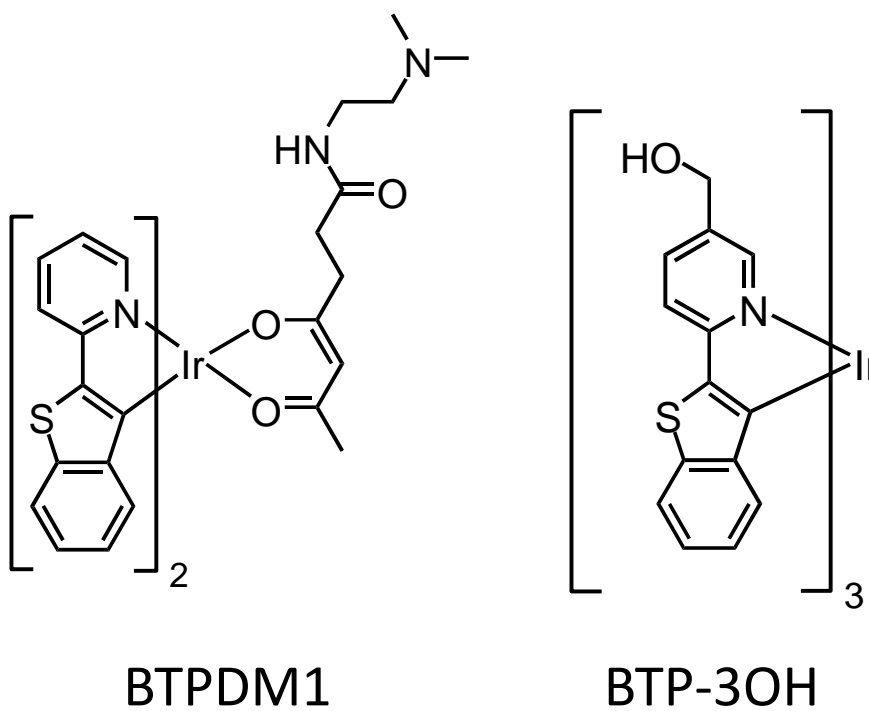
BTPDM1   **BTP-3OH**

Fig. 3-1 Chemical structures of BTPDM1 and BTP-3OH.

3-2 Results and Discussion

3-2-1 Synthesis and Characterization of BTP-3OH

The complex BTP-3OH was synthesized from BTP-COOEt by the synthetic route in Scheme 3-1 according to the literature [1]. The target product was characterized by ^{1}H NMR and mass spectrometry. Details of the synthetic procedure and analytical data are given in Appendix 3-1.
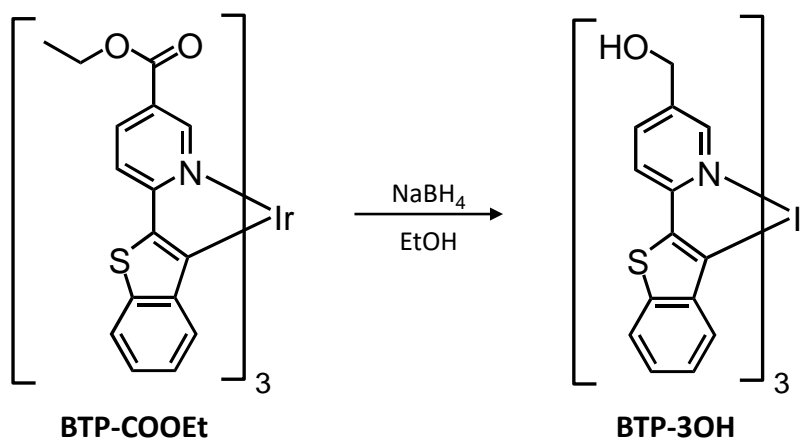
Scheme 3-1 Synthesis of BTP-3OH.

3-2-2 Setup of PLIM System and Evaluation of its Basic Performance

Comparison of lifetimes obtained by PLIM and TCSPC system

The PLIM system constructed in this study consists of an inverted fluorescence microscope, confocal scanning system equipped with a picosecond diode laser (488 nm, pulse width: 40-90 ps, repetition rate: 50 MHz), and lifetime measurement system based on the single-photon counting or multichannel scaler (Fig. 2-2). This system

enables simultaneous measurements of FLIM and PLIM images. To assess the reliability of our PLIM system, the phosphorescence lifetimes obtained by using our PLIM system were compared with those obtained by conventional TCSPC measurements. A hydrophilic Ir(III) complex BTP-PEG$_{48}$ (Fig. 3-2) synthesized in our laboratory was used as the phosphorescent molecule. It shows red emission with the maximum at 646 nm in H_2O by 488 nm excitation.

A PBS solution of BTP-PEG$_{48}$ (10 μM) was placed in a Petri dish and set in an O_2-concentration-changeable incubator on the microscope stage of the PLIM system (Fig. 2-2) and TCSPC system (Fig. 2-1) to measure the lifetime under 21% and 0% O_2 conditions. The 0% O_2 experiment was performed under nitrogen gas flow while removing residual oxygen in the solution by adding Na_2SO_3 (final concentration: 500 mM) to the solution. As shown in Table 3-1, the phosphorescence lifetimes of BTP-PEG$_{48}$ solution obtained by PLIM and TCSPC systems showed good agreement both under 21% and 0% O_2 conditions, demonstrating the reliability of the lifetime obtained by PLIM measurements.

Effect of Peak Counts in Phosphorescence Decay Profile to PLIM Images

In microscopic lifetime measurements of cells and tissues using an optical probe, photon counts per unit time are usually limited to very low levels because only small amount of probe molecules is delivered to the target, and the observation area is confined to a very small space. Therefore, the effect of peak photon count on the PLIM image was investigated using BTP-PEG$_{48}$ dissolved in McCoy's 5A medium which is often used in cell culture. In Fig. 3-3A, the PLIM images of BTP-PEG48 solution measured under 21% O_2 condition are displayed on a color scale with a lifetime range of 0.9-1.2 μs. The upper images were taken for the peak photon counts 100, 500 and

1000 without pixel binning, and the lower figures were obtained with a spatial binning with factor 5 to increase the signal-to-noise ratio. The corresponding decay curves at one pixel are shown in Fig. 3-3B. It should be noted here that the sample is a solution in which the probe molecules are uniformly dissolved, and thus the PLIM image should also be uniform. The image with peak counts of 100 without binning shows fluctuations in lifetime, while it can be seen that the lifetime images with binning 5 are almost uniform even with low peak count. Similar results were obtained for the BTP-PEG$_{48}$ solution under the 0% O$_2$ condition (Fig. 3-4), although the uniformity was inferior to that under 21% O$_2$ condition.

These results indicate that the PLIM image is improved in accuracy as the number of accumulated photons increases, and even if the peak count is only 100 it can be improved by effective use of spatial binning. The time required to obtain a peak count of 1000 in the BTP-PEG$_{48}$ solution was 16 minutes under 21% O$_2$ and 10 minutes under 0% O$_2$ condition. In the following PLIM measurements of cells and living tissues, repeated laser pulse irradiation for 10 minutes or more may cause serious damage to the biological target, and thus the appropriate number of photons was selected while keeping the irradiation time as short as possible.
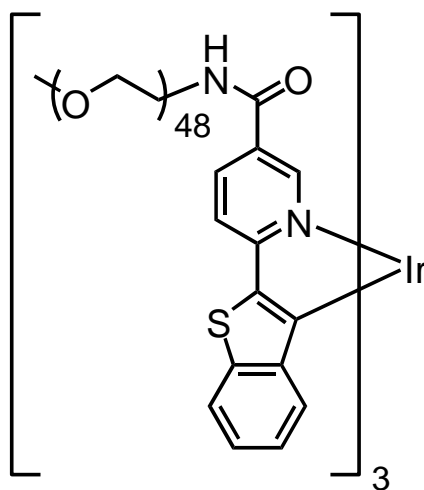
Fig. 3-2 Chemical structure of BTP-PEG$_{48}$.

Table 3-1 Phosphorescence lifetime of 10 μM BTP-PEG48 in PBS under 21% and 0% O$_2$ condition in an incubator.

pO$_2$ (%)	Measurement method	$<\tau_p>$ (μs)
21	PLIM	1.14 ± 0.01
	TCSPC	1.10 ± 0.02
0	PLIM	4.61 ± 0.01
	TCSPC	4.67 ± 0.05
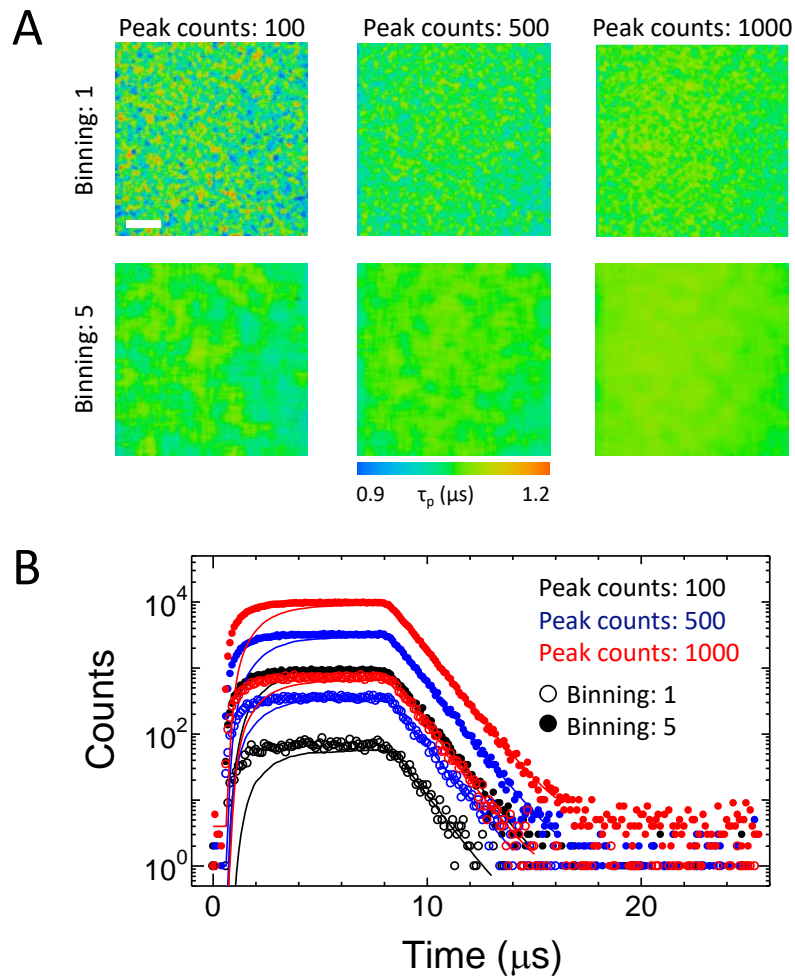
Fig. 3-3 (A) PLIM images of BTP-PEG$_{48}$ in McCoy's 5A medium under 21% O$_2$ in an incubator. Scale bar: 100 μm. **(B)** Phosphorescence decay curve of BTP-PEG$_{48}$ in McCoy's 5A medium under 21% O$_2$.
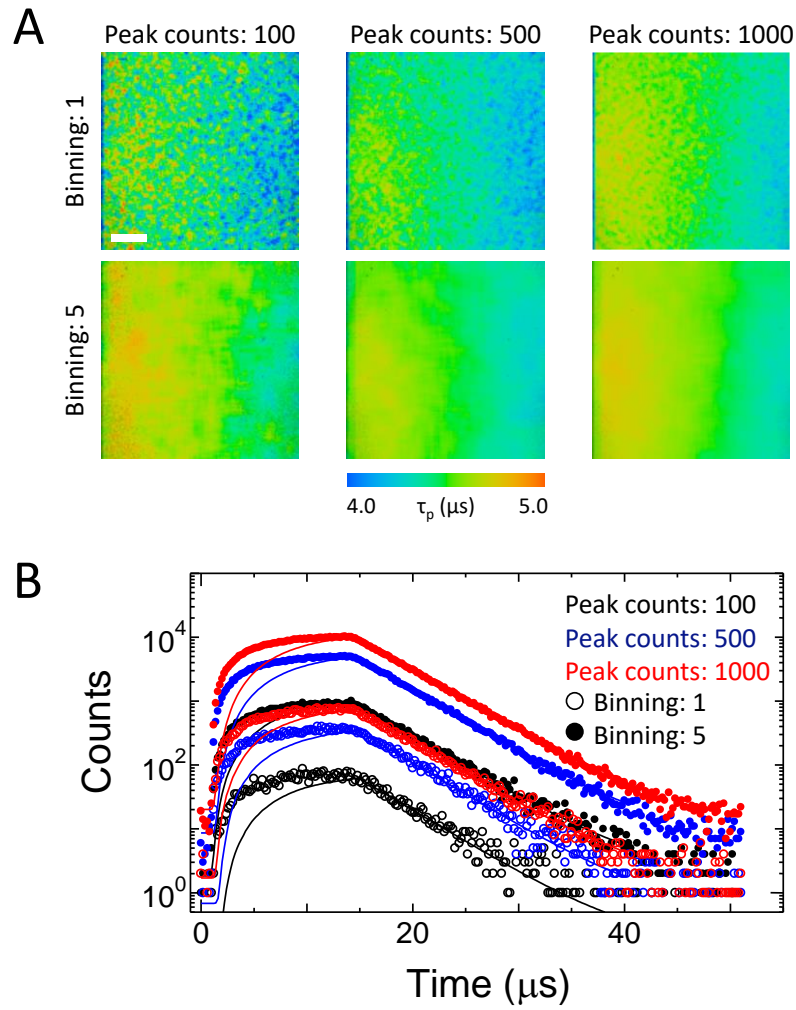
Fig. 3-4 (A) PLIM images of BTP-PEG$_{48}$ in McCoy's 5A medium under 0% O$_2$ in an incubator. Scale bar: 100 μm. **(B)** Phosphorescence decay curve of BTP-PEG$_{48}$ in McCoy's 5A medium under 0% O$_2$.

3-2-3 Photophysical Properties of BTPDM1 and BTP-3OH in Solution

First, the photophysical properties of BTPDM1 and BTP-3OH as O_2 probes were examined in MeCN. Among various photophysical characteristics, emission brightness and O_2 sensitivity are the basic characteristics that are particularly important for an optical O_2 probe. The emission brightness of the probes under the same concentration can be evaluated by the product ($\varepsilon\Phi_p^0$) of the molar absorption coefficient (ε) at the excitation wavelength and the phosphorescence quantum yield (Φ_p^0) under the absence of oxygen, and the O_2 sensitivity by $k_q\tau_p^0$, where k_q and τ_p^0 are the bimolecular quenching rate constant by O_2 and the phosphorescence lifetime under the absence of oxygen.

As shown in Fig. 3-5, The first absorption band of BTPDM1 appears at around 476 nm in MeCN, which originates from singlet metal-to-ligand-charge-transfer (^{1}MLCT) transition. This band is slightly blue-shifted in BTP-3OH, giving a smaller ε value (2,800 $dm^3mol^{-1}cm^{-1}$) compared with that (5,400 $dm^3mol^{-1}cm^{-1}$) of BTPDM1 at the excitation wavelength (488 nm) in the present PLIM measurements. BTPDM1 and BTP-3OH exhibit red emission extending to the near infrared region and give vibrational structures with maximum wavelengths at 612 and 601 nm, respectively. Both complexes are highly emissive in MeCN (Φ_p^0 = 0.26 for BTPDM1 and 0.28 for BTP-3OH). Judging from the ε values at 488 nm and the almost equal Φ_p^0, BTPDM1 is superior to BTP-3OH in brightness for excitation at 488 nm. The O_2 sensitivity of a probe in solution can be evaluated experimentally from the ratio (τ_p^0/τ_p) of the phosphorescence lifetimes under deaerated and aerated conditions. The obtained τ_p^0/τ_p values of BTPDM1 and BTP-3OH in MeCN were 72 and 97, and the k_q values were calculated to be 7.59×10^4 $mmHg^{-1}s^{-1}$ for BTPDM1 and 8.22×10^4 $mmHg^{-1}s^{-1}$ for

BTP-3OH (Table 3-2). Using the solubility of oxygen in MeCN at an oxygen partial pressure (pO_2) of 0.21 atm [2], the quenching rate constant can be converted from pressure units to concentration units. The converted k_q values (6.38×10^9 $M^{-1}s^{-1}$ for BTPDM1 and 6.91×10^9 $M^{-1}s^{-1}$ for BTP-3OH) were close to the diffusion-controlled rate of bimolecular reactions in MeCN [2], indicating that both complexes are highly quenched by oxygen. As described in Sec. 1-3, the phosphorescence quenching of Ir(III) complexes by molecular oxygen occurs not only by energy transfer but also by charge transfer from the triplet Ir(III) complex to O_2 [3]. As a result, Ir(III) complexes show much larger k_q values compared with metalloporphyrins and Ru(II) complexes. The O_2 sensitivity of BTP-3OH seems to be slightly higher than that of BTPDM1 owing to the longer intrinsic lifetime and larger k_q value of BTP-3OH. The intrinsic lifetimes (5-10 μs) of BTPDM1 and BTP-3OH are much shorter than those (10-100 μs) of Pt-porphyrins, but longer than those of typical Ru(II) complexes used as O_2 probes [4], and thus the O_2 sensitivity of BTPDM1 and BTP-3OH is considered to be comparable with Pt-porphyrins and higher than Ru(II) complexes. In addition, the moderately long lifetimes of the Ir(III) complexes have the advantage of increasing the counting efficiency in PLIM measurements and thus shortening the image acquisition time.
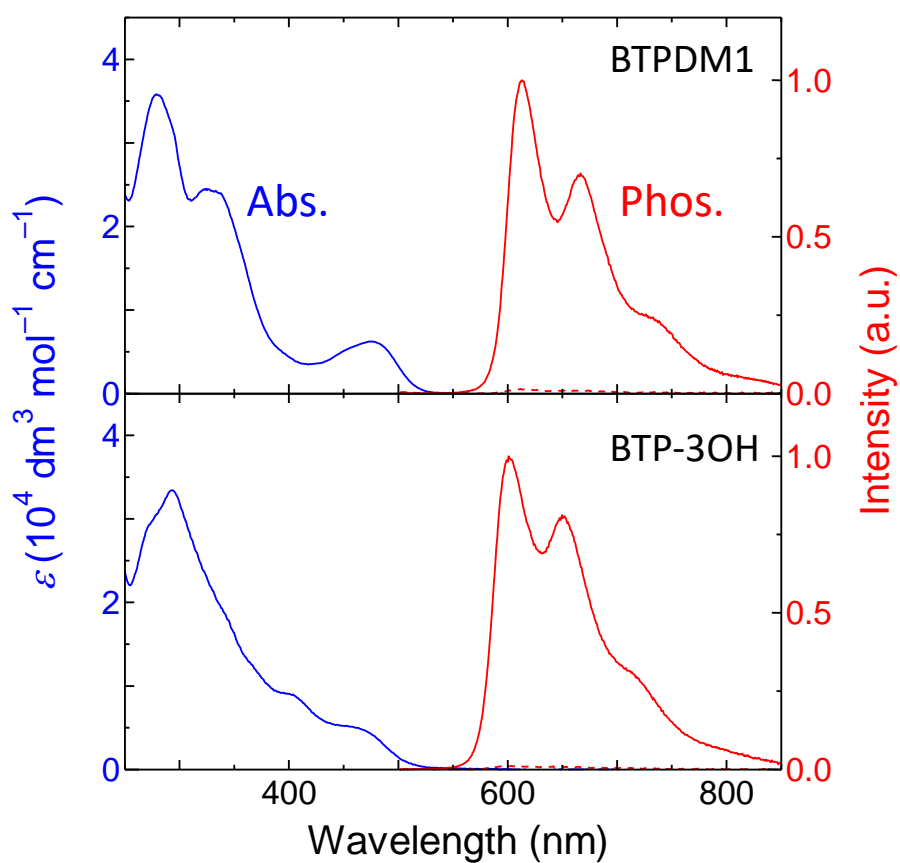
Fig. 3-5 Absorption and phosphorescence spectra of BTPDM1 and BTP-3OH in MeCN at room temperature. The phosphorescence spectra were taken in both degassed (solid line) and aerated (dashed line) solutions.

Table 3-2 Photophysical properties of BTPDM1 and BTP-3OH in MeCN at room temperature[a].

probe	λ_{abs}^{max} (nm)	λ_{phos}^{max} (nm)	τ_p^0 (μs)	τ_p (ns)	τ_p^0/τ_p	Φ_p^0	Φ_p	k_q (10^4 mmHg^{-1}s^{-1})
BTPDM1	476	612	5.86	81.4	72	0.26	0.006	7.59
BTP-3OH	-	601	7.31	75.4	97	0.28	0.005	8.22

[a] τ_p^0 and Φ_p^0 denote the phosphorescence lifetime and quantum yield taken in degassed solutions, and τ_p and Φ_p denote the phosphorescence lifetime and quantum yield taken in aerated solutions.

3-2-4 Characterization of BTPDM1 and BTP-3OH as Intracellular O_2 Probes

Next, characteristics of BTPDM1 and BTP-3OH as intracellular O_2 probes were evaluated using cultured cells. To evaluate the cellular uptake efficiencies of BTPDM1 and BTP-3OH, the emission intensities of human colorectal adenocarcinoma (HT-29) cells incubated with these complexes (5 μM, incubation time: 2 h) were compared using a plate reader. Here, their prototype complex BTP ((btp)$_2$Ir(acac); btp = benzothienylpyridine, acac = acetylacetone) [5] were used as a reference compound. The emission intensities of each complex under 21% and 2.5% O_2 conditions were corrected for the number of HT-29 cells in each well and the ε values (4700, 5400, and 2800 $M^{-1}cm^{-1}$ for BTP, BTPDM1 and BTP-3OH) at 488 nm. The relative emission intensities after these corrections (Fig. 3-6) suggest that the cellular uptake efficiency was greatly improved in BTPDM1 and BTP-3OH compared with BTP by introducing a hydrophilic dimethylamino and hydroxyl group, respectively.

The subcellular localizations of BTPDM1 and BTP-3OH were investigated by co-staining experiments with a lysosome-specific tracker (LysoTracker Green) and an ER-specific tracker (ERTracker Green), using HeLa cells. The co-stained images shown in Fig. 3-7 show preferential accumulation of BTPDM1 to lysosomes and BTP-3OH to endoplasmic reticulum (ER). These localization behaviors were confirmed by the Pearson's correlation coefficient which were calculated to be 0.96 for BTPDM1 and 0.98 for BTP-3OH. Both complexes taken up into cells are presumed to accumulate in the organelle membrane because of their lipophilicity. The cytotoxicity of BTPDM1 and BTP-3OH evaluated with WST assay (incubation time: 24 h under the presence of the probe) revealed that the median lethal doses (LC$_{50}$) of BTPDM1 and BTP-3OH for HT-29 cells were 10-15 μM and ~30 μM (Fig. 3-8A). In addition,

analysis of mitochondrial membrane potential using JC-1 dye (Fig. 3-8B) showed that the mitochondrial membrane potential was almost unaffected by BTPDM1 or BTP-3OH loading (1 μM, 2 h). In typical experiments in this study, the cells were incubated with the probes (500 nM or 1 μM) for 2 h prior to microscopic measurements. Therefore, under the present experimental conditions, the effect of the probes on cell activity is considered to be sufficiently small.

Photostability is another important characteristic required for an intracellular O_2 probe. Here the photostability of BTPDM1 and BTP-3OH in cells was examined by taking emission images of HT-29 cells under continuous 488 nm laser pulse irradiation with our PLIM system. The cells were incubated with BTPDM1 or BTP-3OH (1 μM) for 2 h under 21% or 2.5% O_2 conditions, and PLIM images of the HT-29 cells were taken at every 50 scans until 550 scans (Fig. 3-9). During this irradiation time, the phosphorescence lifetimes of BTPDM1 and BTP-3OH were almost constant, although the phosphorescence intensity changed slightly by 488 nm light irradiation. Also, no significant change was observed in the cell morphology. In this study, the signals accumulated with 50 scans were usually averaged to obtain a single PLIM image. Therefore, BTPDM1 and BTP-3OH were found to have sufficient photostability for obtaining clear PLIM images.
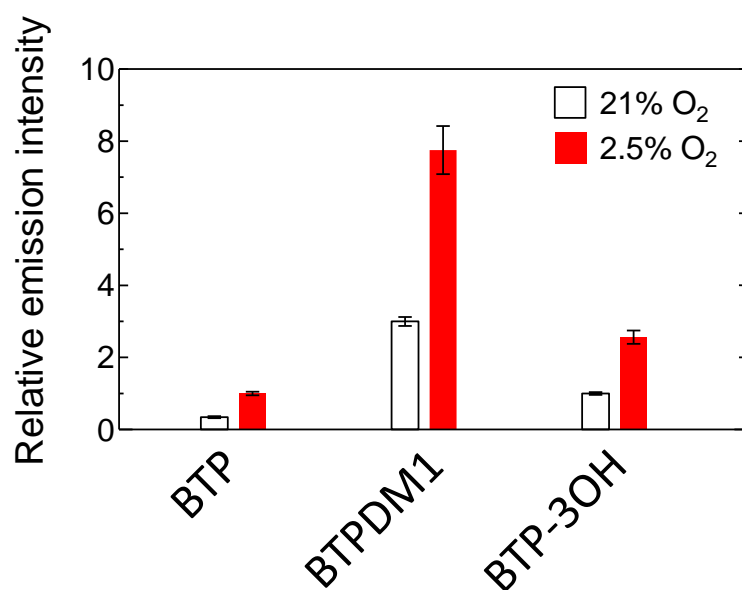
Fig. 3-6 Relative emission intensities of each probe taken up into HT-29 cells incubated with BTP, BTPDM1 or BTP-3OH (5 μM, 2 h) at 37 °C. The emission intensities measured with a microplate reader (Infinite 200 PRO, Tecan) were corrected for the number of HT-29 cells in each well and the molar extinction coefficient at 488 nm in MeCN (4700, 5400, and 2800 $M^{-1}cm^{-1}$ for BTP, BTPDM1 and BTP-3OH, respectively). Excited at 488 nm. Monitored at 615 nm (BTP), 616 nm (BTPDM1) and 601 nm (BTP-3OH). $N = 3$. Error bar: S.D.
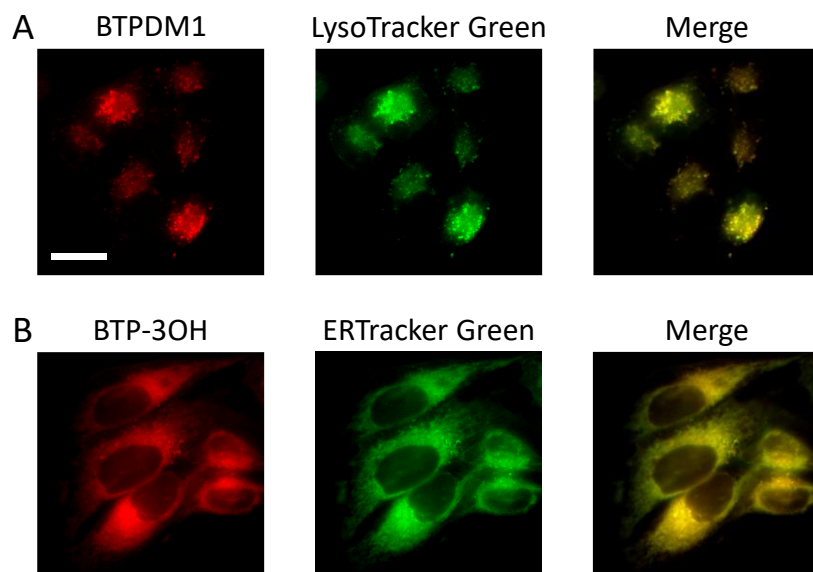
Fig. 3-7 Subcellular localization of BTPDM1 (**A**) and BTP-3OH (**B**) in HeLa cells. The emission images of HeLa cells stained with BTPDM1 (**A**, left), BTP-3OH (**B**, left), organelle-selective markers (middle) and their overlay images (right). Cells were costained with BTPDM1 (500 nM, 2 h) and LysoTracker Green (200 nM, 20 min), and BTP-3OH (1 μM, 2 h) and ERTracker Green (200 nM, 20 min). λ_{ex}: 400-440 nm, λ_{em}: >590 nm (left). λ_{ex}: 450-500 nm, λ_{em}: 515-565 nm (middle). Scale bar: 20 μm.
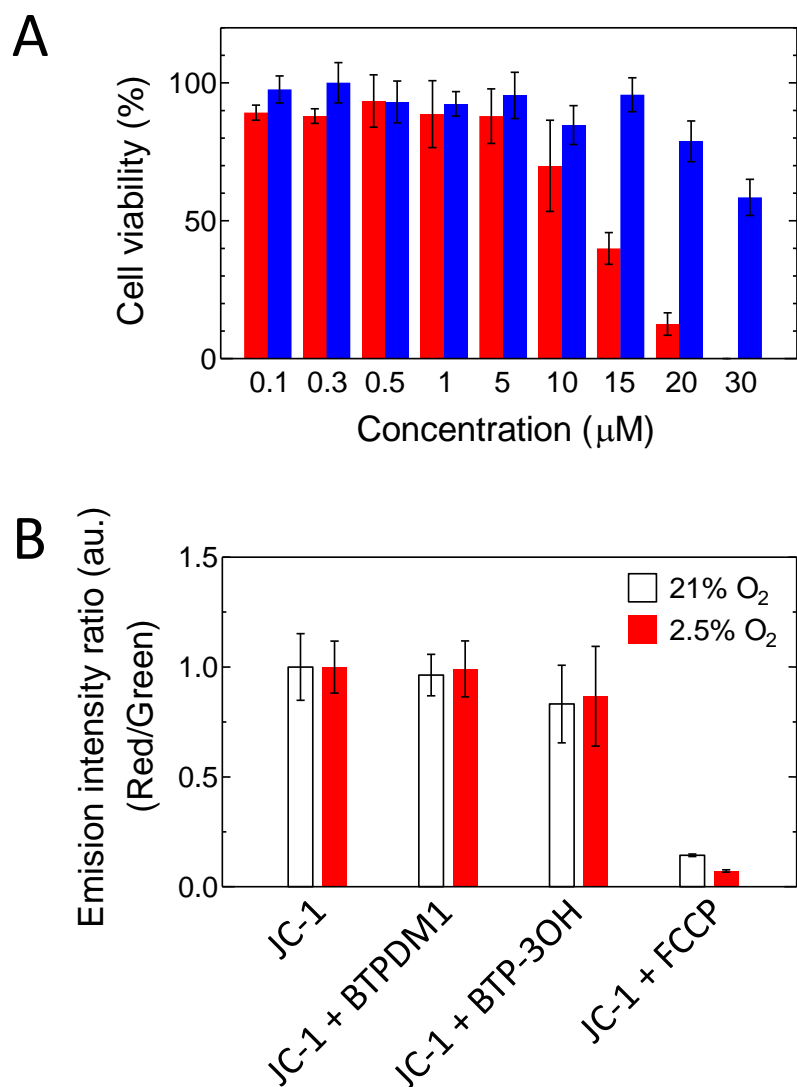
Fig. 3-8 Assessment of the cytotoxicity of BTPDM1 and BTP-3OH. (**A**) Cell viability of HT-29 cells when incubated with various concentrations of BTPDM1 (red) and BTP-3OH (blue) for 24 h, evaluated by the WST assay. Error bar: S.D. (**B**) Emission intensity ratio (Red/Green) of JC-1 in HT-29 cells stained with BTPDM1, BTP-3OH (1 μM, 2 h) and FCCP (10 μM, 1 h). λ_{ex}: 488 nm, λ_{em}: 595 nm (Red emission). λ_{ex}: 488 nm, λ_{em}: 540 nm (Green emission). $N = 12$. Error bar: S.D.
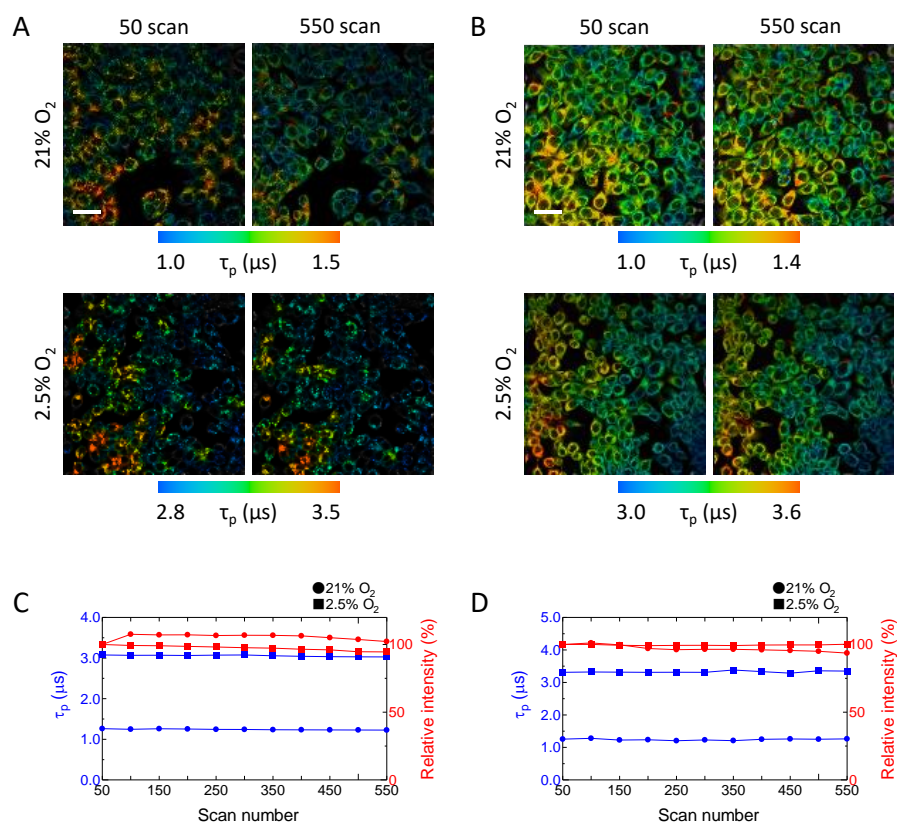
Fig. 3-9 Photostability of BTPDM1 and BTP-3OH in 2D cultured HT-29 cells. (**A, B**) PLIM images of monolayered HT-29 cells stained with BTPDM1 (**A**) and BTP-3OH (**B**) acquired after 50 and 550 scans at 488 nm irradiation under 21% and 2.5% O_2. (**C, D**) Variation of average phosphorescence lifetime (blue) and intensity (red) derived from the PLIM images of HT-29 cells stained with BTPDM1 (**C**) and BTP-3OH (**D**). Each image was acquired every 50 scans up to 550 scans. Probe concentration: 1 μM, incubation time: 2 h. λ_{ex}: 488 nm, λ_{em}: >590 nm. Scale bar: 50 μm.

3-2-5　Quantification of O$_2$ Levels for Cell Spheroids

To quantify the oxygen levels in tissues based on lifetime measurements, it needs a calibration curve that represents the relationship between lifetime and pO$_2$. Since BTPDM1 and BTP-3OH are likely to accumulate in specific organelle membranes, the pO$_2$ dependence of the phosphorescence lifetime in cells is expected to be different from that in solution. Therefore, the lifetime was calibrated by measuring PLIM images of HT-29 cells incubated with BTPDM1 or BTP-3OH under 21, 15, 10, 5 and 0% O$_2$ conditions at 37°C (Fig. 3-10A and 3-10B). Here 10 μM antimycin A (AntA) was added to the medium prior to the PLIM measurements to suppress the oxygen consumption by cellular respiration, and in the experiments under N$_2$ saturated conditions Na$_2$SO$_3$ (final concentration: 500 mM) was added into the medium to remove oxygen remaining in the culture. The average lifetime of an entire image was plotted against the pO$_2$ according to the Stern-Volmer equation (Eq. 1-1). A linear relationship was obtained for both complexes (Fig. 3-10C), and the k_q values for BTPDM1 and BTP-3OH in HT-29 cells were derived to be 4.22×10^3 mmHg^{-1}s^{-1} and 5.36×10^3 mmHg^{-1}s^{-1} along with the τ_p^0, 5.20 μs and 6.18 μs, respectively. These values were used to quantify oxygen levels in cell spheroids in the next section.

One key issue in applying small-molecule intracellular oxygen probes for *in vivo* O$_2$ measurements is the method of lifetime calibration. In this study the tissue pO$_2$ were quantified based on the k_q and τ_p^0 determined using a cell line that is the same as or close to the cell type in the target organ in which the probe is accumulated. The O$_2$ quenching rate constants in HT-29 cells ((4.0-5.0) $\times 10^3$ mmHg^{-1}s^{-1}) were reduced by an order of magnitude compared with those in solution ((7.5-8.5) $\times 10^3$ mmHg^{-1}s^{-1}) (Table 3-2). Since lipophilic BTPDM1 and BTP-3OH are likely to accumulate in organelle membranes after they pass through the plasma membranes of living cells,

the much smaller k_q values in cells can be attributed, at least in part, to the decrease in the diffusion rates of O_2 and Ir(III) complexes in organelle membranes. Further reductions in k_q values can be caused by the binding of excited probe molecules to proteins in the organelle membrane in which they are incorporated. The τ_p^0 values of BTPDM1 and BTP-3OH in cells were decreased by 10-15% compared with those in MeCN. One possible reason lies in the concentration quenching within organelle membranes. The τ_p^0 of BTPDM1 partitioned into DMPC liposomes tended to shorten with increasing probe concentration in solution (Table 3-3), suggesting that concentration quenching may have occurred. Cross-sensitivity to endogenous species other than O_2 cannot be ruled out, but its contribution appears to be relatively small because the τ_p^0 values of BTPDM1 and BTP-3OH in cells are close to those in MeCN. As one of endogenous biological substances that may interact with these complexes, phosphorescence quenching by glutathione was examined for BTPDM1 and BTP-3OH partitioned into DMPC liposome. Quenching was not seen even in the presence of 1 mM glutathione (Table 3-4). It was also confirmed that phosphorescence lifetime is almost independent of pH under physiological conditions (Table 3-5).
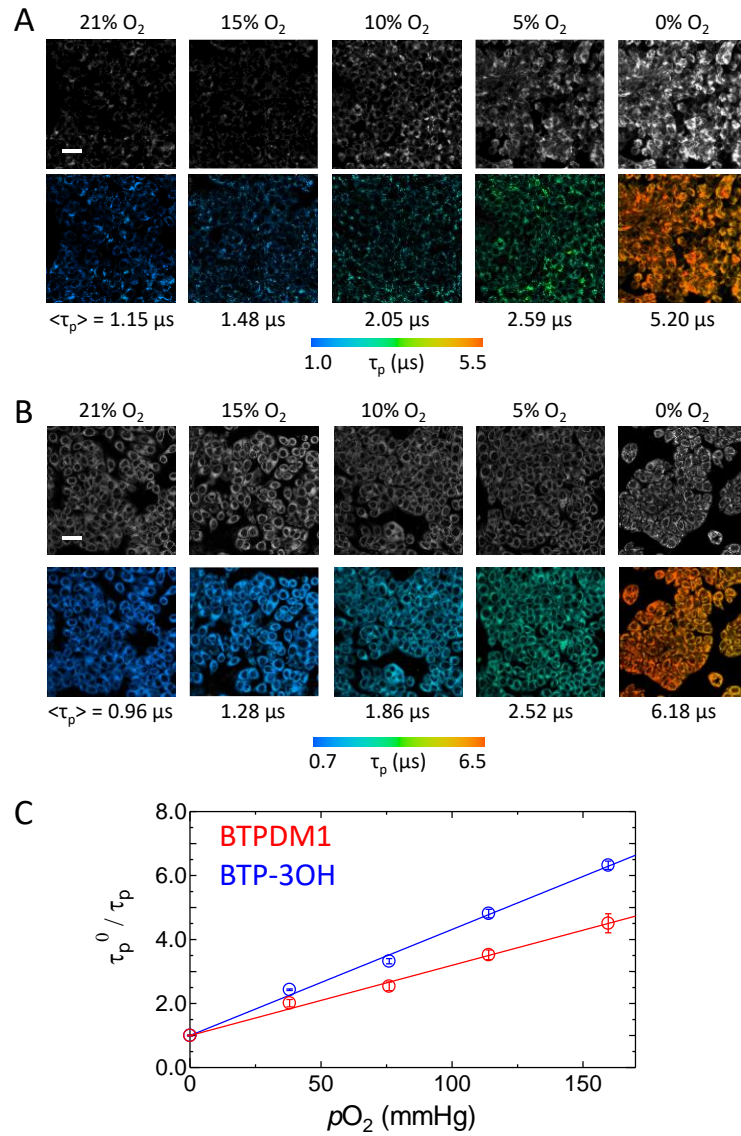
Fig. 3-10 Intensity (upper) and PLIM (lower) images of HT-29 cells stained with BTPDM1 (**A**) and BTP-3OH (**B**) under different pO_2 in an incubator. The average phosphorescence lifetimes are shown below each image. Cells were treated with AntA (5-21% O_2) and Na_2SO_3 (0% O_2). λ_{ex}: 488 nm, λ_{em}: >590 nm. Scale bar: 50 μm. (**C**) Stern-Volmer plots of τ_p^0/τ_p as a function of pO_2 for BTPDM1 (red) and BTP-3OH (blue) partitioned into HT-29 cells under different pO_2 in an incubator. Error bars: S.D.

Table 3-3 Phosphorescence lifetimes of BTPDM1 probe partitioned into DMPC liposome under different BTPDM1 concentrations in Tris-HCl buffer.

Probe concentration (μM)	τ_p (μs)	
	aerated	N$_2$ saturated
0.5	0.549	5.28
1	0.529	5.23
2	0.494	5.11
5	0.512	5.07
10	0.508	5.06
20	0.521	4.72
50	0.544	4.53

Table 3-4 Phosphorescence lifetime of BTPDM1 and BTP-3OH partitioned into DMPC liposome with (1.0 mM) and without glutathione (GSH) in Tris-HCl buffer at 37°C.

GSH (mM)	BTPDM1		BTP-3OH	
	τ_p (ns)	τ_p^0 (μs)	τ_p (ns)	τ_p^0 (μs)
0.0	487	4.96	468	5.46
1.0	497	5.12	471	5.52

τ_p and τ_p^0 denote the phosphorescence lifetime taken in aerated and N$_2$ saturated solutions, respectively.

Table 3-5 Phosphorescence lifetime of BTPDM1 and BTP-3OH partitioned into DMPC liposome under different pH in Tris-HCl buffer or HEPES buffer at 37°C.

pH	BTPDM1		BTP-3OH	
	τ_p (ns)	τ_p^0 (µs)	τ_p (ns)	τ_p^0 (µs)
5.1	543	4.94	466	5.21
6.0	499	4.99	463	5.35
6.7	509	5.09	467	5.35
7.4	495	4.94	477	5.40
8.0	473	5.03	474	5.40

τ_p and τ_p^0 denote the phosphorescence lifetime taken in aerated and N_2 saturated solutions, respectively.

3-2-6 Imaging of O_2 Distribution in Cell Spheroids with BTPDM1 and BTP-3OH

In the past decade, three-dimensional (3D) spheroid systems have received much attention in fields such as drug discovery, cancer research, and toxicology. They provide a more physiologically-relevant environment and organ-like microarchitecture compared with conventional 2D cell cultures and better mimic the crucial tumor tissue properties and microenvironment. The excellent cell-permeable properties of BTPDM1 and BTP-3OH suggested their potential for in-depth staining of 3D cell spheroids and thus the potential of these probes for visualization of the O_2 distribution within spheroids and living tissues.

So, in this section the PLIM images of HT-29 cell spheroid that were incubated with BTPDM1 or BTP-3OH were acquired by using the apparatus shown in Fig. 2-2. Here, each probe (final concentration: 500 nM) was added to the medium after the spheroids were formed, and the spheroids were further incubated with the probe for 24 h prior to PLIM measurements. The bright-field images taken on different planes in the z direction (Fig. 3-11) show that spheroids with a diameter of 150-200 μm were almost uniformly stained, including the core, by BTPDM1 and BTP-3OH. The Z-stack phosphorescence lifetime images of an HT-29 spheroid stained with BTPDM1 (Fig. 3-11B) and BTP-3OH (Fig. 3-11C) indicate that the cells closer to the center of the spheroid gave longer lifetimes, i.e. lower O_2 levels compared with those in the peripheral region. For quantitative evaluation of the O_2 gradient in a spheroid, the line profiles of the average phosphorescence lifetime were investigated on the plane approximately 20 μm from the bottom (Fig. 3-11D).

Further, the lifetimes along the central area in the z-direction (Fig. 3-11E) were measured to derive the pO_2 distribution (Fig. 3-11D and 3-11E) based on the τ_p^0 and

k_q obtained for HT-29 cultured cells. Both probes showed that the pO_2 is reduced near the center and bottom surface of the spheroids, because the oxygen supply from the bottom direction is cut off by the bottom glass, and also the peripheral cells consume oxygen carried by diffusion from the culture medium. The degree of hypoxia in the core depended on the spheroid size (Fig. 3-12) and the respiratory activity as will be described below.

Next, it was investigated whether BTPDM1 and BTP-3OH can image changes in the oxygen status of spheroids caused by metabolic stimulus. FCCP (carbonyl cyanide p-(trifluoromethoxy)phenylhydrazone) and AntA were used to alter the oxygen status of HT-29 spheroids by stimulating metabolic processes; FCCP is an uncoupler of oxidative phosphorylation in mitochondria that disrupts ATP synthesis by transporting protons across the membrane and thus increases the O_2 consumption rate. AntA is known to inhibit the mitochondrial electron transport chain from cytochrome b to cytochrome $c1$ and suppress O_2 consumption. Metabolic stimulation of HT-29 cell spheroids by FCCP and AntA significantly changed the PLIM images (Fig. 3-13). The lifetime images of the spheroid plane ~30 μm from the bottom (Fig. 3-13B and 3-13C) demonstrated that upon addition of FCCP to the medium, the lifetimes of both probes quickly increased within ~10 min, especially in the core. The oxygen partial pressures calculated from the lifetimes based on the calibration in Fig. 3-10 indicate that the pO_2 decreased sharply to less than 20 mmHg by increased O_2 consumption, and then it slowly recovered. Conversely, the lifetimes of both probes rapidly dropped within 10 min upon metabolic stimulation using AntA (Fig. 3-13D and 3-13E), corresponding to the increase in pO_2 by suppression of O_2 consumption. The pO_2 changes of spheroids reflected the metabolic effects of FCCP and AntA, demonstrating that BTPDM1 and BTP-3OH can be used to track the oxygen status of cell spheroids. It is confirmed from

these results that BTPDM1 and BTP-3OH have high penetrating ability into spheroids and their feasibility as tissue O_2 probes.

As described above, one of the advantages of BTPDM1 and BTP-3OH as intracellular O_2 probe is their extremely high cellular uptake efficiencies. The O_2 imaging experiments using HT-29 cell spheroids (Fig. 3-11) demonstrated that BTPDM1 and BTP-3OH are efficiently internalized into the spheroids with a diameter of ~200 μm. The penetrative abilities of some molecular O_2 probes into cell spheroids reported so far are compared in Table 3-6. These probes include glucose conjugates of Pt(II)-*meso*-tetrakis-(pentafluorophenyl)porphyrin [6], Pt(II)-5, 10, 15, 20-tetrakis-(4-carboxyphenyl)porphyrin [7], a Pt(II) complex bearing a cyclometalating 3-di(2-pyridyl)benzene-based moiety [8], and click-assembled oxygen-sensing nanoconjugates with Pd(II) tetracarboxytetrabenzoporphyrin as a phosphorescent core [9]. Comparing each probe for its concentration in culture medium and the incubation time required for observation of clear luminescence images, it can be seen that BTPDM1 and BTP-3OH have excellent cell permeability. Furthermore, PLIM measurements with these probes made it possible to track oxygen levels and distributions in spheroids. As described in the next chapter, these properties are very useful for investigating the oxygen status in living tissues.
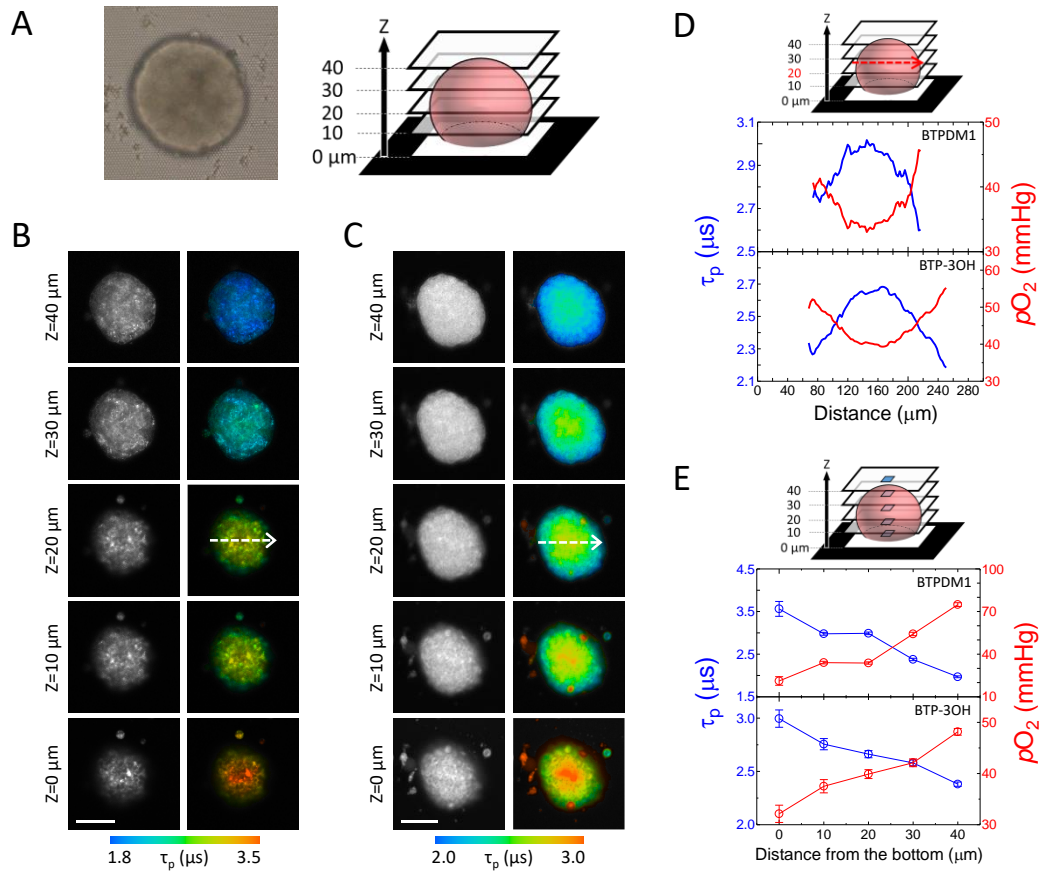
Fig. 3-11 (**A**) Bright-field image (left) and schematic view (right) of an HT-29 cell spheroid. (**B, C**) Z-stacked phosphorescence intensity (left) and lifetime (right) images of an HT-29 cell spheroid stained with BTPDM1 (**B**) and BTP-3OH (**C**). Each image corresponds to cross-section from the bottom to the upper part at an interval of 10 μm along the z-axis. λ_{ex}: 488 nm, λ_{em}: >590 nm. Scale bar: 100 μm. (**D**) Line profiles of phosphorescence lifetime (blue) and pO$_2$ (red) along the arrows shown in **B** and **C**. (**E**) Average phosphorescence lifetime (blue) and pO$_2$ (red) of the square region along the z-axis in an HT-29 cell spheroid stained with probes.
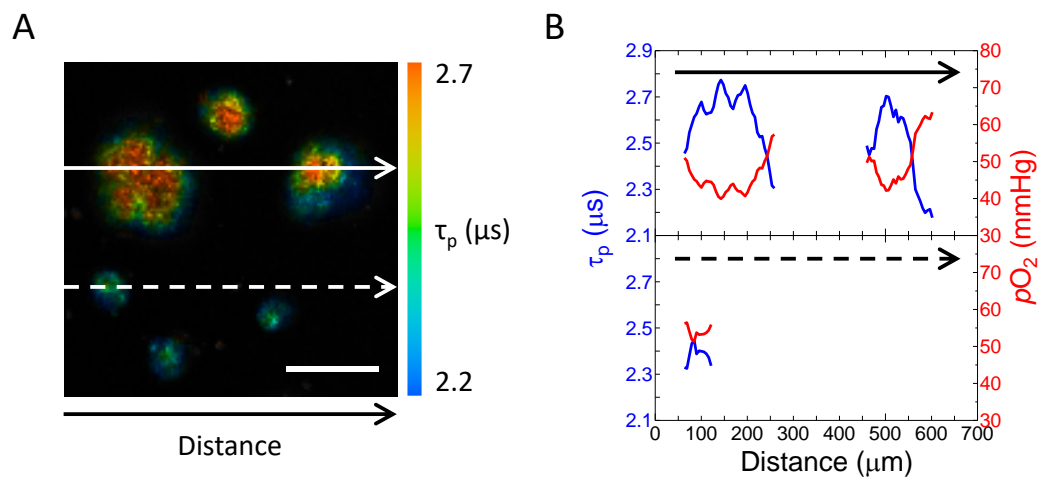
Fig. 3-12 (A) PLIM images of HT-29 cell spheroids with different sizes stained with BTPDM1. The emission image was taken at z = 0 μm. λ_{ex}: 488 nm, λ_{em}: >590 nm. Scale bar: 100 μm. **(B)** Line profile of phosphorescence lifetime and pO$_2$ in the HT-29 cell spheroids along the solid arrow (top) and dashed arrow (bottom) in **A**.
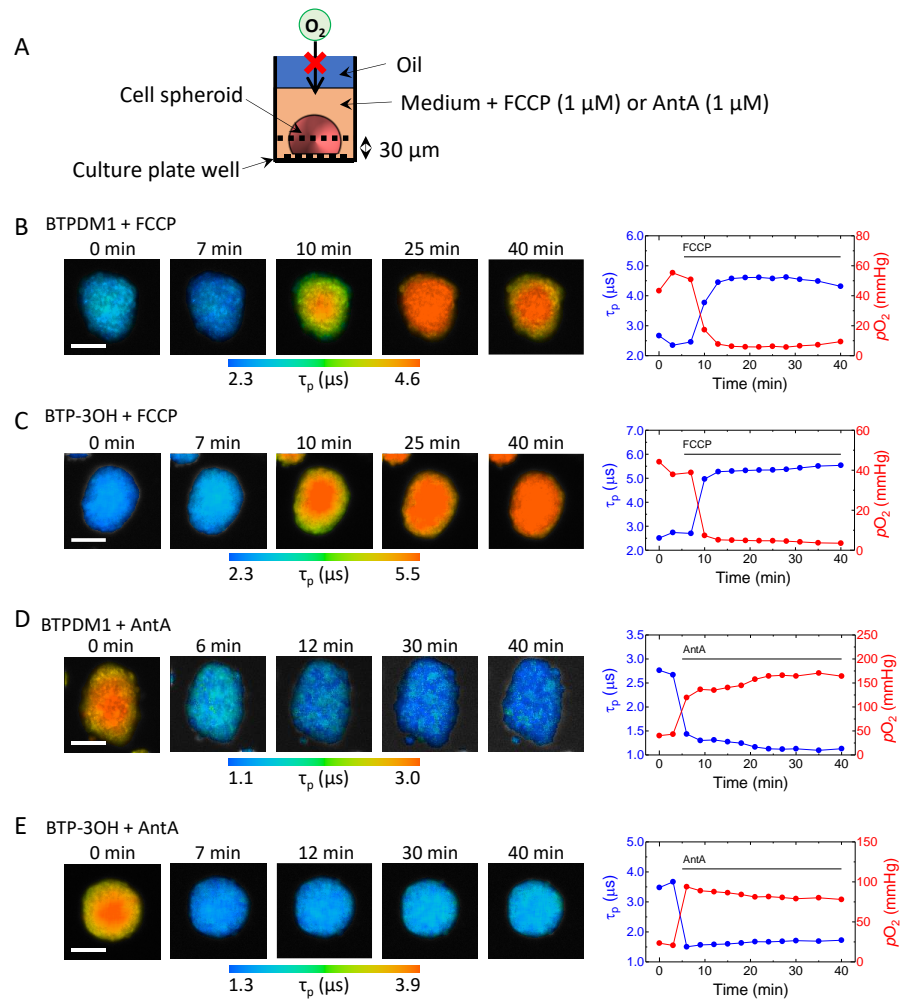
Fig. 3-13 Imaging of the oxygen status of an HT-29 cell spheroid upon metabolic stimulation with FCCP or AntA. (**A**) Schematic representation of a spheroid in media containing FCCP or AntA. PLIM images were taken at 30 μm from the bottom after oil sealing. (**B**, **C**) Variation in PLIM images (left), and their average phosphorescence lifetime and pO_2 (right) of an HT-29 cell spheroid stained with BTPDM1 (**B**) and BTP-3OH (**C**) by metabolic stimulation with FCCP (1 μM) at 5 min and 6 min, respectively, and BTPDM1 (**D**) and BTP-3OH (**E**) by metabolic stimulation with AntA (1 μM) at 5 min. λ_{ex}: 488 nm, λ_{em}: >590 nm. Scale bar: 100 μm.

Table 3-6 Representative molecular probes that have been used for O_2 imaging of cell spheroids.

Spheroid [a]	Probe [b]	[Probe] [c] (μM)	Incubation time (h)	Ref.
HT-29	BTPDM1, BTP-3OH	0.5	24	This work
PC-12	Pt-Glc	2.5	16	6
Colon26	PtTCPP	10	24	7
C8161 [d]	PtL^{S}C1	100	12	8
OvCa [e]	G3 CAOS	2.0	4	9

[a]HT-29 (human colorectal adenocarcinoma cell), PC-12 (rat pheochromocytoma cell), Colon26 (mouse colon carcinoma cell), C8161 (human melanoma cell). OvCa (ovarian cancer cell). [b]Pt-Glc: glucose conjugate of Pt(II)-*meso*-tetrakis-(pentafluorophenyl)porphyrin (PtPFPP), PtTCPP: Pt(II)-5, 10, 15, 20-tetrakis-(4-carboxyphenyl)porphyrin, PtL^{S}Cl: where L is a cyclometalating 3-di(2-pyridyl)benzene based ligand, G3 CAOS: click-assembled oxygen-sensing nanoconjugate with Pd(II) tetracarboxytetrabenzoporphyrin (PdTCTBP) as phosphorescent core. [c]probe concentration in the medium. [d]Spheroid size is larger than the other spheroids in this table. [e]Spheroid images are taken by using a single-photon-counting confocal microscope.

3-3 Conclusions

A PLIM system optimized for the O_2 imaging of living cells and tissues was constructed by combining an inverted microscope and a confocal laser scanning system equipped with a lifetime measurement unit. The reliability of the lifetime obtained by PLIM measurement was confirmed by comparing the lifetime of the same solution (BTP-PEG$_{48}$ in PBS) measured by our PLIM system and the TCSPC instrument. Furthermore, the accuracy of the lifetime distribution of the PLIM image was assessed using a BTP-PEG$_{48}$ in McCoy's 5A medium under 21% and O% conditions. The fluctuation in lifetime within a single PLIM image was within 10% both under 21% and 0% conditions. It was also found that even if the peak photon count is as low as 100, effective use of spatial binning can reduce the variation in the lifetime image.

Small-molecule O_2 probes, BTPDM1 and BTP-3OH, exhibited photophysical properties including emission brightness and O_2 sensitivity suitable for an optical O_2 probe in solution. These Ir(III) complexes were efficiently taken up into cells when added to the culture media of monolayer cells and showed preferential accumulation to lysosomes and endoplasmic reticulum (ER), respectively. It was confirmed that under the measurement conditions of PLIM images of cells and tissues, the cytotoxicity of these complexes was sufficiently low and the photostability was sufficiently high.

The cell-permeable properties of BTPDM1 and BTP-3OH enabled internalization into cell spheroids with a diameter of ~200 μm. PLIM images of spheroids stained with BTPDM1 or BTP-3OH showed that the core of the spheroids became hypoxic, generating an O_2 concentration gradient. It was also demonstrated that PLIM images can track changes in oxygenation status within spheroids due to metabolic stimulation.

Appendix 3-1　Synthesis and Characterization of BTP-3OH

Synthesis of BTP-3OH
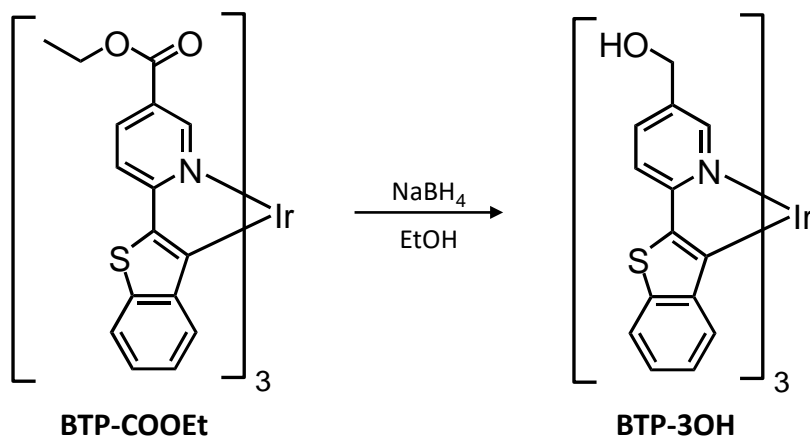
Scheme A3-1 Synthesis of BTP-3OH.

To a solution of BTP-COOEt (100 mg, 0.10 mmol) in ethanol (20 mL) was added NaBH$_4$ (200 mg, 5.3 mmol) quickly and then refluxed for 5 h. After cooling the solution was added to chloroform, then washed with distilled water. The organic layer was dried over sodium sulphate and evaporated to dryness under reduced pressure. Purification of crude product was performed by using a recycling preparative HPLC (LC-9225 NEXT, Japan Analytical Industry). The final product (BTP-3OH) was obtained as yellow powder (34 mg, 37 μmol, 39%). ^{1}H NMR (400 MHz, DMSO-d_6): δ 7.83.7.78 (m, 4H), 7.73-7.71 (m, 2H), 7.69-7.56 (m, 6H), 7.13-7.05 (m, 2H), 7.03-6.99 (m, 1H), 6.78-6.74 (m, 2H), 6.58 (t, J = 8.1 Hz, 1H), 6.35 (d, J = 7.8 Hz, 1H), 6.01 (dd, J = 16.9, 8.0 Hz, 2H), 5.19-5.10 (m, 3H), 4.26-4.22 (m, 2H), 4.20-4.10 (m, 4H). ESI-MS (positive): calcd. for C$_{42}$H$_{30}$IrN$_3$O$_3$S$_3$ [M]$^+$: 913.13, found: 913.2.

References

[1]   Yoshihara, T., Hirakawa, Y., Nangaku, M. & Tobita, S. Hydrophilic Ir(III) Complexes for In vitro and In vivo Oxygen Imaging, RSC Detection Science: Quenched-phosphorescence Detection of Molecular Oxygen: Applications in Life Sciences, ed. Papkovsky, D. B. & Dmitriev, R. I. Royal Society of Chemistry, 2018, Chap. 4, pp.71-90.

[2]   Montalti, M., Credi, A., Prodi, L. & Gandolfi, M. T. *Handbook of Photochemistry* THIRD EDITION. CRC-Taylor & Francis, Boca Raton, 2006.

[3]   Hasebe, N., Deguchi, Y., Murayama, S., Yoshihara, T., Horiuchi, H., Okutsu, T., & Tobita, S. Phosphorescence quenching of neutral and cationic iridium(III) complexes by molecular oxygen and aromatic electron acceptors. *J. Photochem. Photobiol. A: Chem.* **324**, 134–144 (2016).

[4]   Yoshihara, T., Hirakawa, Y., Hosaka, M., Nangaku, M. & Tobita, S. Oxygen imaging of living cells and tissues using luminescent molecular probes. *J. Photochem. Photobiol. C Photochem. Rev.* **30**, 71–95 (2017).

[5]   Zhang, S., Hosaka, M., Yoshihara, T., Negishi, K., Iida, Y., Tobita, S., & Takeuchi, T. Phosphorescent light-emitting iridium complexes serve as a hypoxia-sensing probe for tumor imaging in living animals. *Cancer Res.* **70**, 4490–4498 (2010).

[6]   Dmitriev, R. I., Kondrashina, A. V., Koren, K., Klimant, I., Zhdanov, A. V., Pakan, J. M. P., McDermott, K. W., & Papkovsky, D. B. Small molecule phosphorescent probes for O_2 imaging in 3D tissue models. *Biomater. Sci.* **2**, 853-866 (2014).

[7]   Kurokawa, H., Ito, H., Inoue, M., Tabata, K., Sato, Y., Yamagata, K., Kizaka-Kondoh, S., Kadonosono, T., Yano, S., Inoue, M., & Kamachi, T. High

resolution imaging of intracellular oxygen concentration by phosphorescence lifetime. *Sci. Rep.* **5**, 10657 (2015).

[8]   Raza, A., Colley, H. E., Baggaley, E., Sazanovich, I. V., Green, N. H., Weinstein, J. A., Botchway, S. W., MacNeil, S., & Haycock, J. W. Oxygen mapping of melanoma spheroids using small molecule platinum probe and phosphorescence lifetime imaging microscopy. *Sci. Rep.* **7**, 10743 (2017).

[9]   Nichols, A. J., Roussakis, E., Klein, O. J. & Evans, C. L. Click-assembled, oxygen-sensing nanoconjugates for depth-resolved, near-infrared imaging in a 3D cancer model. *Angew. Chem. Int. Ed.* **53**, 3671–3674 (2014).

Chapter 4

In Vivo O$_2$ Imaging

in Hepatic Tissues

4-1　Introduction

Since it was confirmed in Chapter 3 that BTPDM1 and BTP-3OH can be efficiently taken up into spheroids and evaluate the oxygen status, in Chapter 4 *in vivo* PLIM measurements of hepatic tissues were performed using BTPDM1 and BTP-3OH as O_2 probes.

The hepatic lobule is a fundamental structural unit of the liver with a hexagonal shape (Fig. 4-1) [1,2]. In the lobule, blood runs unidirectionally from the vertices of the hexagon called portal triads, through microcirculatory networks known as sinusoids, to a central vein (CV) in the middle of the lobule. The portal triad contains two distinct inlets for blood flow: a well-oxygenated hepatic artery and a poorly-oxygenated portal vein, the latter of which constitutes ~70% of total liver blood flow. Therefore, even under physiological conditions, liver parenchymal cells and hepatocytes surrounding the portal triad are exposed to relatively low oxygen concentrations, and pericentral hepatocytes experience much lower oxygen concentrations, forming a zonal heterogenous distribution of oxygen along the sinusoids in the hepatic lobule. These intralobular oxygen distributions, however, are considered to be prerequisite for normal liver metabolic functions in a zone-specific manner; mitochondria-related metabolisms such as gluconeogenesis, fatty acid oxidation, and urea synthesis are more active in periportal hepatocytes, while lesser oxygen-required metabolisms including glycolysis, fatty acid synthesis, and glutamine synthesis occur predominately in pericentral ones. In addition, this metabolic zonation is often disrupted in disease conditions with aberrant oxygen distribution in the hepatic lobules. To deepen our knowledge about the dynamic alterations in liver metabolism in both physiological and pathophysiological conditions, real-time imaging of intracellular oxygen tension *in situ* is a promising method with the development of
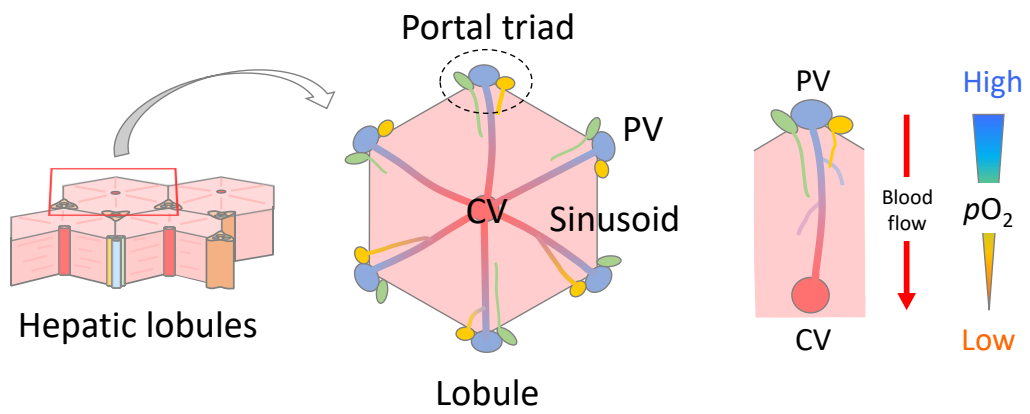
oxygen-sensitive probes.

Fig. 4-1 Schematic views of hepatic lobules. CV: central vein, PV: portal vein.

4-2 Results and Discussion

4-2-1 Synthesis and Characterization of (btp)₂Ir(acac-2OH)

The complex (btp)₂Ir(acac-2OH) was synthesized from BTPSA which was prepared according to the literature [3] as shown in Scheme 4-1. The target product was characterized by ^{1}H NMR and mass spectrometry. Details of the synthetic procedure and analytical data are given in Appendix 4-1.
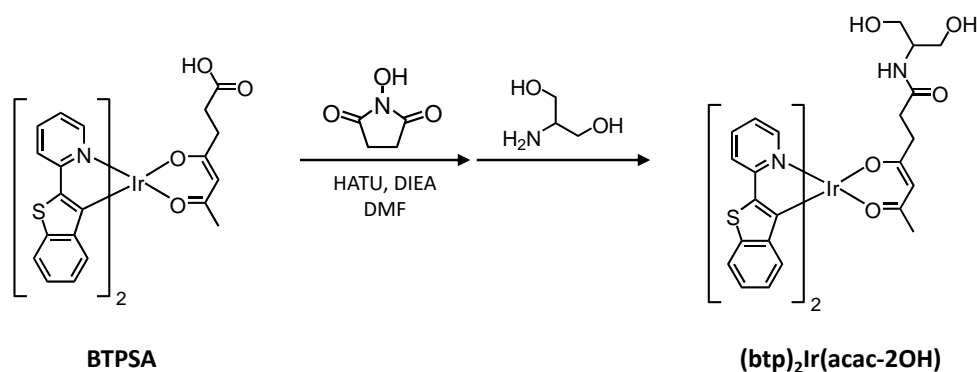
Scheme 4-1 Synthesis of (btp)₂Ir(acac-2OH).

4-2-2 Quantification of O₂ Levels in Hepatic Tissues

To quantify the oxygen levels in hepatic tissues based on lifetime measurements, it needs a calibration curve that represents the relationship between lifetime and pO₂. Since BTPDM1 and BTP-3OH are likely to accumulate in specific organelle membranes, the pO₂ dependence of the phosphorescence lifetime in cells is expected to be different from that in solution. Therefore, the lifetime was calibrated by measuring PLIM images of Alpha mouse liver 12 (AML 12) cells incubated with BTPDM1 or BTP-3OH under 21, 15, 10, 5 and 0% O₂ conditions at 37°C (Fig. 4-2A and 4-2B). Here 10 μM antimycin A (AntA) was added to the medium prior to the

PLIM measurements to suppress the oxygen consumption by cellular respiration, and in the experiments under N_2 saturated conditions Na_2SO_3 (final concentration: 500 mM) was added into the medium to remove oxygen remaining in the culture. The average lifetime of an entire image was plotted against the pO_2 according to the Stern-Volmer equation (Eq. 1-1). A linear relationship was obtained for both complexes (Fig. 4-2C), and the k_q values for BTPDM1 and BTP-3OH in AML 12 cells were derived to be 5.16×10^3 mmHg^{-1}s^{-1} and 4.91×10^3 mmHg^{-1}s^{-1} along with the τ_p^0, 4.93 μs and 6.23 μs, respectively. These values were used to quantify oxygen levels in hepatic tissues in the next section.
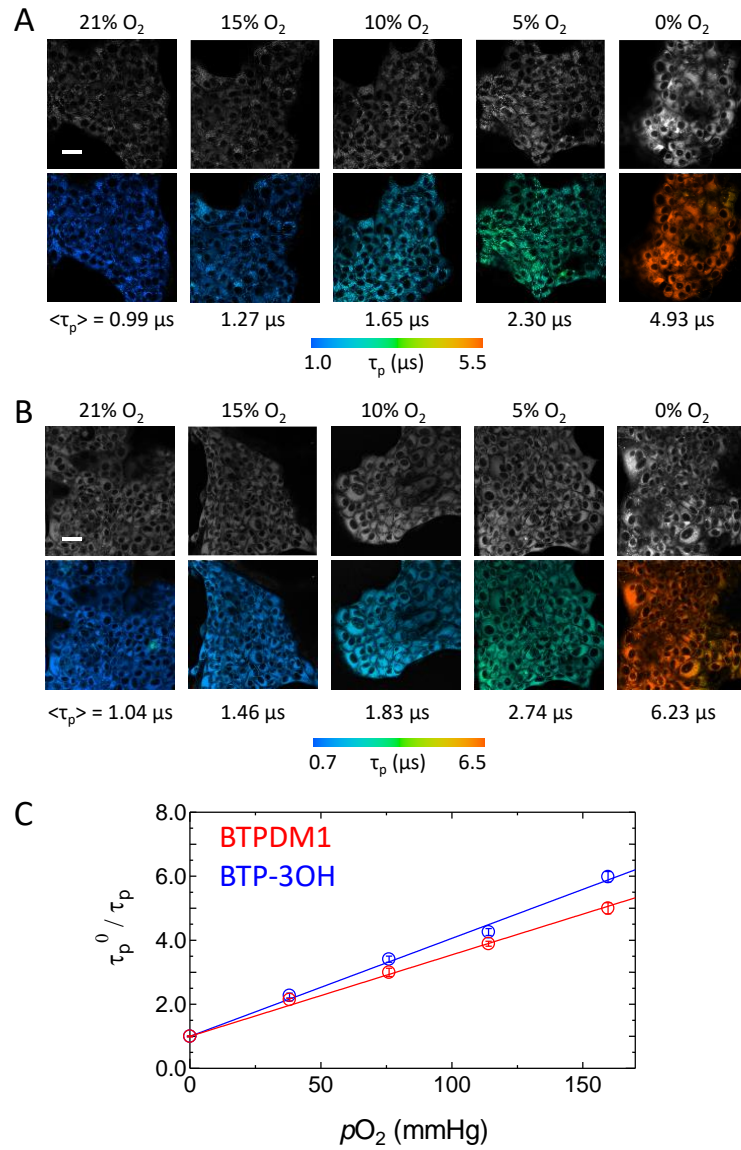
Fig. 4-2 Intensity (upper) and PLIM (lower) images of AML 12 cells stained with BTPDM1 (**A**) and BTP-3OH (**B**) under different pO_2 in an incubator. The average phosphorescence lifetimes are shown below each image. Cells were treated with AntA (5-21% O_2) and Na_2SO_3 (0% O_2). λ_{ex}: 488 nm, λ_{em}: >590 nm. Scale bar: 50 μm. (**C**) Stern-Volmer plots of τ_p^0/τ_p as a function of pO_2 for BTPDM1 (red) and BTP-3OH (blue) partitioned into AML 12 cells under different pO_2 in an incubator. Error bars: S.D.

4-2-3 *In Vivo* O$_2$ Imaging in Hepatic Tissues Using BTPDM1 and BTP-3OH

The probe compound, BTPDM1 or BTP-3OH (250 nmol in 25 μL dimethyl sulfoxide, diluted using PBS to 175 μL) was administered intravenously to anesthetized mice. Approximately 10 min after probe administration, the abdomen was opened by median incision to expose the liver, and the phosphorescence lifetime images of hepatic tissues (~10 μm deep from the surface of the liver) were measured around the central vein (CV) using different magnifications. As shown in Fig. 4-3, both probes gave clear PLIM images of hepatic tissues with cellular-level resolution. Here, the areas that appear black are the regions where the emission intensity from the probe is extremely low, and these mainly correspond to the nucleus and sinusoid that have low probe uptake. It can be seen from the PLIM images measured with a 40× objective lens that BTPDM1 and BTP-3OH are internalized into hepatocytes that line up along sinusoids. The arrangement of hepatocytes and lifetime distribution indicate that these images correspond to a hexagonal hepatic lobule (Fig. 4-1) and that CV exists in the area with the longest lifetime (displayed in orange). The region surrounding the CV is considered to be the portal vein (PV) because it has a much shorter lifetime, i.e. much higher oxygen level. PLIM images obtained with BTPDM1 and BTP-3OH show a similar lifetime gradient that increases from the PV to CV.

To quantify the O$_2$ levels in specific locations in the lobules from the phosphorescence lifetimes, calibration of the phosphorescence lifetimes was performed by using an AML 12 cells as shown in Fig. 4-2. Using the τ_p^0 and k_q of BTPDM1 and BTP-3OH as determined in a monolayer of AML 12 cells, the average pO$_2$ of the regions of interest (ROIs) was evaluated in the CV, PV, and the intermediate region between CV and PV (IR); the phosphorescence lifetime of BTPDM1 gave

reasonable O_2 levels (24 ± 6.1 mmHg for CV, 32 ± 4.9 mmHg for IR, and 39 ± 4.2 mmHg for PV), whereas IBTP-3OH exhibited much lower O_2 levels (3 ± 1.8 mmHg for CV, 5 ± 1.8 mmHg for IR, and 7 ± 2.7 mmHg for PV) (Table 4-1). PLIM images obtained with BTPDM1 and BTP-3OH clearly visualized the oxygen gradient from PV to CV. However, the O_2 levels estimated from the phosphorescence lifetimes differed between BTPDM1 and BTP-3OH.

To confirm that BTPDM1 and BTP-3OH retain their spectral properties in hepatic tissues after systemic administration, the emission spectra of the liver were measured using living mice. Each probe molecule (250 nmol) was administered through the tail vein, and the emission images and spectra of livers were taken using a fluorescence microscope with an excitation filter of 450-500 nm and emission filter of >532 nm (Fig. 4-4). The observed emission spectra with maxima at 619 nm for BTPDM1 and 607 nm for BTP-3OH were slightly red-shifted compared with those in MeCN, but they were in good agreement with those in AML 12 cells, demonstrating that these probes maintain their spectral properties in hepatic tissue.

The reason why BTP-3OH gave an abnormally low O_2 level may be related to the function of the liver to metabolize xenobiotics. So, the detoxification of ammonia in the liver was investigated to clarify how clearance of harmful metabolic byproducts and detoxification of xenobiotics affect hepatic O_2 levels. Here the liver is known to have the function of converting toxic ammonia to urea by the urea cycle or to glutamine by glutamine synthesis in hepatocytes. With increased metabolic activity of the liver, oxygen consumption should be enhanced to produce ATP. Ammonium chloride (0.13 g/kg) was intravenously administered to anesthetized mice at ~30 min after 250 nmol BTPDM1 injection into the tail vein. PLIM images of hepatic lobules measured 10 min after the administration of ammonium chloride exhibited a marked increase in the

phosphorescence lifetime of BTPDM1 (Figs. 4-5A and 4-5B). The average phosphorescence lifetimes (τ_p) and $p\text{O}_2$ of different ROIs in the pericentral region (ROI1) and periportal regions (ROI2 and ROI3) showed that the lifetimes decreased over time, and the O_2 levels recovered to the original levels in approximately 1 h (Fig. 4-5C).

Imaging the spatiotemporal $p\text{O}_2$ changes within the liver microarchitecture provides useful information about the oxygen response and dynamics of the liver at the cellular level during physiological stimulation. The PLIM measurements with BTPDM1 showed that intravenous administration of NH_4Cl resulted in a rapid decrease in hepatic tissue O_2 levels, and its recovery rate depended on the position in the lobule (Fig. 4-5). Hepatocytes are known to display considerable functional differences depending on their position along the porto-central axis of the liver lobule, and ammonia detoxification in the liver occurs by two pathways: consumption by urea synthesis in the periportal area and removal by glutamine synthesis in perivenous area. Since these processes require O_2 consumption, ammonia stimulation may produce hypoxic regions in the hepatic lobules depending on the O_2 consumption rate of hepatocytes.

To clarify the difference in *in vivo* O_2 probe performance between BTPDM1 and BTP-3OH, O_2 imaging experiments were performed on liver tissues using another Ir(III) complex, $(\text{btp})_2\text{Ir}(\text{acac-2OH})$ that has a similar structure to BTPDM1 (Fig. 4-6A). The τ_p^0 and k_q of $(\text{btp})_2\text{Ir}(\text{acac-2OH})$ in AML 12 cells were determined to be 4.80 µs and 4.82×10^3 mmHg^{-1}s^{-1}. The PLIM image (Fig. 4-6B) in the hepatic lobule of an $(\text{btp})_2\text{Ir}(\text{acac-2OH})$-administered mouse exhibited a clear lifetime gradient and gave an average $p\text{O}_2$ of 16 ± 3.2 mmHg in CV, 21 ± 3.4 mmHg in IR, and 24 ± 3.8 mmHg in PV (Fig. 4-6C). The hepatic O_2 levels obtained with $(\text{btp})_2\text{Ir}(\text{acac-2OH})$ were close to

those obtained with BTPDM1, although (btp)$_2$Ir(acac-2OH) gave somewhat smaller pO$_2$ values.

The existence of the oxygen gradient in the hepatic lobule has been suggested by applying the hypoxia marker 2-nitroimidazole to liver tissue sections [4]. High-resolution visualization of hepatic oxygen distribution *in vivo* has been performed by Paxian et al [5]. by intravital emission microscopy using [Ru(phen)$_3$]$^{2+}$ (Tris(1,10-phenanthroline)ruthenium(II)) as an O$_2$ probe. They observed a continuous increase in emission intensity of [Ru(phen)$_3$]$^{2+}$ from periportal to pericentral regions in rat liver, implying an O$_2$ gradient within the liver tissue. However, the emission intensity depends on the probe distribution in the tissue, so that intensity-based measurements cannot assess the precise pO$_2$ and O$_2$ gradient. As for hepatic tissue oxygen levels, Kietzmann and Jungermann [6,7] have reported the pO$_2$ to be 60-65 mmHg in the periportal blood and 30-35 mmHg in the perivenous blood, and they suggested the pO$_2$ level to be approximately 15 mmHg lower in periportal and perivenous cells. Tsukada and Suematsu [8] have investigated the average pO$_2$ in hepatic microcirculation by phosphorescence lifetime measurements of BSA (bovine serum albumin)-bound Pd-TCPP (Pd(II)-meso-tetra(4-carboxyphenyl)porphine) in hepatic tissues of mice. They obtained an average pO$_2$ of 59.8 mmHg in portal vessels and 38.9 mmHg in central venules. The PLIM measurements with BTPDM1 in this study showed that the average pO$_2$ of hepatocytes near PV and CV were 39 ± 4.2 mmHg and 24 ± 6.1 mmHg, respectively. Although the hepatic oxygen levels obtained in this study are somewhat lower than those reported for intravascular pO$_2$, these are considered to be reasonable values given the oxygen levels to which hepatocytes are exposed. To the best of our knowledge, the PLIM images shown in Fig. 4-3 are the first to visualize the oxygen concentration gradient in hepatic lobules *in vivo* using an intracellular O$_2$ probe.

In HT-29 cell spheroids, BTPDM1 and BTP-3OH showed almost the same O_2 levels and distribution in Chapter 3, whereas in hepatic tissues of living mice, BTP-3OH gave much lower oxygen levels: 7 ± 2.7 mmHg for the periportal region and 3 ± 1.8 mmHg for the perivenous region (Table 4-1). This suggests that the administration of BTP-3OH to mice causes hypoxia in hepatic tissues due to some specific metabolic processes in the liver. Since spectral measurements (Fig. 4-4) revealed that the luminescent properties of BTPDM1 and BTP-3OH were maintained in liver tissue, it is likely that BTP-3OH is excreted in the bile through solubilization processes that do not affect the luminescent properties such as glucuronidation at the OH group. The luminescence spectrum of the extract from bile 6 hours after probe administration showed that BTPDM1 was excreted through the bile duct along with bile (Fig. 4-7). Considering that (btp)$_2$Ir(acac-2OH), which has the same acac moiety as BTPDM1, gave similar liver tissue O_2 levels as BTPDM1, the lipophilic Tris-ligand structure of BTP-3OH may be related to its metabolism in the liver.
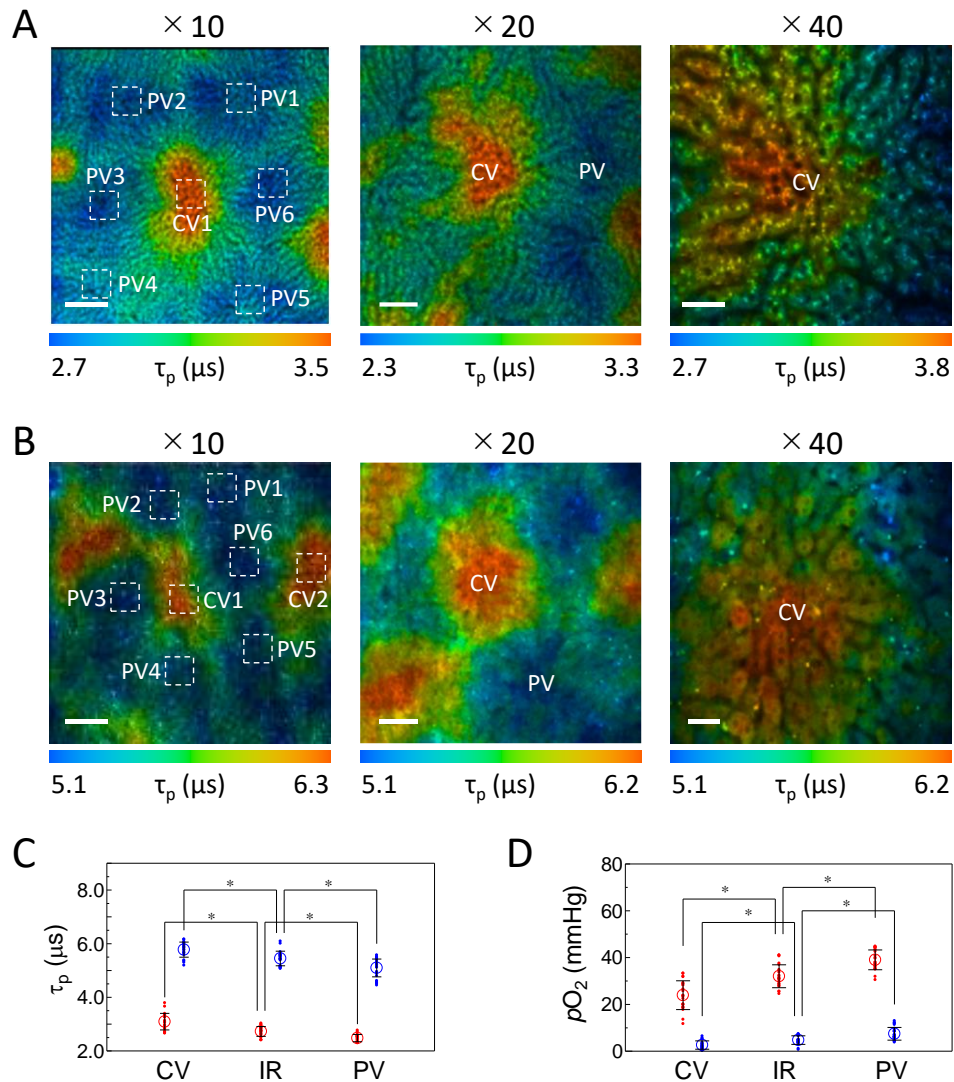
Fig. 4-3 PLIM images of the hepatic surface of a mouse administered with BTPDM1 (**A**) and BTP-3OH (**B**). The color bar indicates phosphorescence lifetime in μs. Left images: 10× objective lens, center images: 20× objective lens, right images: 40× objective lens. λ_{ex}: 488 nm, λ_{em}: >590 nm. Scale bar: 200 μm (left images), 100 μm (center images), and 50 μm (right images). CV: central vein, PV: portal vein. (**C, D**) Phosphorescence lifetime of BTPDM1 (red) and BTP-3OH (blue) and pO_2 in hepatic lobules. Average of phosphorescence lifetime and pO_2 are shown. $N = 23$ ROIs for CV, 23 for IR (intermediate region between CV and PV), and 24 for PV in 5 mice administered BTPDM1. $N = 21$ ROIs for CV, 23 for MR, and 27 for PV in 5 mice administered BTP-3OH. *p value < 0.01 by 2-tailed unpaired t test. Error bar: S.D.

Table 4-1 Phosphorescence lifetimes (τ_p) of BTPDM1 and BTP-3OH at around CV, IR, and PV in hepatic lobules and the pO_2 values calculated from the lifetime. CV: central vein, IR: intermediate region between CV and PV, PV: portal vein.

Area	τ_p (µs)		pO_2 (mmHg)	
	BTPDM1	BTP-3OH	BTPDM1	BTP-3OH
CV	3.09 ± 0.31	5.78 ± 0.28	24 ± 6.1	3 ± 1.8
IR	2.73 ± 0.18	5.45 ± 0.27	32 ± 4.9	5 ± 1.8
PV	2.48 ± 0.14	5.10 ± 0.33	39 ± 4.2	7 ± 2.7

[a] $N = 23$ ROIs for CV, 23 for IR, and 24 for PV in 5 mice administered with BTPDM1. $N = 21$ ROIs for CV, 23 for IR, and 27 for PV in 5 mice administered BTP-3OH.
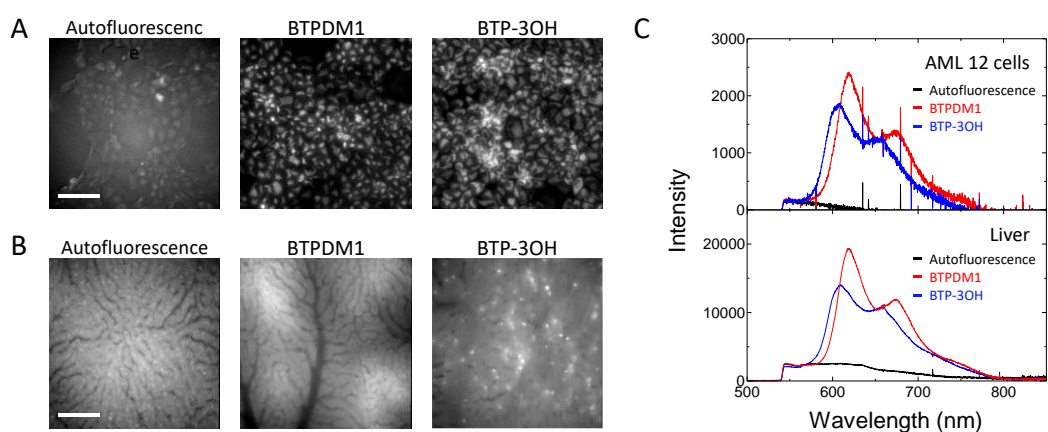
Fig. 4-4 Emission images and spectra of AML 12 cells and liver surface of a living mouse. (**A**) Autofluorescence of AML 12 cells (left), emission images of AML 12 cells incubated with BTPDM1 (middle) and BTP-3OH (right) (1 μM, 2 h). λ_{ex}: 450-500 nm, λ_{em}: >532 nm. Scale bar: 100 μm. (**B**) Emission intensity images of mouse liver with and without probe administration. Autofluorescence in the absence of probe (left), with administration of 250 nmol BTPDM1 (middle) and 250 nmol BTP-3OH (right). λ_{ex}: 450-500 nm, λ_{em}: >532 nm. Scale bar: 100 μm. (**C**) Emission spectra derived from the images in **A** (upper) and **B** (lower), respectively. Black line: autofluorescence in the absence of probe, red line: BTPDM1, blue line: BTP-3OH. λ_{ex}: 450-500 nm.
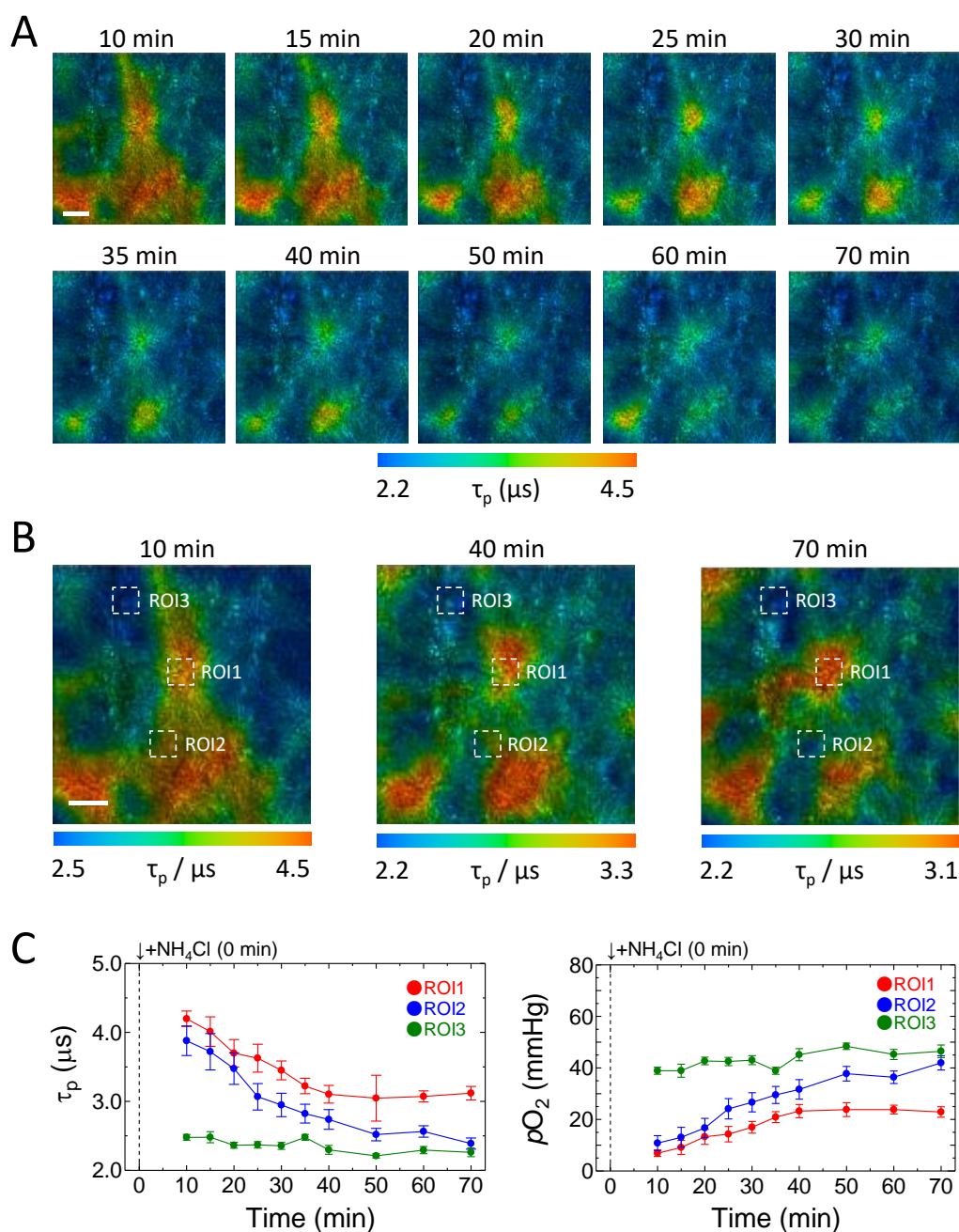
Fig. 4-5 (A, B) Variation of PLIM images of hepatic lobules after administration of NH4Cl following BTPDM1 injection into the tail vein of a mouse. λ_{ex}: 488 nm, λ_{em}: >590 nm. Scale bar: 200 μm. (**C, D**) Variation of average phosphorescence lifetime and pO2 of ROIs in the pericentral region (ROI1) and periportal regions (ROI2 and ROI3) shown in **B**. Error bar: S.D.
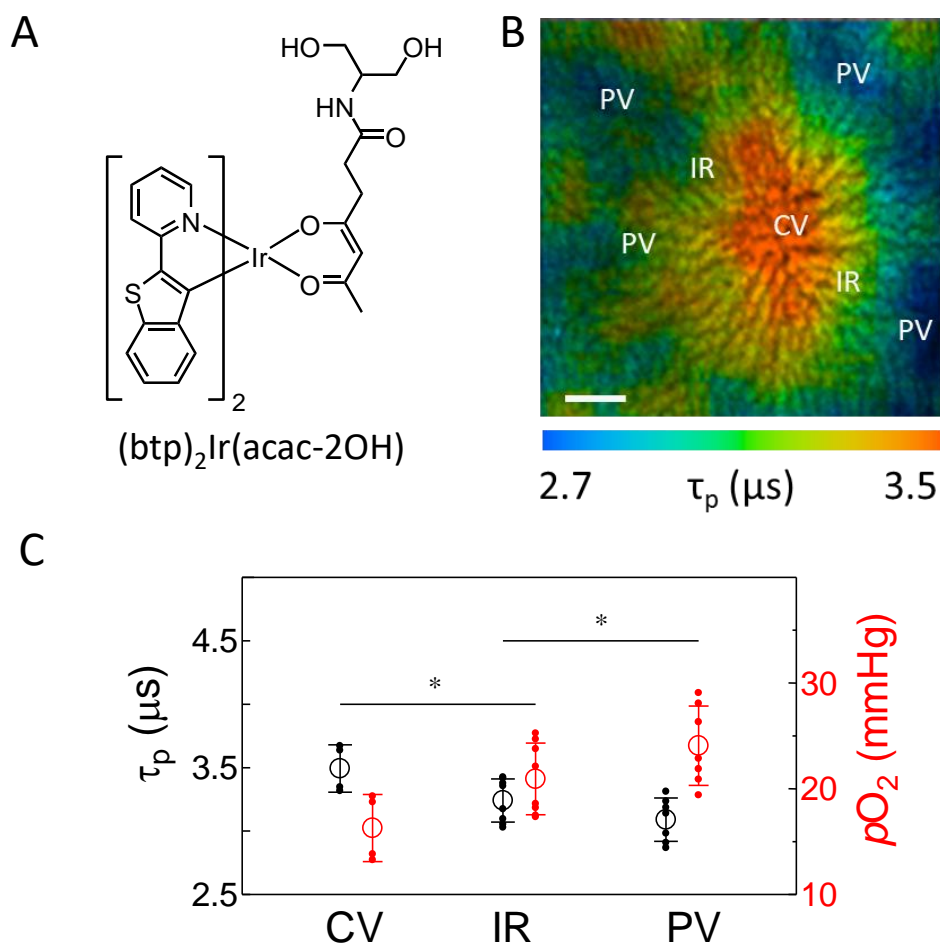
Fig. 4-6 *In vivo* O_2 imaging in hepatic tissues using (btp)$_2$Ir(acac-2OH). (**A**) Chemical structure of (btp)$_2$Ir(acac-2OH). (**B**) PLIM image of hepatic lobules of an (btp)$_2$Ir(acac-2OH) administered mouse. CV: central vein, IR: intermediate region between CV and PV, PV: portal vein. λ_{ex}: 488 nm, λ_{em}: >590 nm. Scale bar: 100 μm. (**C**) Phosphorescence lifetime of (btp)$_2$Ir(acac-2OH) and pO$_2$ in hepatic lobules. $N = 4$ ROI for CV, 8 for IR, and 7 for PV from 2 mice administered (btp)$_2$Ir(acac-2OH). *p value < 0.05 by 2-tailed unpaired t-test. Error bar: S.D.
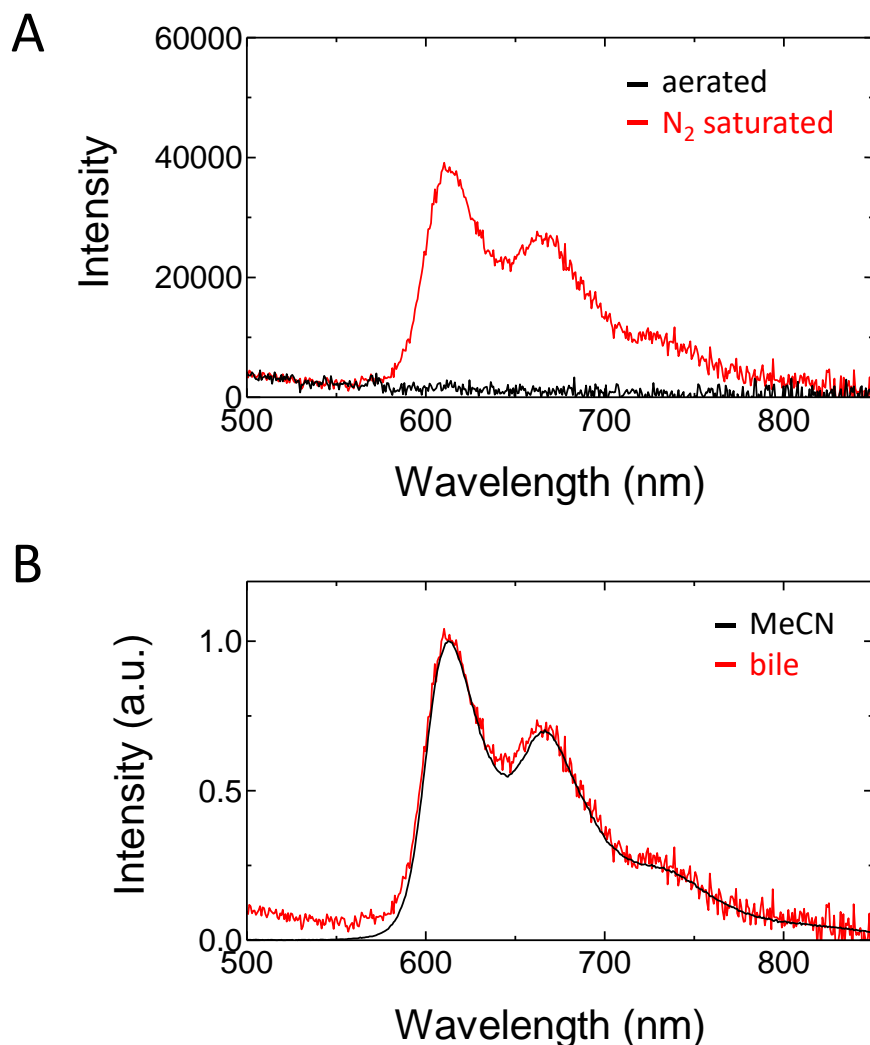
Fig. 4-7 (**A**) Emission spectrum of the extract from bile 6 hours after BTPDM1 administration (red: in N_2 saturated MeCN; black: in aerated MeCN). (**B**) Comparison of the emission spectrum (red) of the extract with the phosphorescence spectrum of BTPDM1 in MeCN (black). Normalized by the intensity of the emission maximum wavelength. Bile was collected 6 hours after the mouse was administered 250 nmol of BTPDM1. The collected bile was separated with water and chloroform to extract an organic layer, and then dried under reduced pressure. The extract was dissolved in MeCN and the emission spectrum was measured.

4-3   Conclusions

PLIM measurements of mouse livers following intravenous administration of BTPDM1 or BTP-3OH allowed high-resolution O_2 imaging of hepatic tissues, exhibiting an O_2 gradient from the pericentral to periportal regions in hepatic lobules. The phosphorescence lifetime of BTPDM1 in the liver gave reasonable hepatic O_2 levels by calibrating the lifetime using cultured AML 12 cells. Furthermore, BTPDM1 allowed visualization of the pO_2 changes in hepatic tissues stimulated by ammonia. However, BTP-3OH gave a much lower pO_2 compared with BTPDM1, which may be due to the toxicity of BTP-3OH, which promoted detoxification in the liver. These results reveal that Ir(III) complexes allow imaging of spatiotemporal changes in oxygen levels within the tissue microarchitecture *in vivo*, but some complexes may influence oxygen consumption in the liver when used for oxygen imaging of hepatic tissues.

Appendix 4-1　Synthesis and Characterization of BTP-3OH

Synthesis of (btp)₂Ir(acac-2OH)
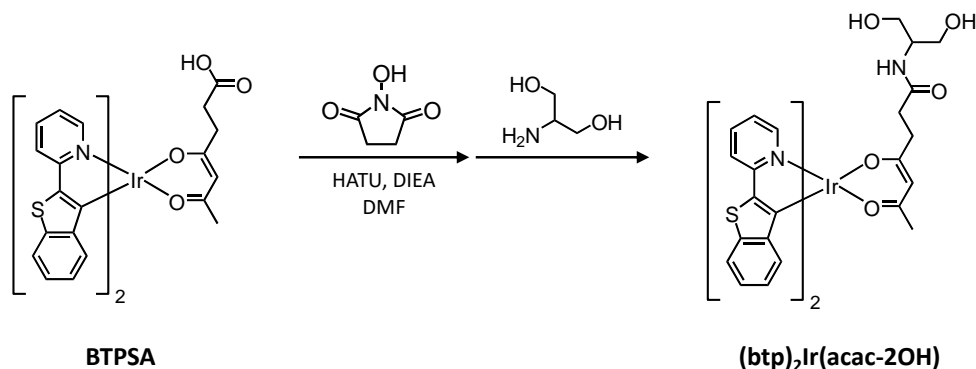
Scheme A4-1 Synthesis of (btp)₂Ir(acac-2OH).

BTPSA (200 mg, 0.26 mmol), *N*-hydroxysuccinimide (70 mg, 0.61 mmol), *o*-(7-azabenzotriazol-1-yl)-*N,N,N',N'*-tetramethyluronium hexafluorophosphate (HATU, 230 mg, 0.61 mmol), *N,N*-diisopropylethylamine (DIEA, 340 mL, 2 mmol) were dissolved in *N,N*-dimethylformamide (DMF, 3 mL). The solution was stirred for 5 h at room temperature under nitrogen, then 2-amino-1,3-propanediol (90 mg, 1 mmol) was added to the solution. The solution was stirred for 24 h at room temperature, and was evaporated to dryness under reduced pressure. The crude product was purified by aminopropyl-modified silica-gel column chromatography using chloroform/methanol (95:5, v/v) as eluent. The final product ((btp)₂Ir(acac-2OH)) was obtained as yellow powder (130 mg, 0.15 mol, 62%). ^{1}H NMR (400 MHz, DMSO-d_6): δ 8.39 (dd, J = 5.7, 23.1 Hz, 2H), 7.99-7.94 (m, 2H), 7.79-7.71 (m, 4H), 7.45 (d, J = 8.0 Hz, 1H), 7.28-7.23 (m, 2H), 7.06 (dd, J = 7.9, 7.2 Hz, 2H), 6.78 (dd, J = 8.0, 7.1 Hz, 2H), 6.05-6.01 (m, 2H), 5.33 (t, J = 5.7 Hz, 1H), 4.59-4.50 (m, 2H), 3.62-3.54 (m, 1H), 3.27-3.20 (m,

4H), 2.29-2.02 (m, 4H), 1.70 (s, 3H). ESI-MS (positive): calcd. for $C_{36}H_{32}IrN_3O_5S_2$

[M]$^+$: 843.14, found: 843.2.

References

[1] Hijmans, B. S., Grefhorst, A., Oosterveer, M. H. & Groen, A. K. Zonation of glucose and fatty acid metabolism in the liver: Mechanism and metabolic consequences. *Biochimie* **96**, 121–129 (2014).

[2] Kietzmann, T. Liver zonation in health and disease: hypoxia and hypoxia-inducible transcription factors as concert masters. *Int. J. Mol. Sci*. **20**, 2347 (2019).

[3] Yoshihara, T., Hosaka, M., Terata, M., Ichikawa, K., Murayama, S., Tanaka, A., Mori, M., Itabashi, H., Takeuchi, T., & Tobita, S. Intracellular and in vivo oxygen sensing using phosphorescent Ir(III) complexes with a modified acetylacetonato ligand. *Anal. Chem*. **87**, 2710–2717 (2015).

[4] Arteel, G. E., Thurman, R. G., Yates, J. M. & Raleigh, J. A. Evidence that hypoxia markers detect oxygen gradients in liver: pimonidazole and retrograde perfusion of rat liver. *Br. J. Cancer* **72**, 889–895 (1995).

[5] Paxian, M., Keller, S. A., Cross, B., Huynh, T. T. & Clemens, M. G. High-resolution visualization of oxygen distribution in the liver in vivo. *Am. J. Physiol. Gastrointest. Liver Physiol.* **286**, G37–G44 (2004).

[6] Kietzman, T. Metabolic zonation of the liver: The oxygen gradient revisited. *Redox Biol*. **11**, 622–630 (2017).

[7] Jungermann, K. & Kietzmann, T. Oxygen: Modulator of metabolic zonation and disease of the liver. *Hepatology* **31**, 255–260 (2000).

[8] Tsukada, K. & Suematsu, M. Visualization and analysis of blood flow and oxygen consumption in hepatic microcirculation: application to an acute hepatitis model. *J. Vis. Exp*. **e3996**, 1–5 (2012).

Chapter 5

In Vivo O$_2$ Imaging

in Renal Tissues

5-1　Introduction

In Chapter 4, high-resolution O_2 imaging of hepatic tissue was attained by PLIM measurements of living mice using Ir(III) complexes, BTPDM1 and BTP-3OH. Quantitative O_2 measurements showed that BTPDM1 is particularly useful for quantifying the partial pressure of oxygen in hepatic tissues. In Chapter 5, the oxygen distribution of renal tissue, in which oxygen deficiency is thought to be associated with disease, was investigated by PLIM measurements using BTPDM1 as O_2 probe.

The kidney is a blood-rich organ that receives ~25% of cardiac output. However, this blood flow is due to the production of urine, and from the viewpoint of O_2 supply of organs, it can receive only little amount of O_2 compared to the blood flow rate. Oxygen supply in the kidney is provided by the peritubular capillaries downstream of the glomerulus (Fig. 5-1). Renal tubulointerstitial hypoxia is regarded as the worsening factor of chronic kidney disease (CKD) progression [1]. The response of the kidneys against hypoxia is mainly via tubules. The tubules are composed of several subsets that differ in terms of their energy sources [2]. Among these, proximal tubules obtain ATP from aerobic energy metabolism, which is implicated to be the reason for the susceptibility of the proximal tubules to hypoxia. Therefore, it has been postulated that an O_2 gradient may exist between the tubule subgroups. However, there seems no reports on high-resolution O_2 imaging in renal tissue *in vivo*, and thus, in this chapter, the O_2 distribution in the renal cortex was investigated by measuring PLIM images of the kidney using BTPDM1 as an intracellular O_2 probe and fluorescein isothiocyanate (FITC)-conjugated *Lycopersicon esculentum* lectin (FITC-lectin) as a vascular imaging reagent.
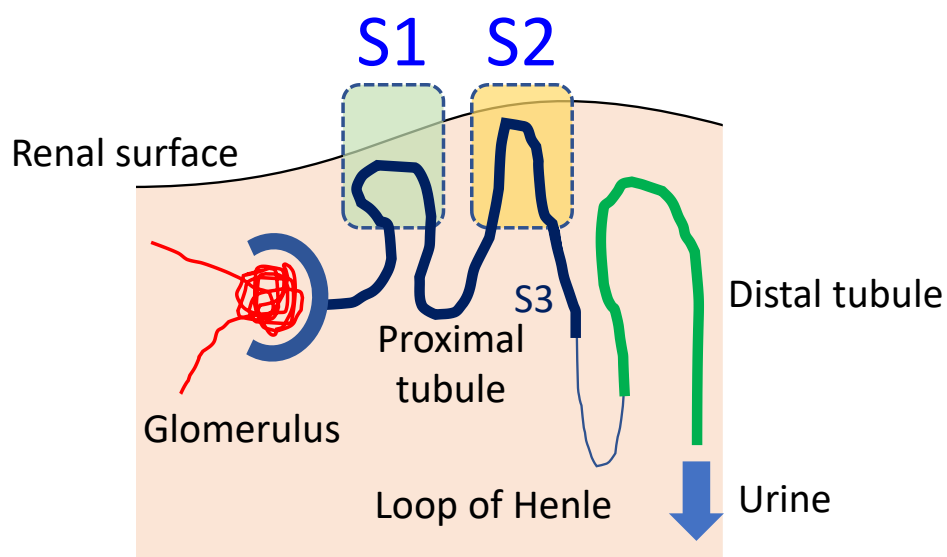
Fig. 5-1 Schematic representation of the structure of renal surface. Proximal tubule is composed of several subgroups such as S1 and S2 segments shown in this scheme.

5-2 Results and Discussion

5-2-1 Photophysical properties of FITC-lectin in H$_2$O

Simultaneous administration of intracellular and intravascular probes to mice is very useful to image the complex structure of renal cortex consisting of tubular cells, capillaries, and urinary spaces. Therefore, in addition to BTPDM1, FITC-lectin, which is known as a vascular endothelial staining probe, was used to visualize capillaries in renal cortex. Fig. 5-2 shows the absorption and fluorescence spectra of FITC-lectin dissolved in H$_2$O. The maximum wavelength of S$_1$←S$_0$ absorption of FITC-lectin appeared at 496 nm, and the fluorescence spectrum extended from 480 nm to 700 nm with maximum at 520 nm (Table 5-1). The fluorescence lifetime and quantum yield were 3.01 ns and 0.29, respectively. Since BTPDM1 emits red phosphorescence and FITC-lectin emits green fluorescence, simultaneous administration of BTPDM1 and FITC-lectin to mice enables multicolor imaging of tubular cells and capillaries in the kidney.
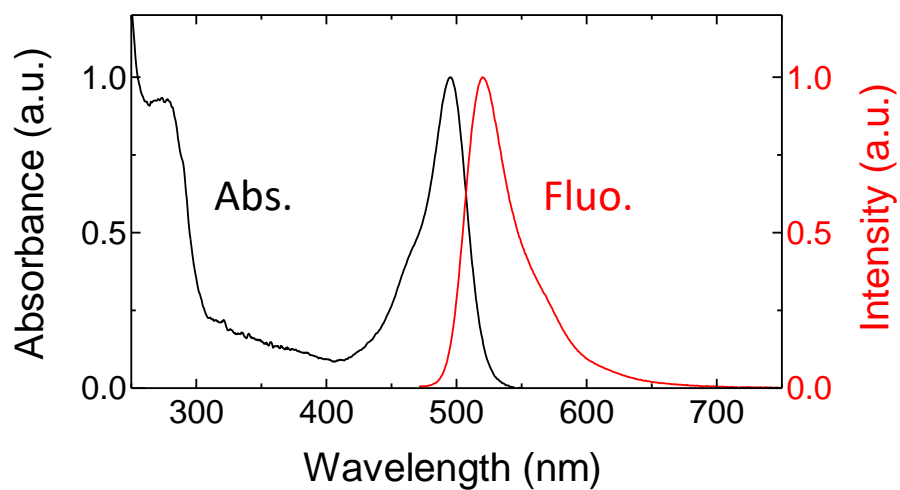
Fig. 5-2 Absorption and fluorescence spectra of FITC-lectin in H_2O at room temperature.

Table 5-1 Photophysical properties of FITC-lectin in H_2O at room temperature.

probe	λ_{abs}^{max} (nm)	λ_{fluo}^{max} (nm)	τ_f (ns)	Φ_f
FITC-lectin	496	520	3.01	0.29

5-2-2 Quantification of O$_2$ Levels in Renal Tissues

As described in Chapter 3, to quantify the oxygen levels in tissues based on lifetime measurements, a calibration curve is required to show the relationship between lifetime and pO$_2$. Since BTPDM1 taken up into cells is likely to accumulate in specific organelle membranes, the pO$_2$ dependence of the phosphorescence lifetime in cells is expected to be different from that in solution. Therefore, the phosphorescence lifetime was calibrated by measuring PLIM images of human kidney 2 (HK-2) cells incubated with BTPDM1 under various O$_2$ conditions at 37°C (Fig. 5-3A). Prior to the PLIM measurements, 10 μM AntA was added to the medium to suppress the oxygen consumption by cellular respiration. The average lifetime of an entire image was plotted against the pO$_2$ according to the Stern-Volmer equation (Eq. 1-1). A linear relationship was obtained (Fig. 5-3B), and the k_q values for the O$_2$ quenching of BTPDM1 in HK-2 cells was derived to be 3.70×10^3 mmHg^{-1}s^{-1} along with the τ_p^0, 4.35 μs. These values were used to quantify oxygen levels in renal tissues from phosphorescence lifetimes (τ_p) of BTPDM1.
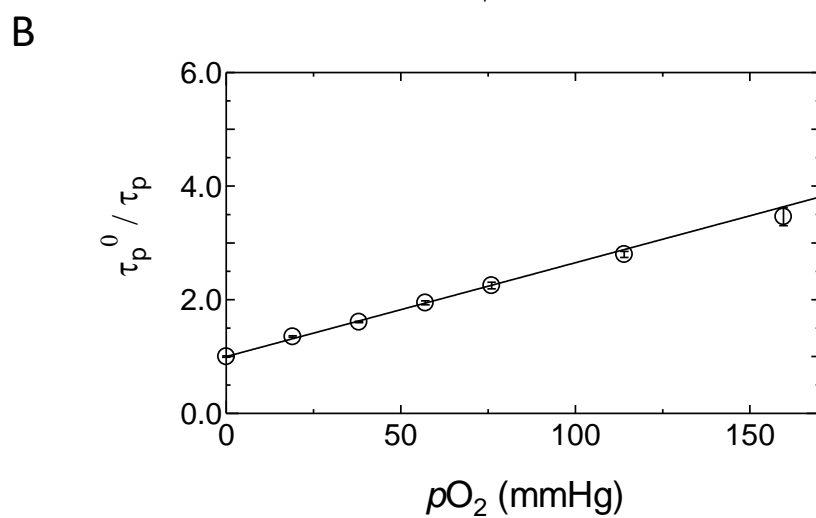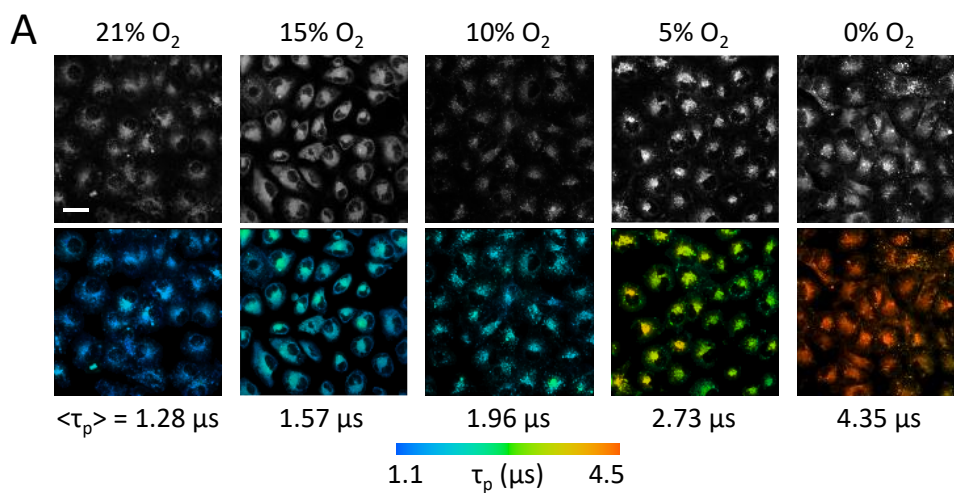
Fig. 5-3 (A) Intensity (upper) and PLIM (lower) images of HK-2 cells stained with BTPDM1 under different pO_2 in an incubator. The average phosphorescence lifetimes are shown below each image. Cells were treated with AntA. λ_{ex}: 488 nm, λ_{em}: >590 nm. Scale bar: 50 μm. **(B)** Stern-Volmer plots of τ_p^0/τ_p as a function of pO_2 for BTPDM1 partitioned into HK-2 cells under different pO_2 in an incubator. Error bars: S.D.

5-2-3 *In Vivo* O$_2$ Imaging in Renal Tissues Using BTPDM1

First, PLIM images of the renal surface were taken at different magnifications using 10×, 20×, 40× and 100× objective lenses to depict the tissue morphology of the kidney surface. BTPDM1 administered from the tail vein traveled through the blood vessel along with the bloodstream, passed through the blood vessel wall, and accumulated in tubular cells (Fig. 5-4). It can be seen from Fig. 5-4 that the phosphorescence intensity images (upper figures) and lifetime images (lower figures) due to BTPDM1 delivered to the kidney clearly visualize the characteristic tissue structure of the renal cortex. The measurements at different magnifications showed that the image taken with 40× objective lens was optimal for observing the tissue structure of the kidney.

Next, PLIM images were measured by changing the focal point of the confocal microscope in the range of 0 to 50 μm from the renal surface. The results are shown in Fig. 5-5. These images were taken at every 10 μm from the renal surface in the depth direction for a mouse administered with BTPDM1 and FITC-lectin. The FLIM images (upper figures) are due to fluorescence of FITC-lectin and autofluorescence from renal tissue as further discussed below, and the PLIM images (lower figures) are due to phosphorescence of BTPDM1. As can be seen from these figures, as the depth from the renal surface increases, the PLIM image becomes blurred due to light scattering and absorption. The clearest images were obtained at 10-20 μm from the surface, so the following measurements were conducted at a depth of ~10 μm.

In order to identify tubular cells and capillaries within a PLIM image, the fluorescent intravascular probe FITC-lectin and phosphorescent intracellular probe BTPDM1 were co-administered to mice (Fig. 5-6). The FLIM image of renal surface of a mouse administered with BTPDM1 alone (Fig. 5-6A, left) shows autofluorescence

of renal tissue, probably due to endogenous fluorescent species such as flavins, and that co-administered with BTPDM1 and FITC-lectin (Fig. 5-6A, right) includes not only fluorescence due to FITC-lectin but also autofluorescence. To distinguish the fluorescence of FITC-lectin from the autofluorescence, the lifetime distributions of the images for FITC-lectin(-) and FITC-lectin(+) were examined as shown in Fig. 5-6B. it can be seen from Fig. 5-6B that the autofluorescence has much shorter lifetime distribution (the average lifetime: ~1 ns) compared with FITC-lectin, and thus, by selectively displaying fluorescence with lifetimes of 2 ns or more, the influence of autofluorescence can be eliminated, and the peritubular capillaries can be selectively imaged (Fig. 5-6C).

Fig. 5-7A shows FLIM and PLIM images of renal tubules of a mouse co-administered with BTPDM1 and FITC-lectin. As can be seen from the color scale of lifetime, the FLIM image in Fig. 5-7A (left) includes autofluorescence as well as FITC-lectin fluorescence so that the structure of renal tissue can be observed closely. Black circles that line around the urinary space are the nuclei of tubular cells. Proximal tubules play an important role in reabsorbing solutes in primary urine, such as sugars, amino acids and electrolytes filtered in the glomerulus, and return them to the blood. Fig. 5-7B schematically shows a cross-sectional structure of one renal tubule derived from the PLIM image. Tubular cells are aligned between the urinary space and the peritubular capillary. By comparing the FLIM image depicting the capillaries with the PLIM image by BTPDM1 phosphorescence in Fig. 5-7A, it can be seen that BTPDM1 distributes intracellularly, mainly in the apical side of tubules, and not in the peritubular capillary or urinary spaces, which is consistent with previous reports [3,4].

It should be noted in the PLIM images in Fig. 5-7 that some tubules have a longer lifetime and some have a shorter lifetime. As shown in the schematic representation of

renal cortex in Fig. 5-1, the proximal tubule mainly consists of subgroups called S1 and S2 segments. Therefore, the S1 and S2 segments can have different lifetimes and thus different pO$_2$. To identify the subgroups of tubules, the urinary excretion dye FITC-conjugated 4 kDa dextran was administered intraperitoneally in living mice. At first, the FITC signals were located only inside the tubules with shorter phosphorescence lifetimes, and later the fluorescence signal of FITC appeared also inside the tubules with longer lifetimes (Fig. 5-8A). Here the upstream and downstream are considered to correspond to S1 and S2 segments, respectively. The PLIM image in Fig. 5-8B and the average lifetimes of upstream and downstream (Fig. 5-8C) demonstrate that the S1 segment has a higher oxygen tension compared with the S2 segment as schematically shown in Fig. 5-9A. Fig. 5-9B shows a PLIM image of the renal cortex measured using a 40× objective lens. Based on the above discussion, the tubules with shorter lifetimes can be attributed to the S1 segment and those with longer lifetimes to the S2 segment.
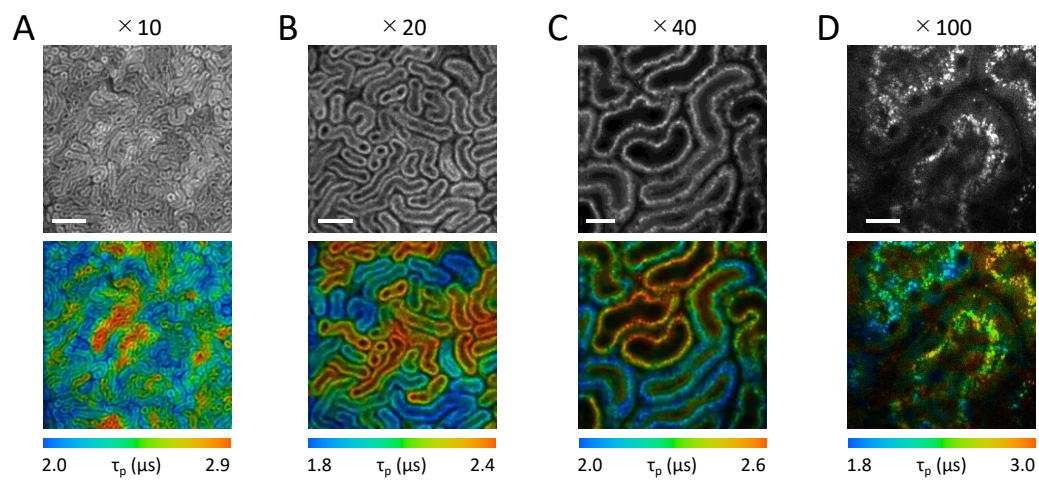
Fig. 5-4 Intensity (upper) and PLIM (lower) images of renal surface of a mouse administered with BTPDM1 obtained with different magnifications: ×10 objective lens (**A**), ×20 objective lens (**B**), ×40 objective lens (**C**) and ×100 objective lens (**D**). λ_{ex}: 488 nm, λ_{em}: >590 nm. Scale bars: 200 μm (**A**), 100 μm (**B**), 50 μm (**C**) and 20 μm (**D**).
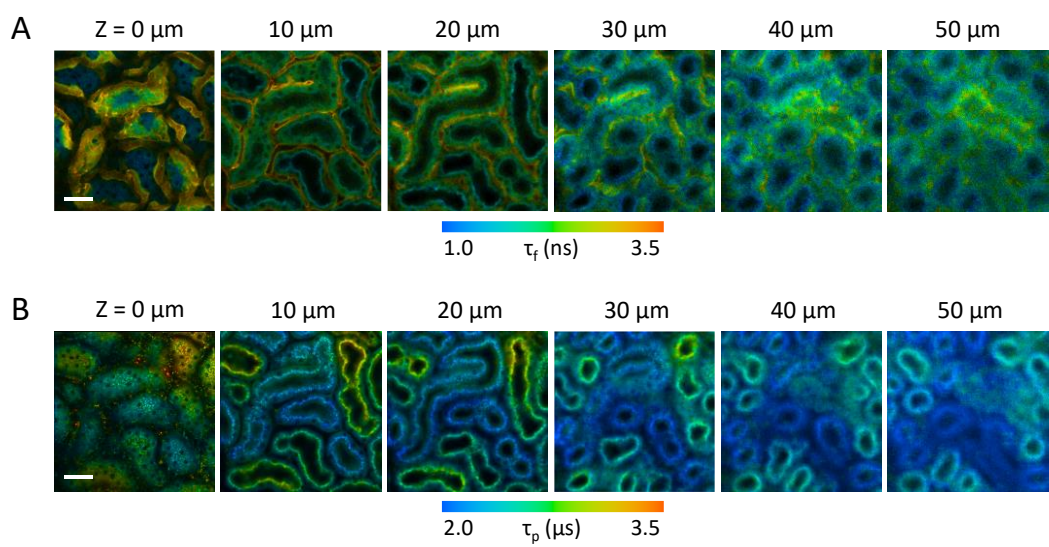
Fig. 5-5 FLIM (**A**) and PLIM (**B**) images taken at every 10 μm from the renal surface in the depth direction for a mouse administered with BTPDM1 and FITC-lectin. λ_{ex}: 488 nm, λ_{em}: 535±50 nm (**A**). λ_{ex}: 488 nm, λ_{em}: >590 nm (**B**). Scale bar: 50 μm.
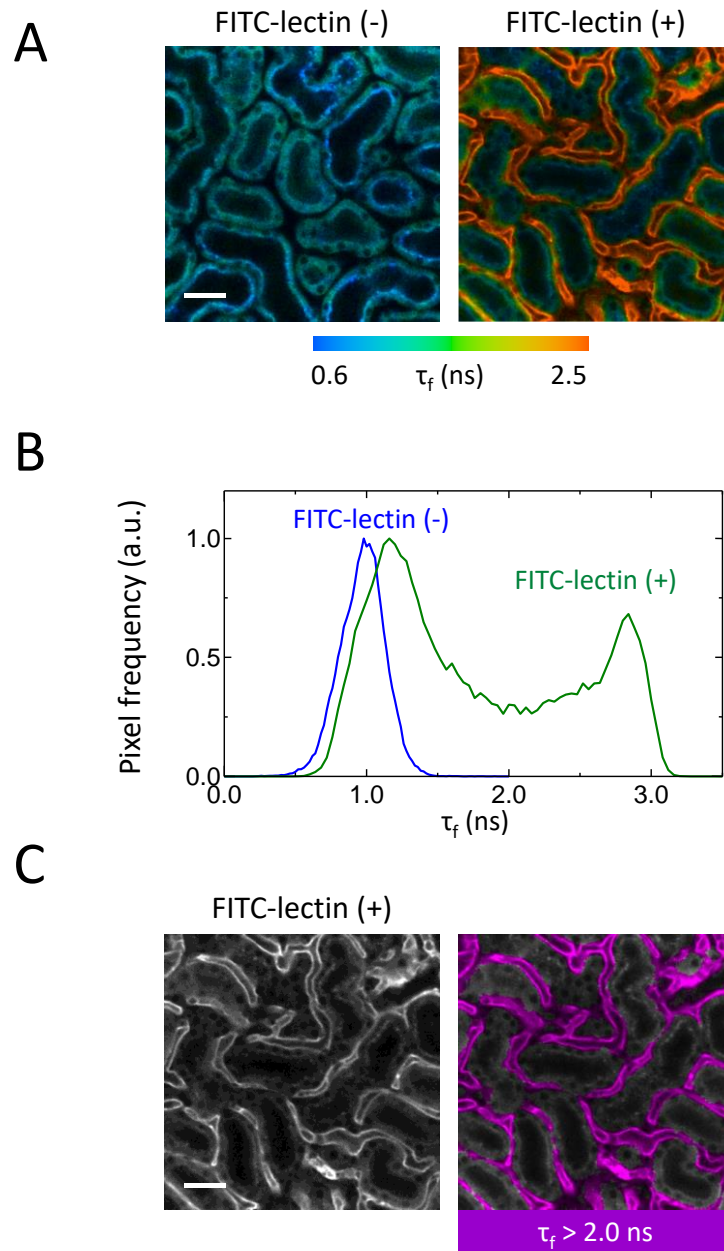
Fig. 5-6 (A) FLIM images of renal surface of a mouse administered with BTPDM1 (left) or BTPDM1 and FITC-lectin (right). λ_{ex}: 488 nm, λ_{em}: 535±50 nm. Scale bar: 50 μm. **(B)** Distribution of fluorescence lifetime for FITC-lectin (-) and FITC-lectin (+) shown in **A**. **(C)** Fluorescence intensity image (left) and lifetime image (right) with the fluorescence lifetime over 2.0 ns for the FITC-lectin (+) image shown in **A**. Scale bar: 50 μm.
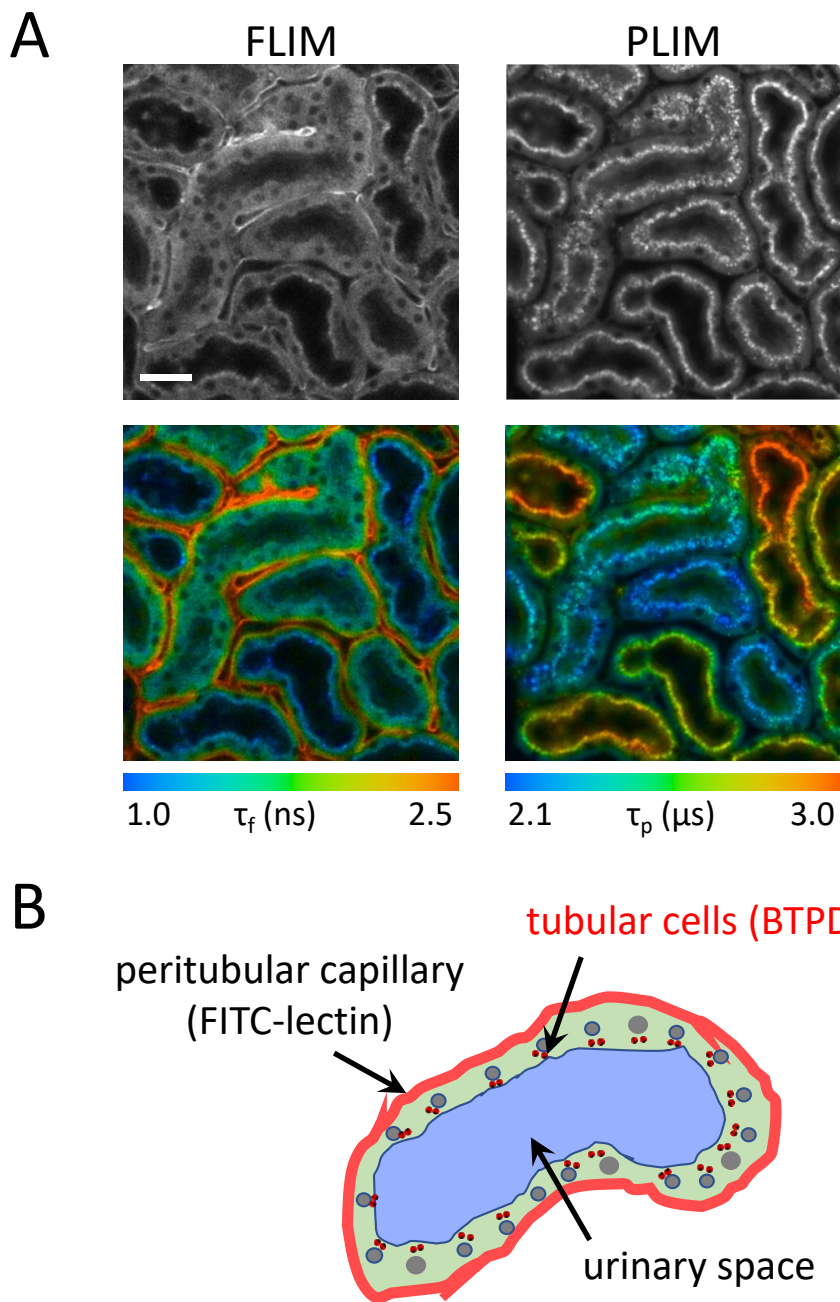
A

FLIM PLIM

1.0 τ_f (ns) 2.5 2.1 τ_p (µs) 3.0

B

tubular cells (BTPDM1)

peritubular capillary
(FITC-lectin)

urinary space

Fig. 5-7 (A) Intensity (upper) images and FLIM/PLIM (lower) images of renal tubule of a mouse administered with BTPDM1 and FITC-lectin. λ_{ex}: 488 nm, λ_{em}: 535±50 nm (FLIM). λ_{ex}: 488 nm, λ_{em}: >590 nm (PLIM). Scale bar: 50 µm. **(B)** Schematic representation of the structure of renal surface stained with BTPDM1 and FITC-lectin.
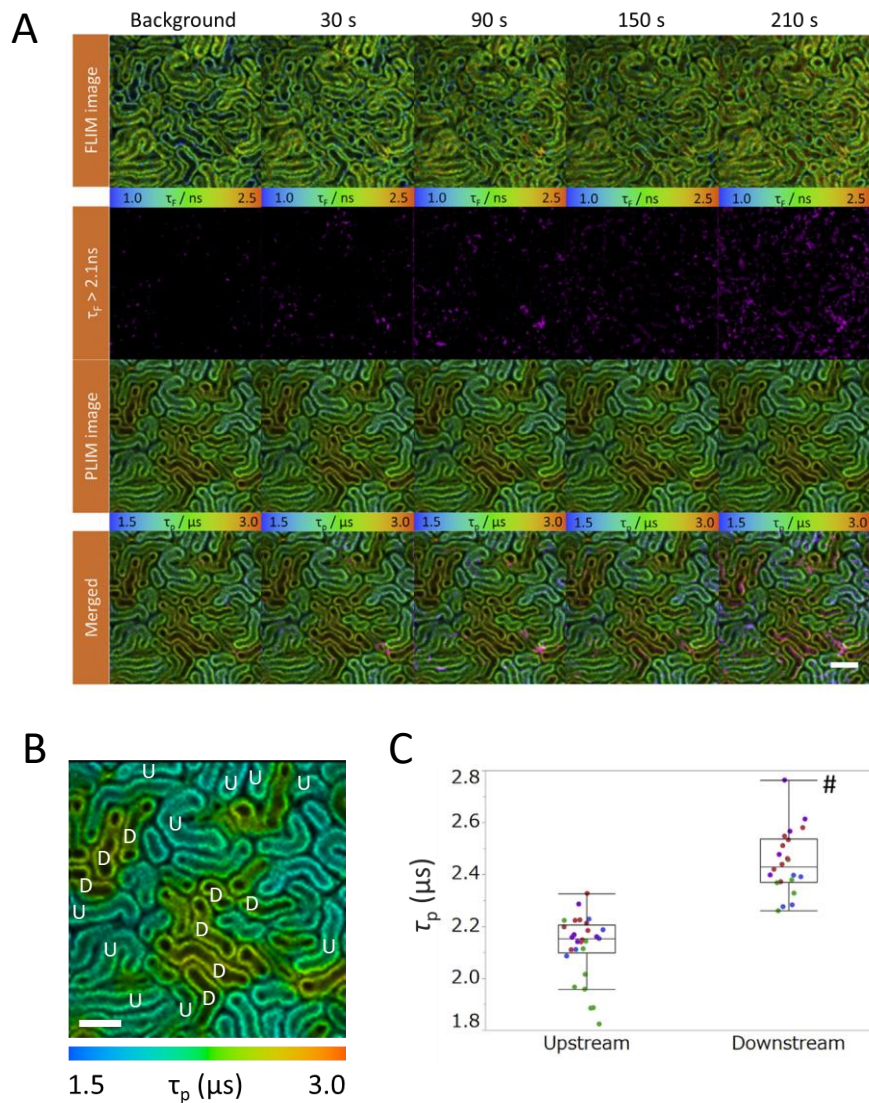
Fig. 5-8 Identification of S1 and S2 segments. (**A**) Dynamics of FITC-dextran merged with a PLIM image. Scale bar: 100 μm. (**B**) Identification of upstream and downstream tubules. Tubules in the PLIM images are divided into 2 subgroups according to the timing that FITC signals appear in the urinary space. U, upstream; D, downstream. Scale bar:100 μm. (**C**) Difference in the phosphorescence lifetime between upstream and downstream tubules. Averages of lifetime are shown. $N = 29$ for upstream tubules and $N = 22$ for downstream tubules in 4 mice. #P value < 0.05 by 2-tailed unpaired t-test.
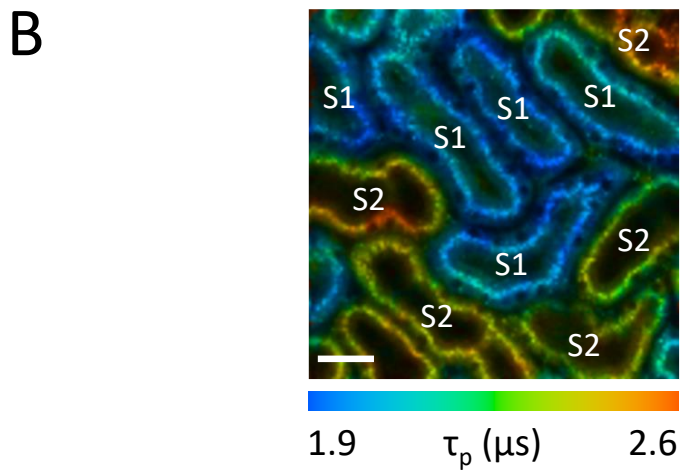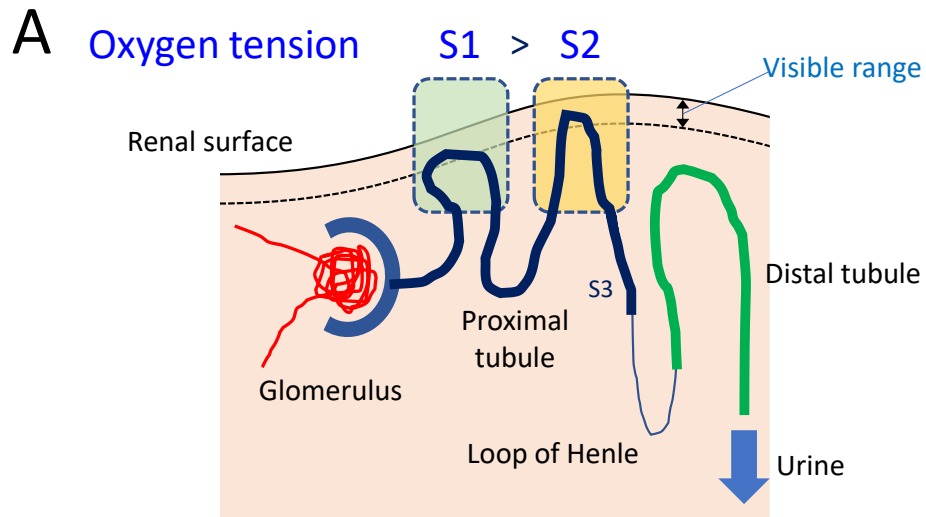
Fig. 5-9 (**A**) Schematic representation of the structure of renal surface and the oxygen gradient in tubules. Proximal tubule is composed of S1 and S2 segments. (**B**) PLIM image of renal tubules of a mouse administered with BTPDM1 showing oxygen gradient in S1 and S2 segments. λ_{ex}: 488 nm, λ_{em}: >590 nm. Scale bar: 50 μm.

5-2-4 Response of Renal Tissue O_2 Levels to Changes in Inspiratory O_2 Concentration

To quantify the O_2 levels in the renal tubules, the phosphorescence lifetimes in PLIM images were converted to pO_2. The experiments were carried out both 21% O_2 inhalation condition (Normoxia) and 15% O_2 inhalation condition (Hypoxia) using O_2/N_2 mixed gas (Fig. 5-10A). The PLIM image taken under hypoxia showed, as a whole, longer lifetimes compared to images under normoxia (Fig. 5-10B). The lifetime restored by reoxygenation, but the lifetime of both upstream and downstream has become shorter than the original lifetimes. Using the τ_p^0 and k_q of BTPDM1 determined in monolayer HK-2 cells (Fig. 5-3), the average pO_2 of renal tubules under normoxia, hypoxia and reoxygenation were obtained as shown in Table 5-2. The pO_2 values under normoxia obtained in this study are in good agreement with the values (45-50 mmHg) measured by using a needle microelectrode [5,6]. The latter method using a needle microelectrode has the advantage of being able to observe the tissues in deep, but it is invasive because the needle is inserted into the kidney tissue, and is limited to one-point measurements.
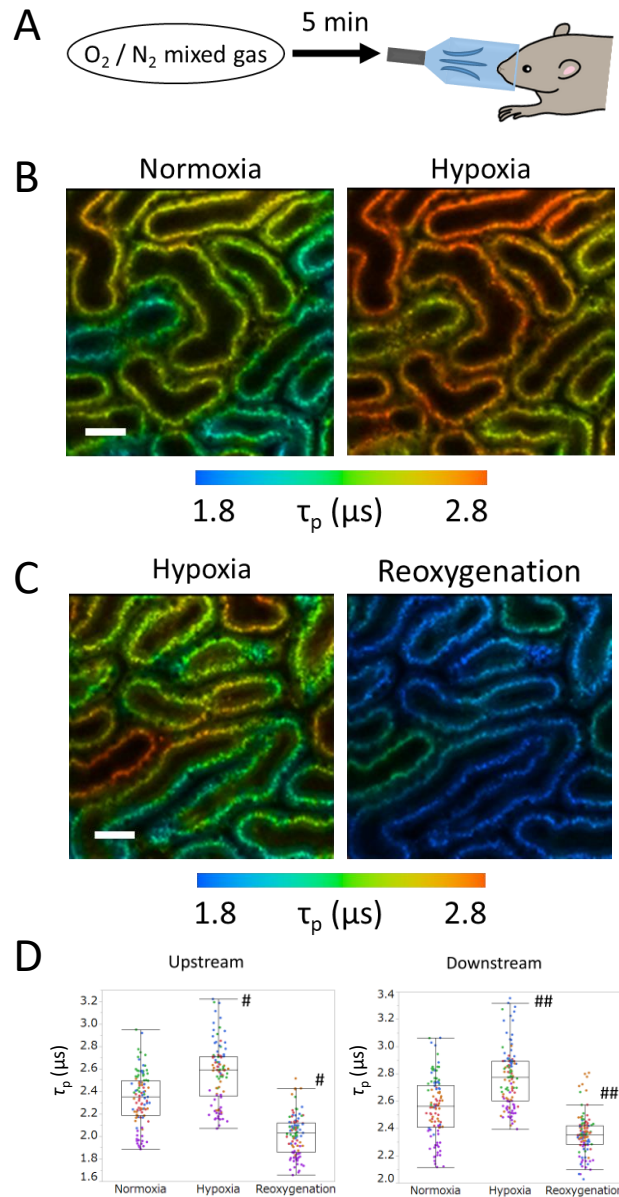
Fig. 5-10 (A) Schematic view of a mouse inhaled O_2/N_2 mixed gas. (**B**, **C**) Variation of PLIM images of renal tubule of a mouse administered with BTPDM1 under normoxia, hypoxia and reoxygenation. λ_{ex}: 488 nm, λ_{em}: >590 nm. Scale bar: 50 μm. (**D**) Phosphorescence lifetime of BTPDM1 in each renal tubule group of mice under normoxia, hypoxia and reoxygenation. N = 105, 103, 104, 106, and 118 for upstream normoxia, upstream hypoxia, upstream reoxygenation, downstream normoxia, downstream hypoxia, and downstream reoxygenation in 5 mice, respectively. #p value < 0.001 by 2-tailed unpaired t test compared with upstream normoxia. ##p value < 0.001 by 2-tailed unpaired t test compared with downstream normoxia. Error bar: S.D.

Table 5-2 Average phosphorescence lifetime (τ_p) of BTPDM1 in renal tubules and the pO_2 values calculated from the lifetime.

Subgroup of tubules	τ_p (μs)		pO_2 (mmHg)	
	Upstream	Downstream	Upstream	Downstream
Normoxia	2.44	2.67	49	41
Hypoxia	2.71	2.87	39	33
Reoxygenation	2.09	2.36	68	54

N = 105, 103, 104, 106, and 118 for upstream normoxia, upstream hypoxia, upstream reoxygenation, downstream normoxia, downstream hypoxia, and downstream reoxygenation in 5 mice, respectively.

5-3　Conclusions

In vivo FLIM/PLIM measurements with BTPDM1 and FITC-lectin as intracellular and intravascular probes enabled visualization of microstructure of the renal tissue with a space resolution of cellular level. Gated measurements utilizing the difference in lifetime between autofluorescence and FITC fluorescence were shown to be useful for selective visualization of the capillary network. The O_2 probe BTPDM1 administered from the tail vein of mice accumulated mainly in lysosomes in tubular cells and gave O_2-dependent phosphorescence. The phosphorescence lifetime of BTPDM1 was converted to the oxygen partial pressure using the HK-2 cell line. It was found from the results that the O_2 levels differed depending on the tubular subgroups; the S1 segment, which is closer to the glomerulus, gave higher O_2 tension compared to the S2 segment. When the O_2 concentration in respiration was reduced from 21% to 15%, the partial pressure of oxygen in the renal tissue also decreased immediately, and recovered when the O_2 concentration was returned to 21%. From these results, it was demonstrated that the PLIM technique using BTPDM1 as an O_2 probe is extremely useful for tracking the oxygen status of renal tissue *in vivo* with high spatial resolution. As far as we know, this study is the first report of confocal PLIM imaging of the renal cortex in living mice.

References

[1]   Mimura, I. & Nangaku, M. The suffocating kidney: tubulointerstitial hypoxia in end-stage renal disease. *Nat. Rev. Nephrol*. **6**, 667–678 (2010).

[2]   Epstein, F. H. Oxygen and renal metabolism, *Kidney Int*. **51**, 381-385 (1997).

[3]   Hirakawa, Y., Yoshihara, T., Kamiya, M., Mimura, I., Fujikura, D., Masuda, T., Kikuchi, R., Takahashi, I., Urano, Y., Tobita, S., & Nangaku, M. Quantitating intracellular oxygen tension in vivo by phosphorescence lifetime measurement. *Sci. Rep*. **5**, 17838 (2015).

[4]   Declèves, A. E., Zolkipli, Z., Satriano, J., Wang, L., Nakayama, T., Rogac, M., Le, T. P., Nortier, J. L., Farquhar, M. G., Naviaux, R. K., & Sharma, K. Regulation of lipid accumulation by AMP-activated kinase in high fat diet-induced kidney injury. *Kidney Int*. **85**, 611-623 (2014).

[5]   Nordquist, L., Friederich-Persson, M., Fasching, A., Liss, P., Shoji, K., Nangaku, M., Hansell, P., & Palm, F. Activation of hypoxia-inducible factors prevents diabetic nephropathy. *J. Am. Soc. Nephrol.* **26**, 328-338 (2015).

[6]   Ow, C. P. C., Abdelkader, A., Hilliard, L. M., Phillips, J. K. & Evans, R. G. Determinants of renal tissue hypoxia in a rat model of polycystic kidney disease. *Am. J. Physiol. Regul. Integr. Comp. Physiol.* **307**, R1207-R1215 (2014).

Chapter 6

Summary

In this thesis, a fluorescence and phosphorescence lifetime imaging microscopy (FLIM/PLIM) system was constructed for high-resolution O_2 imaging of oxygen in living tissues using an optical oxygen probe. By using phosphorescent Ir(III) complexes as O_2 probes, the following findings were obtained regarding the O_2 distribution and dynamics of cell spheroids, hepatic tissues, and renal tissues *in vivo*.

In Chapter 3, a FLIM/PLIM devise was constructed using an inverted microscope equipped with a confocal laser scanning system and an emission lifetime measurement system, and its basic performance was evaluated using a solution of hydrophilic Ir(III) complex, BTP-PEG$_{48}$. After confirming that a uniform PLIM image can be obtained by effective use of spatial binning, O_2 imaging experiments on HT-29 cell spheroids were performed using Ir(III) complexes, BTPDM1 and BTP-3OH. These complexes showed excellent characteristics as intracellular O_2 probe in photophysical properties such as brightness, lifetime, and O_2 sensitivity, and also in intracellular properties such as cellular uptake efficiency, cytotoxicity, and photostability in cells. In particular, their high cell-permeability facilitated penetration into a cell spheroid, enabling O_2 imaging of the entire structure of the cell spheroid. PLIM images of HT-29 cell spheroids with a diameter of ~200 μm showed a lifetime gradient that increases from the peripheral region towards the core. Based on the calibration of phosphorescence lifetime using HT-29 cells, it was shown that the core region of spheroids fell into hypoxia due to cellular respiration consuming oxygen. Furthermore, PLIM measurement allowed tracking changes in cellular oxygen consumption by metabolic stimulation with FCCP and AntA.

In Chapter 4, the PLIM method using BTPDM1 and BTP-3OH was applied to O_2 imaging of the liver in living mice. The probe molecule was intravenously administered to anesthetized mice, and the PLIM image of the hepatic surface was

measured *in vivo*. Both BTPDM1 and BTP-3OH were internalized in hepatocytes, and provided PLIM images visualizing clearly the characteristic structure of hepatic lobules. The lifetimes in the PLIM images were converted to the partial pressure of oxygen (pO_2) based on the τ_p^0 and k_q values which were determined by using AML 12 cells. BTPDM1 gave reasonable O_2 levels: (24 mmHg for central vein and 39 mmHg for portal vein), whereas BTP-3OH exhibited extremely low O_2 levels (3 mmHg for central vein and 7 mmHg for portal vein), suggesting that the detoxification of probes might affect liver O_2 levels. In fact, intravenous administration of NH_4Cl to mice caused the hepatic tissues to fall into hypoxia because of the O_2 consumption to produce ATP required for detoxification of ammonia. These results reveal that Ir(III) complexes allow imaging of spatiotemporal changes in O_2 levels within the tissue microarchitecture *in vivo*, but some complexes may influence oxygen consumption in the liver when used for oxygen imaging of hepatic tissues.

In Chapter 5, the oxygen status of the renal cortex in mice was examined by FLIM/PLIM measurements using BTPDM1 as an O_2 probe. In order to clearly image the structure of renal tissues, red-emitting intracellular probe (BTPDM1) and a green-emitting intravascular probe (FITC-lectin) were simultaneously administered to anesthetized mice. FLIM images due to FITC-lectin and autofluorescence visualized the proximal tubular cells and the peritubular capillaries. PLIM images showed that BTPDM1 was localized in the lysosomes located on the apical side of tubular cells, and gave different lifetimes depending on the tubules. The analysis using the urinary excretion dye FITC-dextran revealed that the S1 segments have shorter lifetimes than S2 segments. Furthermore, PLIM measurements using BTPDM1 showed that O_2 levels in renal tissue were sensitive to inspiratory conditions. Using the τ_p^0 and k_q of BTPDM1 as determined in monolayer HK-2 cells, the average pO_2 in the S1 and S2

segments were obtained to be 49 mmHg and 41 mmHg for 21% O_2 inhalation condition (Normoxia), and 39 mmHg and 33 mmHg for 15% O_2 inhalation condition (Hypoxia). The oxygen partial pressure of the kidney tissue in normoxia obtained from the PLIM measurement showed good agreement with the literature value obtained using the oxygen microelectrode, demonstrating the reliability of the PLIM method.

Finally, it can be concluded from this study that PLIM measurements using Ir(III) complex as an O_2 probe provide a powerful technique for imaging the oxygen status of organ tissues *in vivo* with cellular level resolution.

Acknowledgements

I would like to express my sincere gratitude to **Professor Seiji Tobita** of Gunma University for his insightful direction, valuable suggestions and discussions throughout this study. I wish to thank **Associate Professor Toshitada Yoshihara** for his experimental guidance, valuable advice and discussions. I am deeply grateful to Professor Tobita and Associate Professor Yoshihara, again, for their continuous supports and trust in me.

I am also sincerely grateful to **Professor Tetsuo Okutsu**, **Professor Naoki Asakawa**, **Professor Yosuke Nakamura**, and **Associate Professor Yusuke Inoue** of Gunma University for their valuable comments and kind advises on this thesis.

I am grateful to **Professor Masaomi Nangaku**, **Assistant Professor Yosuke Hirakawa**, and **Doctor Tomoko Honda** of the University of Tokyo for their valuable suggestions and experimental guidance especially for O_2 imaging of renal tissues.

I am also grateful to **Proffesor Nobuhito Goda** of Waseda University for his valuable discussions on O_2 imaging of hepatic tissues.

I would like to warmly acknowledge to **Doctor Shuichi Shiozaki** and all laboratory members for their valuable suggestions and assistance to complete this work.

Finally, I would like to express my deep gratitude to my family for their supports me in every respect.

March 2021

Kiichi Mizukami